Search for a Heavy Resonance Decaying to a Pair of Higgs Bosons in the Four b-quark Final State with the CMS Experiment

by

M. D. Krohn

B.S., University of Wisconsin, 2012

M.S., University of Colorado, 2015

A thesis submitted to the
Faculty of the Graduate School of the
University of Colorado in partial fulfillment
of the requirements for the degree of
Doctor of Philosophy
Department of Physics
2018

This thesis entitled:
Search for a Heavy Resonance Decaying to a Pair of Higgs Bosons in the Four b-quark Final State with the CMS Experiment
written by M. D. Krohn
has been approved for the Department of Physics

Prof. Stephen Wagner

Prof. John P. Cumalat

Date

The final copy of this thesis has been examined by the signatories, and we find that both the content and the form meet acceptable presentation standards of scholarly work in the above mentioned discipline.

Krohn, M. D. (Ph.D., Physics)

Search for a Heavy Resonance Decaying to a Pair of Higgs Bosons in the Four b-quark Final State with the CMS Experiment

Thesis directed by Prof. Stephen Wagner

A search for a massive resonance decaying into a pair of standard model Higgs bosons, in a final state consisting of two b quark-antiquark pairs, is performed using proton-proton collisions at a center-of-mass energy of 13 TeV collected by the Compact Muon Solenoid detector at the Large Hadron Collider and corresponding to an integrated luminosity of 35.9 fb^{-1}. The Higgs bosons are highly Lorentz-boosted and are each reconstructed as a single large-area jet. The signal is characterized by a peak in the dijet invariant mass distribution, above a background from the standard model multijet production. The observations are consistent with the background expectations, and are interpreted as upper limits on the products of the production cross sections and branching fractions of narrow bulk gravitons and radions in warped extra-dimensional models. The limits range from 126 to 1.4 fb at 95% confidence level for resonances with masses between 750 and 3000 GeV, and are the most stringent to date, over the explored mass range.

Acknowledgements

First and foremost, I need to thank my parents, David Krohn and Kay Reuter-Krohn. Without your constant love and support this would not have been remotely possible. You showed me the value of a good work ethic and have been outstanding role models. I cant thank you enough. I also owe a great deal to all the friends in Madison, Boulder, and Fermilab who have always been a major source of support if research ever got discouraging. A special thanks to the PLG.

There are so many people to thank for the help and guidance throughout my graduate research: David Christian and the Fermilab ASIC group for all that you taught me regarding pixel electronics. Ben Bentele and John Cumalat for the long hours collecting data at Sandia. The entire HH to 4b analysis group, Marc Osherson, Devdatta Majumder, Petar Maksimovic, Maxime Gouzevitch, Ching-Wei Chen, Shin-Shan Eiko Yu, and Alice Cocoros, for making this thesis possible. A very special thanks to Caterina Vernieri for bringing me into the HH analysis group, teaching me the fundamentals of a physics analysis, and presenting me with numerous opportunities to further my research. I also must thank the entire CMS community for allowing such a large-scale experiment to somehow function properly.

Finally, Steve Wagner, I am extremely grateful to have had you as an advisor. You gave me the freedom to pursue any topic that interested me and you always searched for the situations that would best allow me to conduct that research. Despite usually being a time zone apart, you were always just a phone call away to offer your insight and advice. Thank you so much for your support and mentorship.

Contents

Chapter

1 Introduction **1**

2 The Standard Model of Particle Physics and Beyond **3**

2.1 The Standard Model 3

2.1.1 Electroweak Theory 6

2.1.2 Quantum Chromodynamics 8

2.2 The Brout-Englert-Higgs Mechanism 10

2.3 The Higgs Boson 13

2.4 Higgs Boson Pair Production 14

2.4.1 Standard Model Production 16

2.4.2 Beyond the Standard Model Production 17

3 Experimental Setup **21**

3.1 The Large Hardon Collider 21

3.2 The Compact Muon Solenoid Detector 22

3.2.1 The Tracker 24

3.2.2 The Electromagnetic Calorimeter 27

3.2.3 The Hadron Calorimeter 29

3.2.4 The Superconducting Magnet 30

3.2.5 The Muon System 30

3.2.6 The Trigger System 32

4 Object Reconstruction **35**

4.1 The Particle Flow Algorithm 35

4.1.1 Iterative Tracking 35

4.1.2 Calorimeter Clustering 36

4.1.3 The Link Algorithm 37

4.1.4 Particle Identification 37

4.2 Vertex Reconstruction 38

4.3 Jet Reconstruction 38

4.4 Missing Transverse Energy 39

4.5 *b*-tagging 39

4.6 Double *b*-tagging 40

5 Radiation Tolerance of 65 nm CMOS Transistors **43**

5.1 Radiation Damage Mechanisms 44

5.2 Experimental Details 46

5.2.1 Transistor Test Setup 46

5.2.2 Irradiation Setup 47

5.3 Analysis 50

5.4 Results 50

5.5 Summary 52

6 Search for a heavy resonance decaying to a pair of Higgs bosons in the four b quark final state in proton-proton collisions at $\sqrt{s} = 13$ TeV **56**

6.1 Motivation and Strategy 57

6.2 Data and Simulated Samples 58

6.3 Triggers 60

6.4 Event Selection . . . 63

6.4.1 Lepton Selection . . . 64

6.4.2 Jet Selection . . . 65

6.4.3 Full Selection . . . 76

6.5 Background Estimation . . . 76

6.5.1 Alphabet Method . . . 80

6.5.2 Alphabet Assisted Bump Hunt Method . . . 90

6.6 Signal Modelling . . . 94

6.7 Systematic Uncertainties . . . 94

6.8 Results . . . 97

7 Summary and Outlook **102**

Bibliography **105**

Tables

Table

2.1 Predicted branching fractions for the Higgs boson with a mass of 125 GeV. The relative uncertainties are calculated from theoretical predictions that depend on the uncertainties of α_s, the quark masses, and the Higgs boson partial decay widths. . . 15

2.2 Cross sections (in fb) for the seven largest Higgs pair production channels at the LHC, with $\sqrt{s} = 13$ and 14 TeV. The first uncertainty is the scale uncertainty, the second is the PDF uncertainty, and the third for gluon fusion is the α_s uncertainty. The gluon fusion, ZHH, and $W^{\pm}HH$ channels have been calculated at next-to-next-to-leading-order (NNLO) QCD and the vector boson fusion, $ttHH$, and $tjHH$ channels have been calculated at next-to-leading-order (NLO) QCD [1]. 16

5.1 The irradiation schedule, showing the 2 weeks it took to accumulate 1 Grad. 50

6.1 List of the primary datasets, their data reconstruction campaign, and their corresponding integrated luminosity. The different datasets correspond to different detector and trigger configurations used by CMS. 59

6.2 List of Monte Carlo signal samples used and the number of events generated for each sample. 60

6.3 List of background Monte Carlo samples used. The two $t\bar{t}$ POWHEG samples correspond to two different productions with the same generator parameters, but the latter with much higher statistics. The cross sections, σ, and number of events generated are also given. 61

6.4 The trigger paths used and their corresponding L1 seeds. 62

6.5 Loose and medium electron identification criteria used in the analysis. The selection criteria vary depending on if the electron is in the barrel or endcap of the detector. $\sigma_{i\eta i\eta}$ is the energy weighted standard deviation of a single crystal within the 5×5 cluster of crystals centered at the crystal with maximum energy and $\Delta\eta_{seed}$ refers to the η difference between the seed and the track. $\Delta\phi_{in}$ is the difference ϕ difference between the supercluster and positions of the inner track extrapolated from the interaction vertex and H/E refers to the energy measured in the hadronic calorimeter divided by the energy measured in the electromagnetic calorimeter. 65

6.6 Loose and medium muon identification criteria used in the analysis. The segment compatibiliy refers to the compatibility of the global muon track to the track formed using just the segments in the muon detector. 65

6.7 Tight jet identification quality criteria used in the analysis. 67

6.8 Full selection criteria for the analysis. 77

6.9 Efficiencies of various spin-2 bulk graviton masses after each selection selection requirement. 78

6.10 Efficiencies of various spin-0 radion masses after each selection selection requirement. 78

6.11 Definition of the signal, the anti-tag, and the sideband regions used for the background estimation. 83

6.12 Summary of systematic uncertainties in the signal and background yields. 97

6.13 Comparison of expected and observed limits on the production cross section of a resonance decaying to HH for the bulk graviton and the radion signal hypotheses, for different values of the resonance mass. The limits for masses below 1200 GeV are obtained using the Alphabet background estimation method, while those above use the AABH method. 101

Figures

Figure

2.1 The quarks, leptons, and bosons that compose the Standard Model[2]. 4

2.2 (Left) The invariant diphoton mass distribution with each event weighted by the $\frac{S}{S+B}$ value of its category. The lines represent the fitted background and signal, and the colored bands represent the ±1 and ±2 standard deviation uncertainties in the background estimate. (Right) Distribtuon of the four-lepton invariant mass for the $ZZ \to 4l$ analysis. The points represent the data, the filled histograms represent the background, and the open histogram show the signal expectation for a Higgs boson of mass $m_H = 125$ GeV [3]. 14

2.3 Best fit values as a function of particle mass for the combination of ATLAS and CMS data, with parameters defined as $\kappa_F \cdot m_F/v$ for the fermions and as $\sqrt{\kappa_V} \cdot m_V/v$ for the weak vector bosons, where $v = 246$ GeV is the vacuum expectation value of the Higgs field. Here $\kappa_F = \lambda_f$ from Equation 2.22 and κ_V corresponds to the coupling of the vector bosons to the Higgs, which depends on g and g' from Equations 2.16. [4]. 15

2.4 The two leading HH production diagrams for gluon fusion [5]. 17

3.1 A schematic of the accelerator chain. 23

3.2 A sliced view of the CMS detector. 24

3.3 A schematic of the CMS tracker in the r-z plane. 25

3.4 Distribution of hit residuals on the second pixel barrel layer in the transverse (left) and longitudinal (right) directions to the beam. The distribution is fitted with a student's t-function for which sigma is shown on the plot. 26
3.5 A comparison of the 2016 pixel detector geometry with the 2017 upgrade geometry. . 26
3.6 Schematic view of a quadrant of the electromagnetic calorimeter (ECAL). The numbers correspond to η and show the coverage of the different sections of the ECAL. . 28
3.7 Schematic cross section of the hadron calorimeter (HCAL). 29
3.8 Schematic view of the muon system. 31
3.9 Schematic of the Level-1 trigger system. 33

4.1 Discriminator values for the combined secondary vertex (CSVv2) algorithm in a dilepton $t\bar{t}$ topology. The total number of entries in the simulation is normalized to the observed number of entries in data. The small bump between discriminator values of 0.5 and 0.6 are due to tracks or jets from pileup collisions [6]. 40
4.2 Schematic comparison of the fatjet and subjet b tagging approaches and the double-b tagger [7]. 41
4.3 Comparison of the performance of the double-b tagger, the CSVv2 subjet b tagging, and fatjet b tagging using the CSVv2 algorithm for $500 < p_T < 800$ GeV jets. The tagging efficiency for signal is evaluated using boosted $\mathrm{H} \to \mathrm{b\bar{b}}$ jets from simulation. The mistag rate is evaluated for simulated QCD jets containing zero, one or two b quarks[7]. 42

5.1 The cross section view of an n-channel transistor. The transistor is built on a p-type substrate with n-type implants as the source and drain. An inversion layer is formed in the conducting channel when a positive voltage is applied to the gate. The gate dielectric (gate oxide) and shallow trench isolation (STI) oxide are the green regions[8]. 44

5.2 The crosses represent positive charge build up in the shallow trench isolation (STI) oxide, which allow current to pass between the source and the drain when no voltage is applied to the gate[9]. 46

5.3 Pictures of the thermos bottle, including an irradiation printed circuit board with four chip carriers, before insertion of the irradiation board into the thermos bottle. On the left, the red arrow points to the vortex tube on top of the thermos bottle lid. On the right, the red arrow points to an antistatic bag which wraps the irradiation board and low-voltage cable before irradiation. These bags keep the boards and voltage cables dry during the irradiation. 48

5.4 The temperature measured inside the two thermos bottles during the long irradiations. No irradiation was performed on June 8 or 9. The two spikes where the temperature reached about 8°C in both thermos bottles for 30 minutes on June 12 occurred because the compressed air unexpectedly turned off. 49

5.5 This figure illustrates the quadratic extrapolation method used to determine the threshold voltage (V_{th}) of an NMOS transistor. The blue data points are the transistor characteristic and the red ones are computed using finite differences $\frac{\sqrt{I_{ds}(N+1)}-\sqrt{I_{ds}(N)}}{V_{gs}(N+1)-V_{gs}(N)}$. The black curve is the result of differentiating the fifth order polynomial that was fit to the characteristic. V_{th} is the point on the $I_{ds} = 0$ axis where the tangent to the characteristic intersects. For PMOS transistors, $|I_{ds}|$ is used since I_{ds} is negative. 51

5.6 Transistor characteristic curves for total dose up to 1.1 Grad of (upper left) a 120/60 core PMOS, (upper right) a 360/60 core PMOS, and for total dose up to 878 Mrad of (lower left) a 240/60 core NMOS, and (lower right) a 1000/280 2.5 V NMOS. . . . 52

5.7 The change in maximum drain-source current for similar PMOS core transistors irradiated with different gate bias voltages. The graph on the left is for 120/60 transistors and the graph on the right is for 360/60 transistors. The lines connecting points do not represent a fit, and are included only to make the plots easier to read. The transistor characteristics measured for transistors in one of the test ASIC packages after 754 Mrad was accumulated were all offset by current not likely to have passed through the transistors (this can be seen in Figure 5.6). Lines are not drawn through these points. The most likely source of these offsets is leakage current due to moisture caused by condensation on the cold ASIC package. 53

5.8 Transistor chararcteristic curves during the annealing period for (left) a 120/60 core PMOS and (right) a 1000/280 2.5 V NMOS. 53

5.9 The graph on the left shows the loss of maximum drain-source current during irradiation for 4 PMOS core transistors. The graph on the right shows the recovery of maximum drain-source current for the same 4 transistors during and after annealing. As in Figure 5.11, lines are included to make the plots easier to read. Once again, lines are not drawn through the points corresponding to measurements made after 754 Mrad of transistors in one of the ASIC packages. 54

5.10 The graph on the left shows the loss in maximum drain-source current after each irradiation step for 9 NMOS core transistors. The graph on the right shows the change in maximum drain-source current for the same 9 transistors during and after annealing. 54

5.11 The shift in threshold voltage for 8 NMOS I/O transistors irradiated to 878 MRad is shown in the graph on the left, while the graph on the right shows V_{th} for the same 8 transistors during and after annealing. No significant annealing was observed for the two zero V_{th} I/O transistors. 55

6.1 Observed and expected 95% confidence level upper limits on the product of the cross section and the branching fraction for the spin-0 radion obtained by different final states explored by the CMS Collaboration at $\sqrt{s} = 8$ TeV. Theory lines corresponding to different ultraviolet cutoffs are shown. 58

6.2 The trigger efficiency, as a function of m_{jj}^{red}, in the JetHT dataset and QCD MC for different $|\Delta\eta(\mathrm{j}_1, \mathrm{j}_2)|$ regions: $0.0 - 1.3$ (upper left), $0.0 - 0.434$ (upper right), $0.434 - 0.868$ (lower left), and $0.868 - 1.3$ (lower right). 63

6.3 The trigger efficiency in QCD MC for the baseline trigger HLT_PFJET260, as a function of m_{jj}^{red}, for different $|\Delta\eta(\mathrm{j}_1, \mathrm{j}_2)|$ regions: $0.0-1.3$, $0.0-0.434$, $0.434-0.868$, and $0.868 - 1.3$. The percentage difference between one and these turn-on curves is taken as an uncertainty on the trigger efficiency scale factor. 64

6.4 Efficiency to reconstruct a Cambridge-Aachen jet with a cone size of 0.8 (CA8) within $\Delta R < 0.1$ of a generated W boson, and the efficiency to reconstruct two anit-k_t jets with a 0.5 cone size (AK5) within $\Delta R < 0.1$ of the generated quarks from the W boson, as a function of the p_T of the W boson [10] Here, the fatjet is clustered with the CA algorithm but the reconstruction efficiency does not depend on the jet algorithm that is used to cluster the jets. Also, the same trend occurs for reconstructed Higgs bosons with large p_T, although the turnover in efficiency between a single fatjet and two smaller jets takes place at a slightly higher p_T due to the higher mass of the Higgs compared to the W boson. 67

6.5 Jet mass distributions of simulated QCD jets with $p_T > 300$ GeV for jets with different soft-drop parameters. The ungroomed jet mass is also shown [11]. 69

6.6 Distribution of τ_2/τ_1 in simulated samples of highly boosted W bosons and inclusive QCD jets after a jet mass selection of $60 < m_{jet} < 100$ GeV. Thick dashed lines represent the generator predictions without pileup interactions and without CMS detector simulation. The histograms are the expected distributions after full CMS simulation with pileup corresponding to an average number of 12 and 22 interactions [11]. Here, the W bosons decay to a pair of quarks, but the τ_{21} distribution is very similar for Higgs bosons decaying to a pair of b quarks. 70

6.7 Double-b tagger discriminant distribution in data and simulated samples for the double-muon tagged jets selection. Simulated events are normalized to the yield observed in data. The loose, medium and tight operating points are also reported. The bottom panel shows the ratio of the number of events observed in data to that of the MC prediction [7]. 71

6.8 The 95% confidence level expected upper limits as a function of bulk graviton resonance mass for different b-tagging categories. Note, when combining the TT category with other categories, the TT events are excluded, which is labeled as "TT exclusive." The limits using a subjet single b tagging selection (3b + 4b) are also shown for comparison. 73

6.9 The significance, $\frac{\epsilon_{\text{signal}}}{1+\sqrt{N_{\text{bkg}}}}$, of the $|\Delta\eta(\text{j}_1, \text{j}_2)|$ selection for various selection values as a function of the bulk graviton signal mass for the LL category (left) and the TT category (right). 74

6.10 The significance, $\frac{\epsilon_{\text{signal}}}{1+\sqrt{N_{\text{bkg}}}}$, of the $|\Delta\eta(\text{j}_1, \text{j}_2)|$ selection for various selection values as a function of the radion signal mass for the LL category (left) and the TT category (right). 74

6.11 The reduced di-jet mass distribution computed as described in Eqn. 6.3 compared to the standard di-jet invariant mass for simulated signal events. The m_{jj}^{red} distributions have a narrower di-jet mass distribution than the m_{jj} distribtuions for each mass point. The simulated bulk graviton mass points are 1000 (top left), 2000 (top right), and 3000 (bottom) GeV. 75

6.12 The reduced invariant di-jet mass distribution in simulated QCD, $\mathrm{t\bar{t}}$, and diboson events after the full event selection applied. The multijet background components for the different jet flavors are shown: events containing at least one jet with two B hadrons ($\mathrm{b\bar{b}}$) or a single one (b), events containing a jet having a charm hadron (c), and all other events (light). 77

6.13 The signal selection efficiencies for the bulk graviton and radion models for different mass hypotheses of the resonances, shown for the LL and the TT signal event categories. Owing to the large sample size of the simulated events, the statistical uncertainties are negligible. 78

6.14 Comparison of simulated events after the full selection excluding b-tagging, $|\Delta\eta(\mathrm{j_1},\mathrm{j_2})|$ (upper), m_{jj} (lower left), and m_{jj}^{red} (lower right). A signal cross section of 20 pb is assumed for each signal mass point. 79

6.15 Comparison of simulated events after the full selection excluding b-tagging, for the p_T (upper) and η (lower) of leading (left) and sub-leading (right) Higgs jets. A signal cross section of 20 pb is assumed for each signal mass point. 80

6.16 Comparison of simulated events after the full selection excluding b-tagging, for the soft-drop mass (upper) and the τ_{21} (lower) of the leading (left) and sub-leading (right) Higgs jets. A signal cross section of 20 pb is assumed for each signal mass point. 81

6.17 Comparison of simulated events after the full selection excluding b-tagging, for the double b-tagger discriminant of the leading (left) and sub-leading (right) Higgs jets. A signal cross section of 20 pb is assumed for each signal mass point. 81

6.18 Schematic representation of the regions used to perform the background estimate. . 82

6.19 The reduced invariant di-jet mass distribution in simulated QCD, t$\bar{\text{t}}$, and diboson events in the combined LL and TT anti-tag region. The multijet background components for the different jet flavors are shown: events containing at least one jet with two B hadrons (b$\bar{\text{b}}$) or a single one (b), events containing a jet having a charm hadron (c), and all other events (light). 82

6.20 Distribution in the pre-tag region of the leading jet double-b tagger discriminator vs soft-drop mass in QCD simulation. The red points represent the 50% quantile and show that there is a slight dependence of the double-b tagger on jet mass. 83

6.21 Distributions of m_{jj}^{red} in the signal and anti-tag regions for the LL category (left) and the TT category (right). Events are from QCD simulation and the distributions are normalized to unity to show that the distributions have similar shapes. 84

6.22 Distributions of m_{jj}^{red} in data normalized to unity in the $50 - 65$ GeV sideband (top left), the $65 - 80$ GeV sideband (top right), the $80 - 95$ GeV sideband (bottom left), and the $95 - 105$ GeV sideband (bottom right). 85

6.23 Distributions of m_{jj}^{red} in data normalized to unity in the $135 - 150$ GeV sideband (top left), the $150 - 165$ GeV sideband (top right), and the $165 - 200$ GeV sideband (bottom). 86

6.24 The pass-fail ratio in simulation of the leading p_T jet for the LL (left) and TT (right) signal region categories as a function of the difference between the soft-drop mass of the leading jet and the Higgs boson mass. The measured ratio in different bins of $m_{j_1} - m_H$ is used in the fit (red solid line), except in the region around $m_{j_1} - m_H = 0$, which corresponds to the signal region (blue markers). 87

6.25 The reduced mass distributions in simulation for the LL (left) and TT (right) signal region categories. The point with bars show the actual events in the signal region, while the histogram shows the estimated background and associated uncertainty. The difference between the events and the predicted background, divided by the statistical uncertainty is shown in the lower panels. 87

6.26 Reconstruction of QCD background in the presence of a bulk graviton signal with a cross section of 10 fb and bulk graviton mass of 1800 GeV. The background estimate is not biased by the signal. 88

6.27 The pass-fail ratio in the LL category from events in three different m_{jj}^{red} bins. The predicted pass-fail ratio in the Higgs mass window between all three cases agree with their uncertainties. 89

6.28 The ratio of events in the anti-tag region to events predicted in the signal region by the transfer factor is shown, binned in m_{jj}^{red}. The plot illustrates that there is no dependence on the pass-fail ratio as a function of di-jet mass. 90

6.29 (left) Fits in the mass sideband regions for the pass-fail ratio $R_{p/f}$ for (from top to bottom) the tight and loose working point. (right) Application of those fits to the anti-tag region to estimate the background in the control regions, compared with the true background (black markers). 91

6.30 Fits in the LL region in the signal (left) and anti-tag (right) regions from QCD as used by the AABH approach. The fits before (pre-fit) and after the likelihood fit are shown. The pre-fit curve is obtained using only the anti-tag region. 93

6.31 Fits in the TT region in the signal (left) and anti-tag (right) regions from QCD as used by the AABH approach. The fits before (pre-fit) and after the likelihood fit are shown. The pre-fit curve is obtained using only the anti-tag region. 93

6.32 Signal modeling for the radion (upper row) and bulk graviton (lower row) signal using the sum of a Gaussian and Crystal Ball functions. Shown are the probablity density functions (Pdfs) for the LL (left) and TT (right) categories. 94

6.33 The pass-fail ratio $R_{p/f}$ of the leading p_T jet for the LL (left) and TT (right) signal region categories as a function of the difference between the soft-drop mass of the leading jet and the Higgs boson mass, $m_{j1} - m_H$. The measured ratio in different bins of $m_{j_1} - m_H$ is used in the fit (red solid line), except in the region around $m_{j_1} - m_H = 0$, which corresponds to the signal region (blue triangular markers). The horizontal bars on the data points indicate the bin widths. 98

6.34 The reduced mass distributions m_{jj}^{red} for the LL (left) and TT (right) signal region categories. The points with bars show data, the histogram with a shaded band shows estimated background and associated uncertainty. The signal predictions for a bulk graviton of mass 1000 GeV, are overlaid for comparison, assuming a production cross section of 10 fb. The last bins of the distributions contain all events with $m_{jj}^{red} > 3000$ GeV. The difference between the data and the predicted background, divided by the data statistical uncertainty are shown in the lower panels. 99

6.35 The m_{jj}^{red} distributions in the anti-tag region for the LL (left) and TT (right) categories. The black markers are the data while the curves show the pre-fit and post-fit background shapes. The difference between the data and the predicted background, divided by the data statistical uncertainty are shown in the lower panels. 99

6.36 The m_{jj}^{red} distributions in the signal region for the LL (left) and TT (right) categories. The black markers are the data while the curves show the pre-fit and post-fit background shapes. The contributions of bulk gravitons of masses 1600 and 2500 GeV are shown assuming a production cross section of 10 fb. The difference between the data and the predicted background, divided by the data statistical uncertainty are shown in the lower panels. 100

6.37 The limits for the spin-0 radion (left) and the spin-2 bulk graviton (right) models. The result for $m_X < 1100$ GeV uses the background predicted by the Alphabet method, while for $m_X \geq 1100$ GeV the background is derived from the AABH method. The predicted theoretical cross sections for a narrow radion or a bulk graviton are also shown. 101

7.1 The limits for the spin-0 radion (left) and the spin-2 bulk graviton (right) from all resonant HH final states searched for with the CMS detector in the full 2016 dataset. The results present in this thesis are labeled as bbbb arXiv:1710.04960 [12]. 103

Chapter 1

Introduction

For millennia, humans have attempted to better understand the universe and explain phenomena that they observe within it. During this exploration, one of the questions that has always been asked is what are the fundamental constituents in nature? For most of our history, this question was answered through theoretical arguments. For example, in Ancient Greece, Lucretius and Democritus hypothesized that everything is composed of indivisible objects called atoms. This hypothesis was based on the empirical argument that matter is subject to irreversible decay and yet, new objects are created in nature, like a sapling sprouting from the ground, with identical properties to objects that have already decayed, like a fallen tree. Therefore, matter is made up of elements that are not visible to human senses and contain a substances properties.

However, as a more rigid scientific method developed, experimental evidence was needed to validate a hypothesis. This eventually led to John Dalton providing the first experimental evidence for the existence of atoms in the early 19th century. He found that elements always react in ratios of small whole numbers and therefore, elements must be reacting in whole number multiples of discrete units of atoms. Then in the late 19th century and early 20th century, Thomson and Rutherford experimentally showed that an atom contains negatively charged particles and a positively charged nucleus. These revelations were needed for the field of modern particle physics, the study of the fundamental building blocks of matter and how they interact, to begin.

As the 20th century continued, theoretical and experimental physics worked in unison to construct the Standard Model (SM) of particle physics. This theory put order to the numerous particles that had been discovered while also predicting the existence of new ones: the top quark, the tau neutrino, and the Higgs boson. Experimental physicists then set out to find these particles and this culminated with the 2012 discovery of the Higgs boson, a discovery that took place over 40 years after the original prediction.

However, despite the great predictive success of the SM, the theory has its shortcomings: gravity is not incorporated in it, it does not predict neutrino oscillations, and it does not contain a viable dark matter candidate. To address these issues, many new theories have been proposed that extend or build upon the SM, called beyond the SM (BSM) theories. There are numerous experiments that search for hints of these theories and particle accelerators have taken a prominent role in these searches. The current leading particle accelerator complex in the world is the Large Hadron Collider (LHC), which is where the Higgs boson was discovered. Unfortunately, no evidence for new theories has been detected yet. Nevertheless, the LHC has only collected a small fraction of the data it is expected to throughout its lifetime. Therefore, as the LHC continues to run, physicists must innovatively examine the data for BSM physics.

This thesis outlines the search for a new, heavy resonance decaying into pairs of standard model Higgs bosons using the Compact Muon Solenoid (CMS) detector at the LHC. Chapter 2 will layout the theoretical foundation for this search by defining the SM and the theories that predict heavy resonances. The LHC and the CMS detector will then be described in Chapter 3 followed by a summary of how events are reconstructed at CMS in Chapter 4. A brief aside will then be taken in Chapter 5 to outline radiation studies done on complimentary metal-oxide-semiconductors that will be installed in an upgrade of the CMS detector. Chapter 6 will completely describe the heavy resonance search and finally, a summary and outlook will be given in Chapter 7.

Chapter 2

The Standard Model of Particle Physics and Beyond

Currently, the Standard Model (SM) of particle physics is the most complete theory to describe the fundamental phenomena of the universe with a finite set of laws. It classifies all known elementary particles while also describing three of the four known ways that they can interact with each other. However, there is a substantial amount of evidence that there exists physics that is not described by the SM and there are numerous theories that connect this new, beyond the SM (BSM) physics to the SM with the Higgs boson. Therefore, the production of Higgs boson pairs (HH) provides an excellent signature in particle collisions to search for new physics. This chapter will first introduce the particles that make up the SM, along with its quantum field framework and how the Higgs boson fits within it. Then HH production within the context of the SM will be discussed and finally, a few BSM theories that enhance HH production will be outlined.

2.1 The Standard Model

The SM describes all observed fundamental particles of the universe as well as their interactions according to the electromagnetic, weak, and strong forces. The fundamental particles are classified as either fermions, half-integer spin particles, or bosons, integer spin particles, where fermions make up the matter of the universe and bosons are the force carriers. All particles in the SM can be seen in Figure 2.1[2].

There are twelve fermions in the SM which are further classified into two separate groups according to how they interact: six quarks which interact through the electromagnetic, weak, and

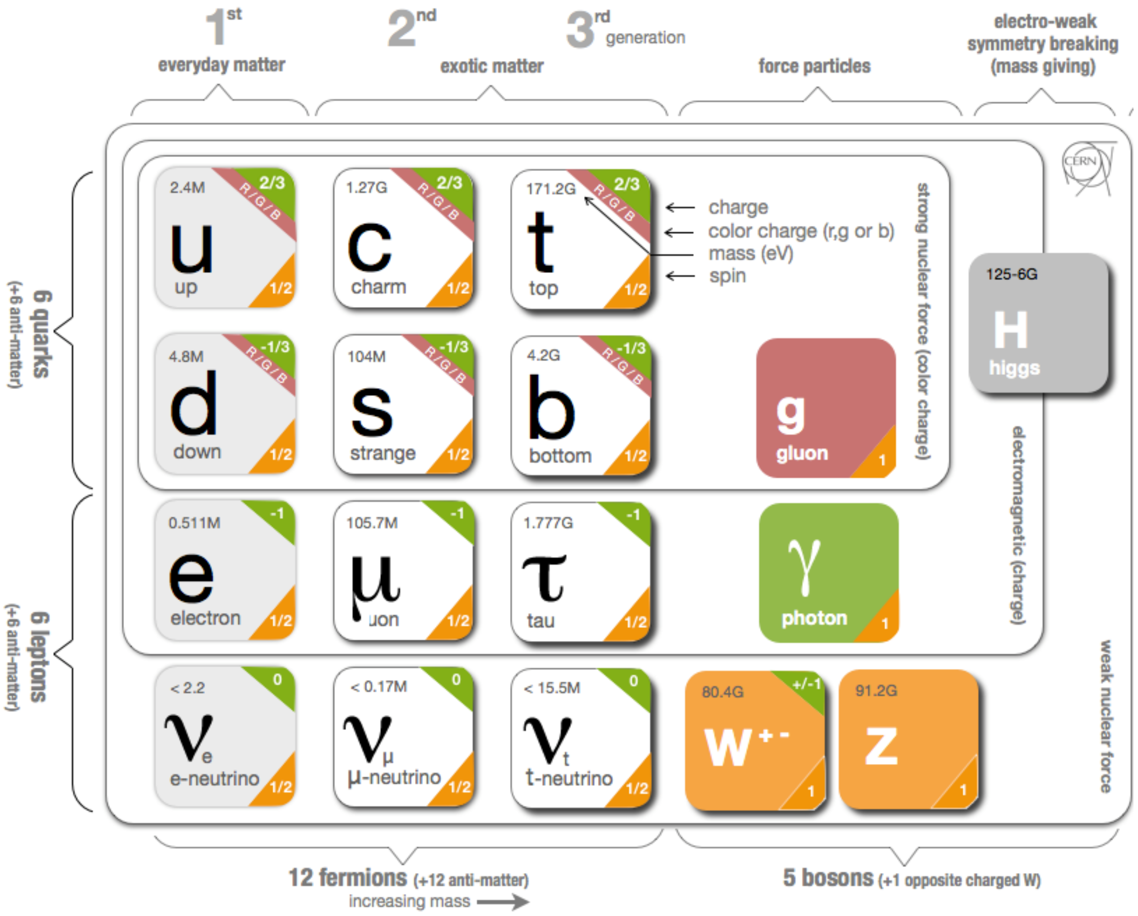
1st
everyday matter
2nd
exotic matter
3rd generation
force particles
electro-weak
symmetry breaking
(mass giving)
CERN
2.4M
2/3
R/G/B
u
up
1/2
1.27G
2/3
R/G/B
c
charm
1/2
171.2G
2/3
R/G/B
t
top
1/2
charge
color charge (r,g or b)
mass (eV)
spin
strong nuclear force (color charge)
125-6G
H
higgs
4.8M
-1/3
R/G/B
d
down
1/2
104M
-1/3
R/G/B
s
strange
1/2
4.2G
-1/3
R/G/B
b
bottom
1/2
g
gluon
1
electromagnetic (charge)
0.511M
-1
e
electron
1/2
105.7M
-1
μ
μon
1/2
1.777G
-1
τ
tau
1/2
γ
photon
1
< 2.2
0
ν_e
e-neutrino
1/2
< 0.17M
0
ν_μ
μ-neutrino
1/2
< 15.5M
0
ν_t
t-neutrino
1/2
80.4G
+/-1
W+-
1
91.2G
Z
1
weak nuclear force
6 quarks
(+6 anti-matter)
6 leptons
(+6 anti-matter)
12 fermions (+12 anti-matter)
increasing mass
5 bosons (+1 opposite charged W)

Figure 2.1: The quarks, leptons, and bosons that compose the Standard Model[2].

strong forces and six leptons which interact through the electromagnetic and weak forces. Also, each fermion has an antiparticle partner which has identical properties but opposite charge. The quarks and leptons are further grouped into 3 generations, where each generation contains a pair of particles. The generations of quarks contain one quark with a positive electric charge of +2/3 and one quark with a negative electric charge of -1/3. The first generation contains the positively-charged up (u) quark and the negatively charged down (d) quark, the second generation contains the positively-charged charm (c) quark and the negatively-charged strange (s) quark, and the third generation contains the positively-charged top (t) quark and negatively-charged bottom (b) quark. Each generation of quarks is identical except they have increasing mass and therefore, the second and third generation particles have short half-lives and are only observed in high energy environments. The first generation quarks make up all ordinary matter. For example, a proton contains two u quarks and one d quark. Since quarks interact through the strong force, they carry a color charge, analogous to electromagnetically interacting particles carrying an electromagnetic charge, and never appear individually in nature but are only found strongly bound to other quarks. This is a property called color confinement and will be discussed in more detail in Section 2.1.2. When quarks are bound together they form composite particles called hadrons. Hadrons can either be comprised of a quark-antiquark pair and gluons, called a meson, or three quarks and gluons, called a baryon. Protons and neutrons are examples of baryons that are found most often in the nature.

Each generation of leptons contains a particle with a -1 electric charge and the corresponding electrically neutral neutrino. Since neutrinos have no electric charge they only interact via the weak force and therefore rarely interact with other particles. The first lepton generation contains the electron (e) and electron neutrino (ν_e), the second generation contains the muon (μ) and muon neutrino (ν_μ), and the third generation contains the tau (τ) and tau neutrino (ν_τ). Again, increasing generations of leptons have increasing mass, except for the masses of the nuetrinos, which are unknown. Since the electrons are the lightest lepton they are stable and are the most common leptons found in the universe.

Forces in the standard model are described through particles exchanging gauge bosons. The gauge bosons have spin-1 and are the gluon (g), the photon (γ), and the $W^{\pm}$ and Z bosons. The gluon and photon are massless and mediate the strong force and electromagnetic force, respectively. The strong force binds quarks together to form nuclei and the electromagnetic force binds atoms and molecules together. There are two W bosons that carry a $+1$ electric charge (W^{+}) and a -1 electric charge (W^{-}), while the Z boson is electrically neutral. These three bosons are massive and mediate the weak force which is responsible for radioactive decay. Finally, the Higgs boson is a spin-0 scalar particle that generates the masses of the charged leptons and W and Z bosons through spontaneous symmetry breaking which will be described in Section 2.2.

The mathematical framework that describes all particles and forces of the SM is quantum field theory (QFT). The SM can be divided into two separate theories: electroweak theory, which describes the electromagnetic and weak forces, and quantum chromodynamics (QCD), which describes the strong force. The particles in these theories are described as fields in space-time and a Lagrangian describes the dynamics and kinematics of the theory. The SM is also a gauge theory, a type of field theory where the Lagrangian is invariant under certain gauge groups of transformations, described by the gauge group:

$$SU(3) \times SU(2) \times U(1), \tag{2.1}$$

where $SU(3)$ is the gauge group that describes QCD and $SU(2) \times U(1)$ describes electroweak theory.

2.1.1 Electroweak Theory

Electroweak theory unifies the electromagnetic force and the weak force. This implies that at high energies, like during the early universe, these two forces manifest as a single force and it's only as the universe cooled down that they separated into two distinct forces. Therefore, the electromagnetic force can also be described by a separate QFT called quantum electrodynamics

(QED). QED is invariant under $U(1)_{em}$, which is defined by the gauge transformation

$$\psi(x) \rightarrow e^{i\alpha(x)Q}\psi(x), \tag{2.2}$$

where $\alpha(x)$ is an arbitrary function of space and time and Q, the electric charge, is the generator for the group. The Lagrangian for this transformation can be derived by keeping the Dirac Lagrangian invariant under the transformation which leads to

$$\mathcal{L} = \bar{\psi}(i\gamma^{\mu}\partial_{\mu} - m)\psi + e\bar{\psi}\gamma^{\mu}A_{\mu}\psi - \frac{1}{4}F_{\mu\nu}F^{\mu\nu}, \tag{2.3}$$

where the first term represents the free propagation of a particle, ψ. The second term describes the interactions between the particle and a photon field, A_{μ}, and is proportional to the electromagnetic coupling constant, e. The final term represents the kinetic energy of the photon field, where $F_{\mu\nu} = \partial_{\mu}A_{\nu} - \partial_{\nu}A_{\mu}$. The photon is required to be massless because the addition of a mass term, $\frac{1}{2}m^2 A_{\mu}A^{\mu}$, would break gauge invariance.

To incorporate the weak force, a field theory is built that is invariant under $SU(2)_L \times U(1)_Y$. This gauge group is represented by the following transformations

$$\begin{aligned} \chi_L &\rightarrow e^{i\alpha(x)\cdot I + i\beta(x)Y}\chi_L, \\ \psi_R &\rightarrow e^{i\beta(x)Y}\psi_R, \end{aligned} \tag{2.4}$$

where these two transformations depend on the "handedness," or helicity, of a particle. The helicity is the dot product of the momentum and spin unit vectors, so a left-handed particle has helicity -1 and a right-handed particle has helicity $+1$. In the above transformations, I is the generator for $SU(2)_L$ and $I_i = \frac{\sigma_i}{2}$, where σ_i are the standard Pauli matrices. The hypercharge, Y, is the generator of $U(1)_Y$ and represents one of the charges of the electroweak interaction. The other charge is I_3, called weak isospin. Left-handed fermions, χ_L, form isospin doublets with weak isospin $\pm\frac{1}{2}$ and right-handed fermions, ψ_R, form isosinglets with weak isospin 0. These generators are related to the generator of QED by

$$Q = I_3 + \frac{Y}{2}. \tag{2.5}$$

The electroweak Lagrangian is

$$\begin{aligned}\mathcal{L} = &-\frac{1}{4}W^i_{\mu\nu} \cdot W^{\mu\nu}_i - \frac{1}{4}B_{\mu\nu}B^{\mu\nu} \\ &+ \chi_L \gamma^\mu (i\partial_\mu - \frac{g}{2}\sigma_i W^i_\mu - g'\frac{Y}{2}B_\mu)\chi_L \\ &+ \psi_R \gamma^\mu (i\partial_\mu - g'\frac{Y}{2}B_\mu)\psi_R,\end{aligned} \tag{2.6}$$

where $W^i_{\mu\nu} \equiv \partial_\mu W^i_\nu - \partial_\nu W^i_\mu - g\epsilon_{ijk}W^j_\mu W^k_\nu$, $B_{\mu\nu} \equiv \partial_\mu B_\nu - \partial_\nu B_\mu$, and g and g' are the coupling constants for $SU(2)_L$ and $U(1)_Y$, respectively. The mediators are the three massless W^i bosons which form a weak isospin triplet and a massless B^0 boson which forms a weak isospin singlet. These massless bosons become the massive $W^\pm$ and Z bosons and the massless photon through the Brout-Englert-Higgs mechanism which will be described in more detail in Section 2.2. The large mass of the $W^\pm$ and Z bosons causes them to be short-lived particles and therefore, the weak force is a short range force. Following the same logic, since the photon is massless the electromagnetic force is a long-range interaction.

2.1.2 Quantum Chromodynamics

The strong force is described by QCD, a field theory that is invariant under the $SU(3)$ gauge group. Particles that interact through this force can carry three types of color charge, “red,” “green,” or “blue,” which are represented as rotations according to $SU(3)$. This gauge group is represented by the gauge transformation

$$\psi(x) \rightarrow U\psi(x) \equiv e^{i\alpha_a T_a}\psi(x), \tag{2.7}$$

where U is a 3×3 unitary matrix and T_a, where $a = 1, ...8$, are the group generators which are hermitian matrices and satisfy the relation

$$[T_a, T_b] = i f_{abc} T_c, \tag{2.8}$$

where f_{abc} is the structure constant of the $SU(3)$ group. To remain invariant under this transformation, the QCD Lagrangian is written as

$$\mathcal{L} = \bar{\psi}(i\gamma^\mu \partial_\mu - m)\psi - g_s(\bar{\psi}\gamma^\mu T_a \psi)A^a_\mu - \frac{1}{4}G^\alpha_{\mu\nu}G^{\mu\nu}_\alpha, \tag{2.9}$$

which has a very similar form to the QED Lagrangian. The first term describes the free propagation of a quark and the second term represents the interactions between a quark and the vector gluon field, A^α_μ, and is proportional to the strong coupling constant, g_s. The final term represents the kinetic energy of the gluon field, where $G^\alpha_{\mu\nu} = \partial_\mu A^\alpha_\nu - \partial_\nu A^\alpha_\mu - g_s f_{abc} A^b_\mu A^c_\nu$, and therefore, there are cubic and quartic self-interactions of gluon fields represented in this term.

These self-interaction terms are the key difference between QCD and QED and give rise to a couple phenomena that are unique to QCD. One of these features is called asymptotic freedom, which states that the interaction between two quarks becomes smaller as the distance decreases. This can be explained by comparing the QCD and QED equivalents. In QED, a lone particle with an electromagnetic charge in a vacuum causes the vacuum to become polarized and therefore, the charge of the particle appears smaller as the distance from the particle increases. This is called the screening effect. The same effect happens in QCD when a particle with color charge sits alone in a vacuum. However, there is an additional antiscreening effect caused by the gluon self-interaction that overpowers the screening effect. Therefore, the further the distance from a color charge the larger the charge appears, or in other words, the coupling constant decreases as the distance decreases or the momentum scale increases.

Another property of QCD, called color confinement, is that no free particle can have a non-neutral color charge. This means that quarks only exist bound together in hadrons and when they try to separate in high energy collisions they behave like a spring, where the energy builds up between them as they separate. Eventually, this energy is large enough to produce a quark-antiquark pair in a process called hadronization.

2.2 The Brout-Englert-Higgs Mechanism

The Brout-Englert-Higgs (BEH) mechanism [13, 14] was proposed to fix the discrepancy between the electroweak theory and what is observed in reality. As stated in Section 2.1.1, electroweak theory predicts four bosons that are required to be massless due to gauge invariance but only one massless boson and three massive ones exist. The BEH mechanism generates the masses for these bosons while also generating the masses of the fermions by spontaneously breaking the $SU(2)_L \times U(1)_Y$ symmetry. This is done by introducing a complex scalar field that is a doublet of $SU(2)$

$$\Phi = \begin{pmatrix} \phi^+ \\ \phi^0 \end{pmatrix} \tag{2.10}$$

and its corresponding Lagrangian

$$\mathcal{L} = (D_\mu \Phi)^\dagger (D^\mu \Phi) - V(\Phi^\dagger \Phi), \tag{2.11}$$

where $D_\mu \equiv \partial_\mu - ig\frac{\sigma_i}{2}W^i_\mu - \frac{i}{2}g' B_\mu$. This Lagrangian is invariant under $SU(2)_L \times U(1)_Y$ transformations, so it can be added to the electroweak Lagrangian. The potential, $V(\Phi^\dagger\Phi)$, is defined as

$$V(\Phi^\dagger \Phi) = \mu^2 \Phi^\dagger \Phi + \lambda (\Phi^\dagger \Phi)^2, \tag{2.12}$$

where $\lambda > 0$ implies that the potential has a minimum. In QFT, the ground state is the vacuum and is found by minimizing the potential, which gives the vacuum expectation value (VEV) of Φ. Taking $\mu^2 > 0$ causes the potential to only have a minimum at $\Phi^\dagger\Phi = 0$ and no spontaneous symmetry breaking can occur. Therefore, μ^2 is required to be less than zero and the minimum of the potential occurs when $\Phi^\dagger\Phi = -\frac{\mu^2}{2\lambda}$. This means there are a degenerate set of ground states with a VEV, v, equal to $\sqrt{-\frac{\mu^2}{2\lambda}}$ and choosing a specific ground state leads to spontaneous symmetry breaking of $SU(2)_L \times U(1)_Y$. Selecting

$$\Phi_0 = \begin{pmatrix} 0 \\ v \end{pmatrix} \tag{2.13}$$

as a ground state allows the scalar field to be invariant under the $U(1)_{em}$ symmetry group since the VEV is only given to the neutral component of Φ. Expanding Φ around the minimum, v, gives

$$\Phi(x) = \frac{1}{\sqrt{2}} e^{i\sigma_i \theta^i(x)/\nu} \begin{pmatrix} 0 \\ \nu + H(x) \end{pmatrix}, \tag{2.14}$$

where a new Higgs field, $H(x)$, and three Goldstone bosons, $\theta^i(x)$, have been introduced. These Goldstone bosons are predicted by the Goldstone theorem [15], which states that massless scalars occur whenever a continuous symmetry is spontaneously broken. Since the Lagrangian is locally $SU(2)_L$ invariant, the three $\theta^i(x)$ fields can be rotated away making these massless excitations unphysical and leaving the ground state as

$$\Phi(x) = \frac{1}{\sqrt{2}} \begin{pmatrix} 0 \\ \nu + H(x) \end{pmatrix}. \tag{2.15}$$

When this ground state is substituted into the Lagrangian in Eq. 2.11, the kinetic piece takes the form

$$\frac{1}{2}\partial_\mu H \partial^\mu H + (v+H)^2 \Big\{ \frac{g^2}{4} W_\mu^+ W^{\mu-} + \frac{1}{8}(g^2 + g'^2) Z_\mu Z^\mu \Big\} \tag{2.16}$$

where the physical gauge fields are defined in terms of the massless mediators as:

$$W_\mu^\pm = \frac{1}{\sqrt{2}}(W_\mu^1 \mp W_\mu^2), \tag{2.17}$$

$$Z_\mu = \frac{1}{\sqrt{g^2+g'^2}}(gW_\mu^3 - g'B_\mu), \tag{2.18}$$

$$A_\mu = \frac{1}{\sqrt{g^2+g'^2}}(gW_\mu^3 + g'B_\mu). \tag{2.19}$$

Therefore, A_μ remains massless, corresponding to the massless γ, and the $W^\pm$ and Z fields acquire masses of $\frac{1}{2}vg$ and $\frac{1}{2}v\sqrt{g^2+g'^2}$, respectively. The three massive gauge bosons have absorbed a degree of freedom from the Goldstone bosons and acquired mass in the process.

The remaining portion of the Lagrangian from Eq. 2.11 after the substitution of the chosen ground state describes the real, scalar Higgs field and is written as

$$\mathcal{L} = \frac{1}{2}\partial_\mu H \partial^\mu H - \lambda v^2 H^2 - \lambda_{HHH} v H^3 - \frac{\lambda_{HHHH}}{4} H^4. \tag{2.20}$$

From this equation, the Higgs field has mass, $m_H = 2\lambda v^2$, which can only be determined experimentally since λ is a free parameter. Another feature of this equation of motion is that there are two Higgs self-coupling terms completely determined by the mass of the Higgs and the VEV. Therefore, measuring the self-coupling is a crucial test of electroweak symmetry breaking.

Finally, the masses of fermions from the electroweak theory need to be addressed. This is done by introducing the $SU(2)_L \times U(1)_Y$ invariant Yukawa Lagrangian

$$\mathcal{L} = -\lambda_f(\bar{\chi}_L \Phi \phi_R + \bar{\phi}_R \Phi \chi_L) - \lambda_{f'}(\bar{\chi}_L \widetilde{\Phi} \phi_R + \bar{\phi}_R \widetilde{\Phi} \chi_L), \tag{2.21}$$

where the conjugate of Φ, $\widetilde{\Phi} = -i\sigma_2 \Phi^*$, and the Yukawa coupling to two different fermions, λ_f and $\lambda_{f'}$, have been introduced. Substituting the same ground state as before from Eq. 2.15, the Lagrangian becomes

$$\mathcal{L} = -\frac{\lambda_f}{\sqrt{2}}(v+H)(\bar{\psi}_L \psi_R + \bar{\psi}_R \psi_L), \tag{2.22}$$

where this has been written for the general fermion field, ψ. Therefore, the mass term for a fermion, f, has the general form $\frac{\lambda_f v}{\sqrt{2}}(\bar{\psi}_L\psi_R + \bar{\psi}_R\psi_L)$ and the mass is $\frac{\lambda_f v}{\sqrt{2}}$. There is also an additional term that couples the Higgs scalar to a fermion and changes the chirality of the fermion. The coupling is proportional to the mass of the fermion and is a free parameter in the SM.

2.3 The Higgs Boson

In 2012, nearly 40 years after the BEH mechanism was proposed, the Higgs boson was discovered by the CMS and ATLAS Collaborations at the LHC [16, 3]. The discovery was made by combining five different Higgs decay modes, $\gamma\gamma$, ZZ, W^+W^-, $\tau^+\tau^-$, and $b\bar{b}$, from data produced in proton-proton (pp) collisions with a center-of-mass energy of 7 and 8 TeV($\sqrt{s} = 7$ and 8). Despite having smaller branching fractions, which can be seen in Table 2.1, the two leading contributions to the discovery were the $\gamma\gamma$ and $ZZ \to 4l$ channels due to the clean signature of these decays. The invariant mass distributions for these two channels from the CMS experiment are shown in Figure 2.2 and a clear bump in the data can be seen at 125 GeV. The CMS and ATLAS experiments combined to measure the mass of the Higgs [17] as

$$m_H = 125.09 \pm 0.21(stat.) \pm 0.11(syst) \text{ GeV}. \tag{2.23}$$

This discovery was a great success for the SM and many properties of the new scalar boson were measured [18, 19] to confirm that it is consistent with the SM Higgs boson. For example, the spin and parity of the particle, the total decay width, the coupling strengths to fermions and vector bosons, and the differential production cross sections have all been probed and have thus far been shown to agree with SM predictions [4]. The CMS and ATLAS combined measurements of the Higgs coupling strengths can be seen in Figure 2.3.

One of the remaining Higgs measurements needed to demonstrate that the discovered Higgs is consistent with the SM Higgs is of the Higgs self-coupling, λ_{HHH}. This is a crucial test to verify that the discovered Higgs is represented by the Lagrangian in Eq. 2.11. The Higgs self-coupling can only be directly accessed by measuring Higgs pair production (HH) and therefore, measuring HH production is an essential step to verify the BEH mechanism.

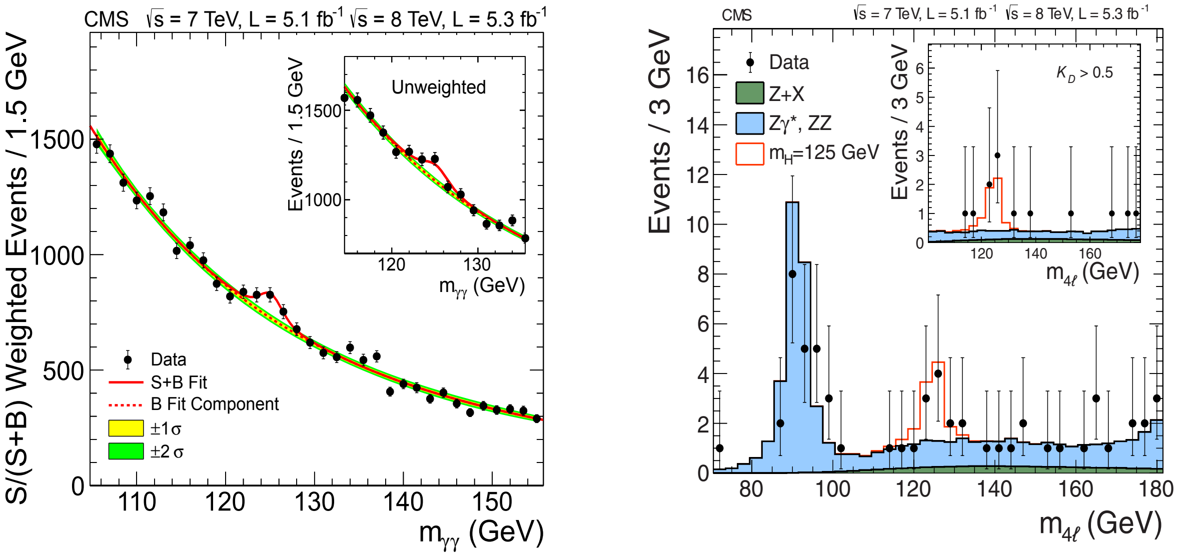

Figure 2.2: (Left) The invariant diphoton mass distribution with each event weighted by the $\frac{S}{S+B}$ value of its category. The lines represent the fitted background and signal, and the colored bands represent the ±1 and ±2 standard deviation uncertainties in the background estimate. (Right) Distribtuon of the four-lepton invariant mass for the $ZZ \rightarrow 4l$ analysis. The points represent the data, the filled histograms represent the background, and the open histogram show the signal expectation for a Higgs boson of mass $m_H = 125$ GeV [3].

2.4 Higgs Boson Pair Production

At $\sqrt{s} = 13$ TeV the HH production cross section, σ_{HH}, is only ∼35 fb, about 1000 times smaller than SM Higgs production cross sections, making this measurement extremely challenging and possibly not feasible during the planned lifetime of the LHC. To further impede the measurement of λ_{HHH}, there are two leading diagrams that contribute to HH production and only one of them contains the tri-Higgs vertex. The other diagram contains Higgs coupling to top quarks and disentangling these processes further reduces the sensitivity of HH searches to λ_{HHH}. However, there are many BSM theories that predict an enhancement to the HH signal and it is necessary to conduct HH searches to verify that BSM physics is not involved in electroweak symmetry break-

Decay mode	Branching fraction (%)
$b\bar{b}$	$58.4^{+3.2}_{-3.3}$
W^+W^-	$21.4^{+4.3}_{-4.2}$
gg	$8.19^{+5.1}_{-5.1}$
$\tau^+\tau^-$	$6.27^{+5.7}_{-5.7}$
$c\bar{c}$	$2.89^{+5.5}_{-2.0}$
ZZ	$2.62^{+4.3}_{-4.1}$
$\gamma\gamma$	$0.227^{+5.0}_{-4.9}$
$Z\gamma$	$0.153^{+9.0}_{-8.9}$
$\mu^+\mu^-$	$0.0218^{+6.0}_{-5.9}$

Table 2.1: Predicted branching fractions for the Higgs boson with a mass of 125 GeV. The relative uncertainties are calculated from theoretical predictions that depend on the uncertainties of α_s, the quark masses, and the Higgs boson partial decay widths.

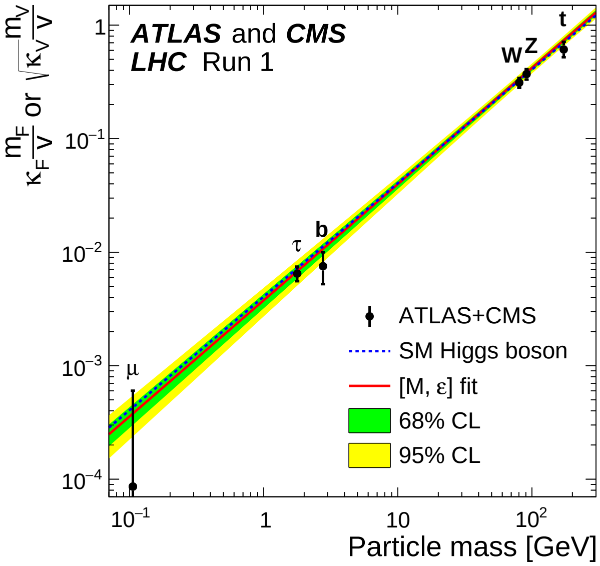

Figure 2.3: Best fit values as a function of particle mass for the combination of ATLAS and CMS data, with parameters defined as $\kappa_F \cdot m_F/v$ for the fermions and as $\sqrt{\kappa_V} \cdot m_V/v$ for the weak vector bosons, where $v = 246$ GeV is the vacuum expectation value of the Higgs field. Here $\kappa_F = \lambda_f$ from Equation 2.22 and κ_V corresponds to the coupling of the vector bosons to the Higgs, which depends on g and g' from Equations 2.16. [4].

ing. Furthermore, the SM only predicts non-resonant HH produciton so any sign of resonant HH production would a clear indication of BSM physics.

2.4.1 Standard Model Production

At the LHC, there are five main processes that contribute to HH production: gluon fusion, vector boson fusion, double Higgs-strahlung, and top pair and single top production in association with HH production. The cross section for these process can be seen in Table 2.2 for a center-of-mass energy of 13 and 14 TeV. Gluon fusion is the leading production mechanism and the two leading diagrams for this process are in Figure 2.4, where the box diagram on the right has the larger cross section. These diagrams have quark loops in them that are dominated by top quarks and therefore, the cross section for this process depends on λ_{HHH} and the top quark Yukawa coupling. Also, these diagrams interfere destructively causing the low production cross section. This makes searches for HH production intriguing since any observation would be a clear indication of BSM physics.

	$\sqrt{s} = 13$ TeV	$\sqrt{s} = 14$ TeV
Gluon Fusion	$33.49^{+4.3+2.1+2.3\%}_{-6.0-2.1-2.3\%}$	$39.59^{+4.4+2.1+2.2\%}_{-6.0-2.1-2.2\%}$
Vector Boson Fusion	$1.62^{+2.3+2.3\%}_{-2.7-2.3\%}$	$1.95^{+1.8+2.4\%}_{-2.3-2.4\%}$
$t\bar{t}HH$	$0.772^{+1.7+3.2\%}_{-4.5-3.2\%}$	$0.949^{+1.8+3.2\%}_{-4.8-3.2\%}$
ZHH	$0.362^{+3.4+1.9\%}_{-2.6-1.9\%}$	$0.414^{+3.5+1.8\%}_{-2.7-1.8\%}$
W^+HH	$0.329^{+0.32+2.2\%}_{-0.41-2.2\%}$	$0.368^{+0.33+2.1\%}_{-0.39-2.1\%}$
W^-HH	$0.173^{+1.2+2.8\%}_{-1.3-2.8\%}$	$0.197^{+1.2+2.7\%}_{-1.3-2.7\%}$
$tjHH$	$0.0281^{+5.2+4.5\%}_{-3.2-4.5\%}$	$0.0364^{+3.7+4.7\%}_{-1.3-4.7\%}$

Table 2.2: Cross sections (in fb) for the seven largest Higgs pair production channels at the LHC, with $\sqrt{s} = 13$ and 14 TeV. The first uncertainty is the scale uncertainty, the second is the PDF uncertainty, and the third for gluon fusion is the α_s uncertainty. The gluon fusion, ZHH, and $W^{\pm}HH$ channels have been calculated at next-to-next-to-leading-order (NNLO) QCD and the vector boson fusion, $ttHH$, and $tjHH$ channels have been calculated at next-to-leading-order (NLO) QCD [1].

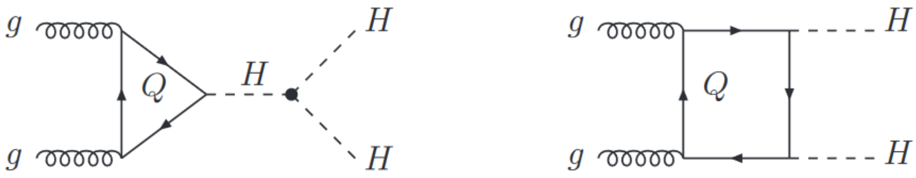

Figure 2.4: The two leading HH production diagrams for gluon fusion [5].

2.4.2 Beyond the Standard Model Production

The HH process is theoretically predicted by numerous BSM scenarios and can be observed in two distinct signatures, resonant and non-resonant. A resonant signature would manifest as an enhancement of σ_{HH} at a specific resonance mass, m_X. A non-resonant BSM signature would produce an overall enhancement of σ_{HH} across a wide range of m_X values. Since this thesis describes a search for resonant production, this section will only focus on resonant BSM production.

The BSM theories that predict the existence of a new resonance X decaying to a pair of Higgs bosons allow for a wide range of possible masses. This range spans from the kinematic limit, which is twice the Higgs mass, up to several TeV. Due to this large range, different search techniques must be employed to completely cover it. This analysis is a model independent search for a heavy resonance, with a mass from just below a TeV up to a couple of TeV, and therefore this section will focus on BSM theories that predict these types of particles. This section is not meant to be a complete description of every BSM model that predicts this HH signature, but rather an illustration that this search is well motivated by many different types of theories.

2.4.2.1 Warped Extra Dimensions

In order to solve the hierarchy problem, the large discrepancy between the weak force and gravity, Randall and Sundrum [20] proposed a warped extra dimension (WED) model where there is one extra spatial dimension compactified between two fixed points, called branes. The region between the branes is referred to as bulk and controlled through an exponential metric, which is written as

$$ds^2 = e^{-2kl\phi}\eta_{\mu\nu}dx^\mu dy^\nu + l^2 d\phi^2, \tag{2.24}$$

where l is the size of the extra dimension. The gap between the two fundamental scales of nature, such as the Planck scale (M_{Pl}) and the electroweak scale, is controlled by a warp factor, k, in the metric, which corresponds to one of the fundamental parameters of the theory. One of the branes, where the density of the extra dimensional metric is localized, is called the "Planck brane", while the other, where the Higgs field is localized, is called the "TeV brane". This type of model predicts the existence of new particles, such as the spin-0 radion [21, 22, 23] and the spin-2 first Kaluze-Klein (KK) excitation of the graviton [24, 25, 26].

There are two possible ways of describing a KK bulk graviton, which would also be the mediator of the gravitational force, from the standpoint of a WED that depends on the choice of localization of the SM matter fields. In the "RS1 model", only gravity is allowed to propagate in the extra-dimensional bulk, and the couplings of the KK graviton to matter fields are fully defined by $k/\overline{M}_{Pl}$, where $\overline{M}_{Pl} \equiv M_{Pl}/\sqrt{8\pi}$. If other fields are allowed to propagate in the bulk, the "bulk RS model", the coupling of the KK graviton to matter depends on the localization of the SM fields in the bulk. This model is favored because only the Higgs is on the TeV brane which allows high energy unification of gauge couplings and a natural mass hierarchy. For example, the light quarks are localized near the Planck brane while the top quarks are localized near the TeV brane, the elementary top hypothesis, causing a large top mass.

The radion is an additional element of WED models that is needed to stabilize the size of the extra dimension l and the radion's properties are similar between the two WED models. It is standard to express the benchmark points of the radion in terms of the dimensionless quantity $k/\overline{M}_{Pl}$, and the mass scale $\Lambda_R = \sqrt{6}e^{-kl}\overline{M}_{Pl}$, with the latter interpreted as the ultraviolet cutoff of the theory [27]. The addition of a scalar-curvature term can induce a mixing between the scalar radion and Higgs boson [28], but due to electroweak precision tests this mixing is expected to be small.

In proton-proton collisions at the LHC, the KK graviton and radion are produced primarily through gluon-gluon fusion. The KK gravition is predicted to decay to a pair of Higgs with a branching fraction of up to ∼10% depending on the type of model and model parameters [29]. While the radion has an HH branching fraction of ∼25% that is roughly constant across models. The absolute value for the production cross section scales with $(k/\overline{M}_{Pl})^2$ for the KK gravition [29] and with $1/\Lambda_R^2$ for the radion [30].

2.4.2.2 Higgs Singlet

The simplest extension of the SM Higgs sector is done by adding a real singlet field, S [31]. The scalar potential is then

$$V(\Phi, S) = -m^2\Phi^\dagger\Phi - \mu^2 S^2 + \lambda_1(\Phi^\dagger\Phi)^2 + \lambda_2 S^4 + \lambda_3\Phi^\dagger\Phi S^2, \tag{2.25}$$

where Φ is the complex scalar doublet of $SU(2)$ from the SM. In the unitary gauge, the Higgs fields are given by

$$\Phi = \begin{pmatrix} 0 \\ \frac{\widetilde{h}-\nu}{\sqrt{2}} \end{pmatrix}, \tag{2.26}$$

$$S = \frac{h' + x}{\sqrt{2}}, \tag{2.27}$$

where ν and x are the vacuum expectation values for the Φ and S fields, respectively. The gauge and mass eigenstates are then related by the mixing matrix

$$\begin{pmatrix} h \\ H \end{pmatrix} = \begin{pmatrix} \cos\alpha & -\sin\alpha \\ \sin\alpha & \cos\alpha \end{pmatrix} \begin{pmatrix} \widetilde{h} \\ h' \end{pmatrix}, \tag{2.28}$$

where h represents the SM Higgs and H is a new, additional Higgs. The free parameters in this model are m_h, m_H, $\sin\alpha$, ν, and x. When $m_H > 2m_h$, the $H \rightarrow hh$ decay is allowed and the second

Higgs is decoupled from other SM particles [32]. In this scenario, the second Higgs is primarily produced through gluon fusion and can have a mass from $250 - 1000$ GeV. The branching fraction of H to two SM Higgs is up to 40% depending on the parameters of the model.

2.4.2.3 Georgi-Machacek Model

The Georgi-Machacek (GM) model [33] is a more complicated extension of the Higgs sector where a real triplet field, ξ, with hypercharge $Y = 0$ and a complex $SU(2)_L$ triplet field, χ, with hypercharge $Y = 1$ are added. This is an interesting model because the triplet fields can have vacuum expectation values which leads to neutrinos having light Majorana masses. The model also predicts the existence of three neutral scalars, two that are CP-even and one that is CP-odd. At the LHC, the production of one of these CP-even scalars is dominated by gluon fusion. This scalar can be as heavy as 1 TeV and it decays to a pair of Higgs bosons with a branching fraction that can be as large as ∼95% depending on the mass of the scalar. The GM model has the intriguing phenomenological feature that the couplings between the SM Higgs and the SM weak gauge bosons are enhanced, meaning that precision measurements of Higgs couplings could also give evidence to this model [34].

Chapter 3

Experimental Setup

3.1 The Large Hardon Collider

The Large Hadron Collider (LHC) accelerates protons and heavy ions in counter rotating beams to near-light speeds. These beams are contained in vacuum tubes that form a closed path 26.7 km in circumference and are housed between 50 and 175 m underground, near the France-Switzerland border. The beams cross at four interaction points where four different detectors are located.

In ideal conditions, each beam contains 2,808 bunches of protons and each bunch contains about 100 billion protons. These bunches are formed from the 16 radio-frequency (RF) cavities located on the beamline. The path and shape of the beam are controlled by about 9,600 magnets. Dipole magnets keep the beams on their circular path, while quadrupole magnets focus the beams. In order for the superconducting dipole magnets to provide a high magnetic field of 8.3 T, they must be kept at 1.9 K with superfluid Helium.

The design instantaneous luminosity, $\mathcal{L}$, is $10^{34}\text{cm}^{-2}\text{s}^{-1}$ and only depends on beam parameters

$$\mathcal{L} = \frac{N_b^2 n_b f_{rev} \gamma_r}{4\pi \varepsilon_n \beta} F, \tag{3.1}$$

where N_b is the number of particles per bunch, n_b is the number of bunches per beam, f_{rev} is the frequency of the revolutions of the beam, γ_r is the relativistic factor, ε_n is the normalized transverse beam emittance, β is the beta function at the collision point and is roughly the width of the beam squared divided by the emittance, and F is the geometric luminosity reduction factor due to the crossing angle at the interaction point [35]. Integrating the instantaneous luminosity with respect to time gives the integrated luminosity:

$$L = \int \mathcal{L}(t)dt. \tag{3.2}$$

In 2016, the LHC provided 35.9 fb^{-1} of integrated luminosity and a similar amount is expected in 2017. This luminosity is delivered with a bunch spacing of 25 ns and a center of mass energy of 13 TeV. To achieve this, electrons are stripped off of Hydrogen atoms by an electric field and the remaining protons are injected into a linear accelerator (LINAC 2) where they reach an energy of 50 MeV. The beam is then sent to the Proton Synchrotron Booster (PSB), which accelerates the protons to 1.4 GeV. Afterwards, the beams are injected into the Proton Synchrotron (PS) where they reach 25 GeV, followed by the Super Proton Synchrotron (PSP) where they are accelerated to 450 GeV. The beams are then accelerated in the main ring to 6.5 TeV. A layout of the acceleration facility can be seen in Figure 3.1[36].

3.2 The Compact Muon Solenoid Detector

The Compact Muon Solenoid (CMS) detector is one of the general-purpose particle detectors at the LHC. It is made up of layered, sub-detectors arranged in a cylindrical structure that is 21.6 m long, 15 m in diameter and weighs about 14,000 tons. The detector is built around its huge solenoid magnet which provides a 3.8 T magnetic field. Due to the size of this magnet, the silicon tracker, the lead tungstate crystal electromagnetic calorimeter (ECAL), and the brass and plastic scintillator hadron calorimeter (HCAL) are all able to fit within the solenoid, allowing the momentum of particles to be precisely measured. Encasing the solenoid is the muon detector system composed of different types of gas-ionization detectors. A layout of the CMS detector can be seen in Figure 3.2.

The experiment uses a right-handed, Cartesian coordinate system that is oriented with the x-axis pointing to the center of the LHC ring, the y-axis pointing up, and the z-axis pointing along the beam line. A pseudo-polar coordinate system is also used due to the cylindrical symmetry of the

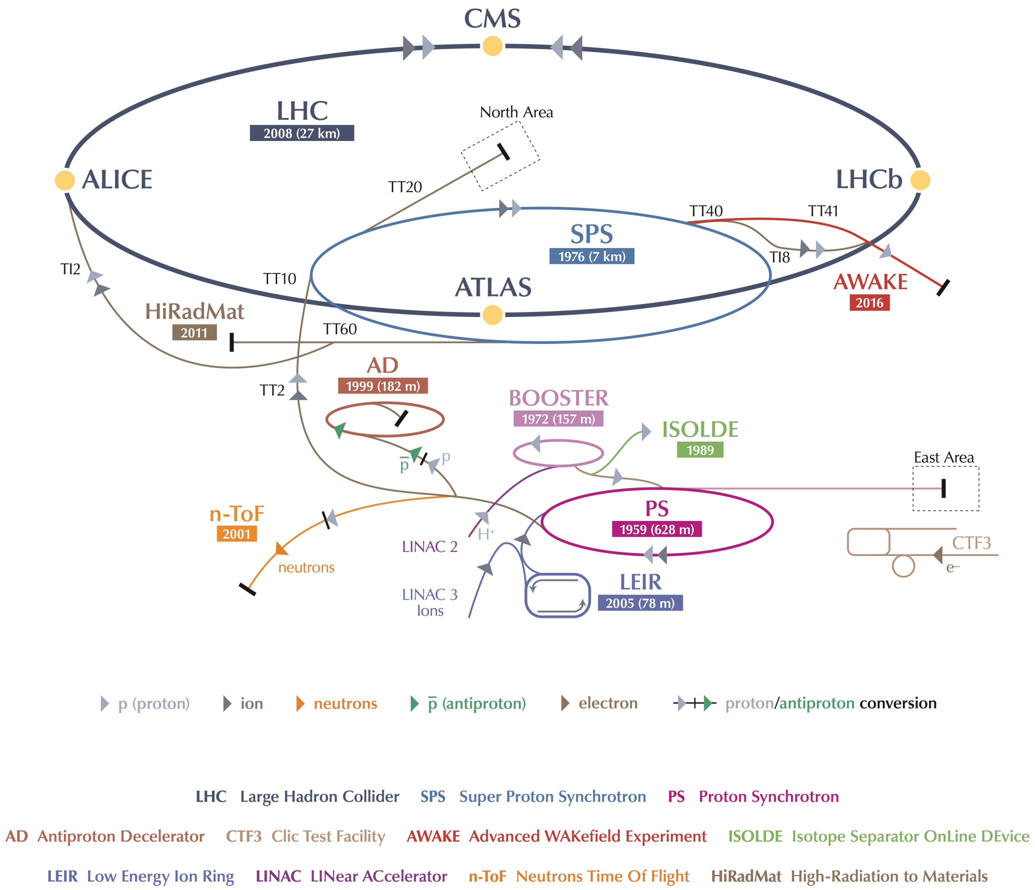
CMS
LHC
2008 (27 km)
North Area
ALICE
LHCb
TT20
TT40
TT41
SPS
1976 (7 km)
TI8
TI2
TT10
ATLAS
AWAKE
2016
HiRadMat
2011
TT60
AD
1999 (182 m)
TT2
BOOSTER
1972 (157 m)
ISOLDE
1989
East Area
p̄
p
n-ToF
2001
PS
1959 (628 m)
CTF3
e–
LINAC 2
H+
neutrons
LINAC 3
Ions
LEIR
2005 (78 m)
p (proton)
ion
neutrons
p̄ (antiproton)
electron
proton/antiproton conversion
LHC Large Hadron Collider
SPS Super Proton Synchrotron
PS Proton Synchrotron
AD Antiproton Decelerator
CTF3 Clic Test Facility
AWAKE Advanced WAKefield Experiment
ISOLDE Isotope Separator OnLine DEvice
LEIR Low Energy Ion Ring
LINAC LINear ACcelerator
n-ToF Neutrons Time Of Flight
HiRadMat High-Radiation to Materials

Figure 3.1: A schematic of the accelerator chain.

detector. The azimuthal angle, ϕ, is measured from the x-axis in the x-y plane, the polar angle, θ, is defined from the z-axis, and the pseudorapidity, η, is given by $\eta = -\ln\tan(\theta/2)$. The transverse plane is used to define the component of observable quantities, like momentum and energy, that is perpendicular to the beamline in the x-y plane.

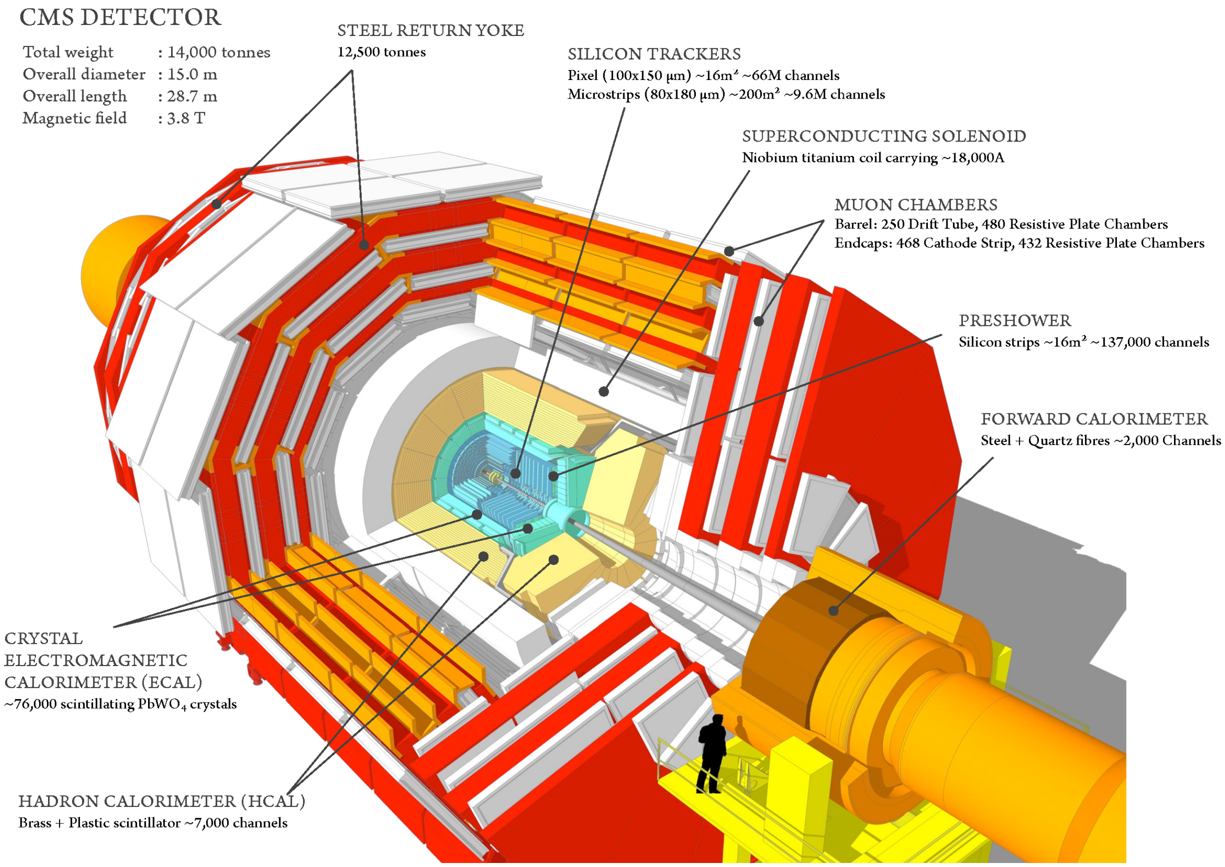
CMS DETECTOR
Total weight : 14,000 tonnes
Overall diameter : 15.0 m
Overall length : 28.7 m
Magnetic field : 3.8 T
STEEL RETURN YOKE
12,500 tonnes
SILICON TRACKERS
Pixel (100x150 μm) ~16m² ~66M channels
Microstrips (80x180 μm) ~200m² ~9.6M channels
SUPERCONDUCTING SOLENOID
Niobium titanium coil carrying ~18,000A
MUON CHAMBERS
Barrel: 250 Drift Tube, 480 Resistive Plate Chambers
Endcaps: 468 Cathode Strip, 432 Resistive Plate Chambers
PRESHOWER
Silicon strips ~16m² ~137,000 channels
FORWARD CALORIMETER
Steel + Quartz fibres ~2,000 Channels
CRYSTAL ELECTROMAGNETIC CALORIMETER (ECAL)
~76,000 scintillating PbWO₄ crystals
HADRON CALORIMETER (HCAL)
Brass + Plastic scintillator ~7,000 channels

Figure 3.2: A sliced view of the CMS detector.

3.2.1 The Tracker

The tracker is the innermost layer of the CMS detector and is completely made of silicon. It consists of two separate subdetectors: the inner pixel detector and the outer strip detector. The purpose of the tracker is to collect precise, three-dimensional single hit positions along the curved trajectories of charged particles to extract their momentum. The tracker covers up to a pseudorapidity of $\mid \eta \mid < 2.5$. A schematic of the tracker can be seen in Figure 3.3 [37].

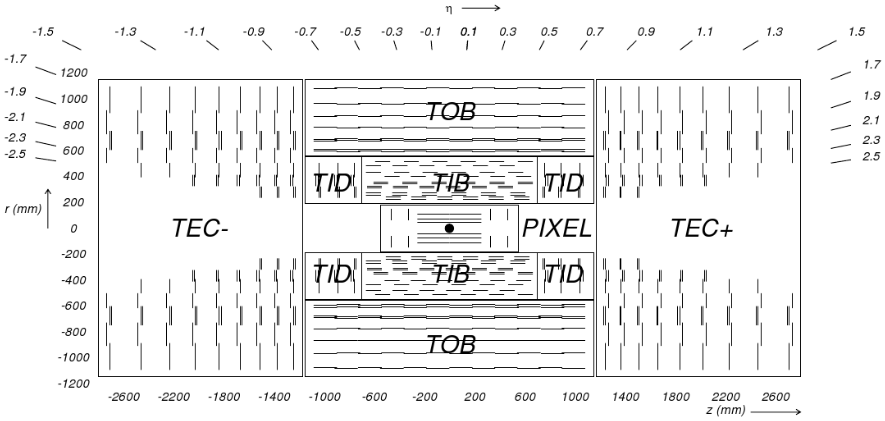
η
-1.5
-1.3
-1.1
-0.9
-0.7
-0.5
-0.3
-0.1
0.1
0.3
0.5
0.7
0.9
1.1
1.3
1.5
-1.7
-1.9
-2.1
-2.3
-2.5
1.7
1.9
2.1
2.3
2.5
r (mm)
1200
1000
800
600
400
200
0
-200
-400
-600
-800
-1000
-1200
TEC-
TOB
TID
TIB
TID
PIXEL
TID
TIB
TID
TOB
TEC+
-2600
-2200
-1800
-1400
-1000
-600
-200
200
600
1000
1400
1800
2200
2600
z (mm)

Figure 3.3: A schematic of the CMS tracker in the r-z plane.

3.2.1.1 The Pixel Detector

The pixel detector contains 65 million pixels that are $100 \times 150\,\mu\text{m}^2$ with a thickness of $285\,\mu$m. These pixels are contained in two different sections: the barrel (BPIX) and the endcaps (FPIX). The barrel is a cylindrical structure that surrounds the interaction vertex and consists of three concentric layers. These layers are at distances of 4.4, 7.3, and 10.2 cm from the beamlines. The endcap section consists of 2 symmetrical disk sections on either end of the barrel. Each section is made up of 2 disks that are 34.5 and 46.5 cm from the interaction point. An important feature of the pixel detector is its precise hit resolution, which is necessary for the high performance of different reconstruction and tagging algorithms. The resolution is measured by comparing the hit position in the second layer of the barrel with an interpolated track created from hits in the inner and outer layer and taking the residual difference. The resolution is 10.6 μm in the $r-\phi$ direction and 29.1 μm in the z direction as shown in Figure 3.4[38].

At the end of the 2016 data taking period, an additional layer was added to the barrel region and the layers are now at distances of 3.0, 6.8, 10.2, and 16.0 cm. An additional disk was also added to each endcap region and each disk now consists of 2 concentric rings, inner and outer, to enable easy replacement. A comparison of the 2016 and 2017 pixel detector geometries can be seen in Figure 3.5[39].

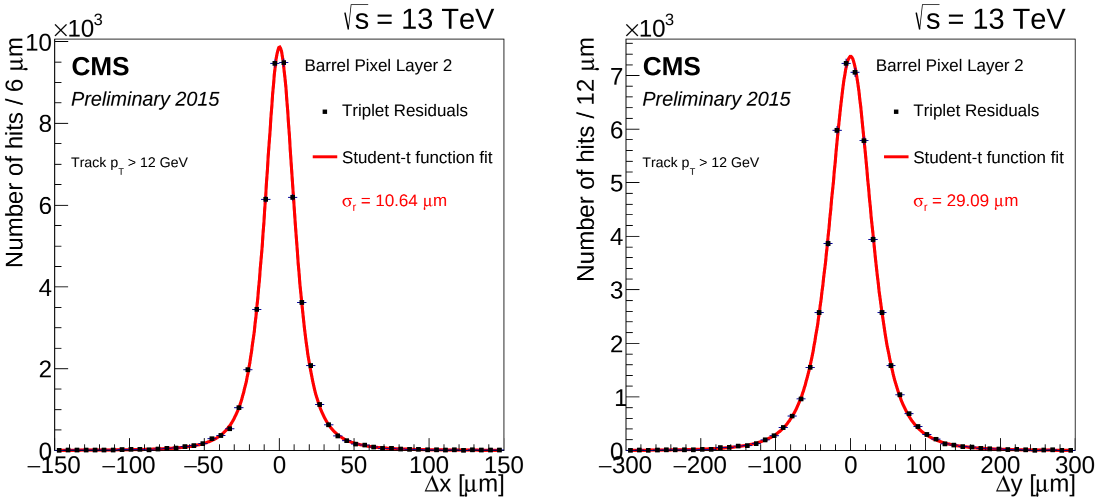

Figure 3.4: Distribution of hit residuals on the second pixel barrel layer in the transverse (left) and longitudinal (right) directions to the beam. The distribution is fitted with a student's t-function for which sigma is shown on the plot.

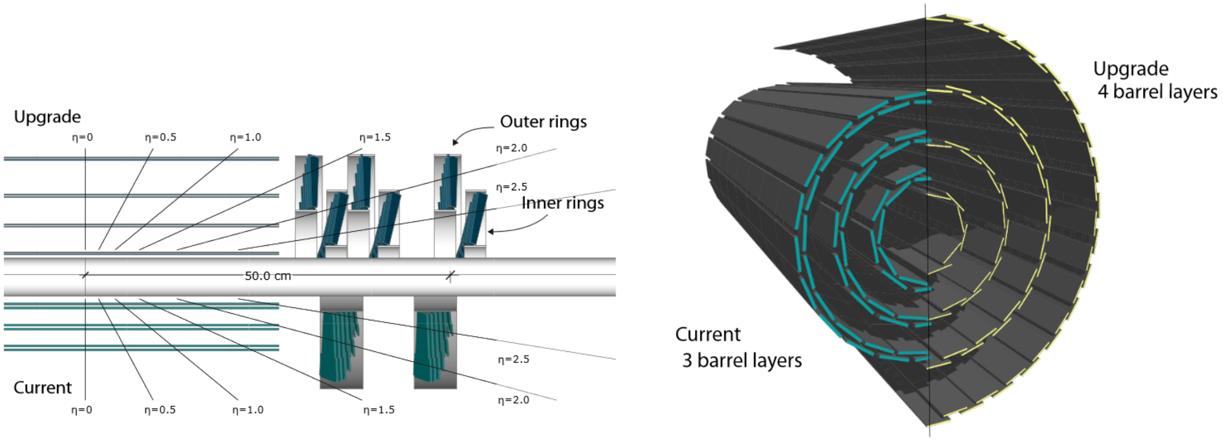
Upgrade
η=0
η=0.5
η=1.0
η=1.5
Outer rings
η=2.0
η=2.5
Inner rings
50.0 cm
η=2.5
η=2.0
Current
η=0
η=0.5
η=1.0
η=1.5
Upgrade
4 barrel layers
Current
3 barrel layers

Figure 3.5: A comparison of the 2016 pixel detector geometry with the 2017 upgrade geometry.

The silicon pixels are grouped in modules of 52 × 80 pixels and bump-bonded to a read-out-chip (ROC). These ROCs amplify and shape the signals from the pixel sensors so that they can be converted from analog to digital signals.

Due to the proximity of the pixel detector to the interaction point, the sensors and readout electronics will receive an incredibly high particle flux. The innermost layer of the BPIX is expected to receive a radiation dose of 840 kGy after an integrated luminosity of 500 fb^{-1}. A radiation tolerant design was a top priority for both the electronics and sensors and more details on this will be given in Chapter 5.

3.2.1.2 The Strip Detector

Outside of the pixel detector is the strip detector which is arranged in a similar manner as the pixel detector. There is a barrel region that is split into an inner barrel (TIB) section and an outer barrel (TOB) section and two endcap sections on either side that consist of an inner endcap region (TID) and an outer endcap region (TEC). The TIB consists of four concentric cylinders that extend out to 65 cm on either side of the interaction point and have radii between 25.5 and 49.8 cm. The two inner layers are comprised of double sided modules with a strip pitch of 80 μm and the two outer layers are made of single sided modules with a strip pitch of 120 μm. The TOB consists of 6 concentric cylinders that extend from -110 to $+110$ along the z axis and are between radii of 55.5 to 116.0 cm. Each TID consists of 3 disks located between $z = \pm 80$ cm and $z = \pm 90$ cm. A disk consists of 3 rings which span radii from 20 to 50 cm. The 2 innnermost rings have double sided modules and the outermost has single sided ones. The TEC disks extend radially from 22 to 113.5 cm and are located between ± 124 cm and ± 280 cm along the z direction. The silicon sensors in the TIB, TID, and inner 4 rings of the TEC are 320 μm thick and the sensors in the TOB and 3 outer rings of the TEC are 500 μm thick[37].

3.2.2 The Electromagnetic Calorimeter

Surrounding the tracker is the electromagnetic calorimeter (ECAL) which measures the energies of electrons and photons. The ECAL is made up of lead tungstate (PbWO4) crystals which produce scintillation light in fast, well defined photon showers whenever an electron or photon passes through them. These showers can be measured by photodetectors to determine the energy of the electron or photon. Since the yield of light in the crystals depends on temperature, the temperature of the ECAL does not vary by more than 0.1°C.

The ECAL is made up of a barrel region which consists of 61,200 crystals and two endcap segments which consist of 7,324 crystals. The barrel covers a pseudorapidity of $|\eta| < 1.479$ and is made of crystals with a cross section of 22×22 mm^2 and a length of 230 mm, which corresponds to 25.8 radiation lengths. The photodetectors in the barrel region are avalanche photodiodes and are made of silicon. The endcaps cover a pseudorapidity of $1.48 < |\eta| < 3.0$ and the crystals have dimensions $24.7 \times 24.7 \times 220$ mm^3. The crystals are organized into groups of 36 crystals, called a supercrystal, and each endcap contains 268 supercrystals. The photodiodes in the endcaps are vacuum phototriodes and are used because of the higher radiation tolerance that is needed in this region.

Another component of the ECAL is the preshower detector. The preshower sits in front of both endcaps and covers a pseudorapidity of $1.65 < |\eta| < 2.61$. The purpose of the preshower is for extra spatial precision in order to distinguish single photons from a π^0 decaying to two nearby photons. The preshower is made of 2 planes of lead followed by silicon sensors that have dimensions of 6.3 cm × 6.3 cm × 0.3 mm[37][40]. The layout of the ECAL can be seen in Figure 3.6.

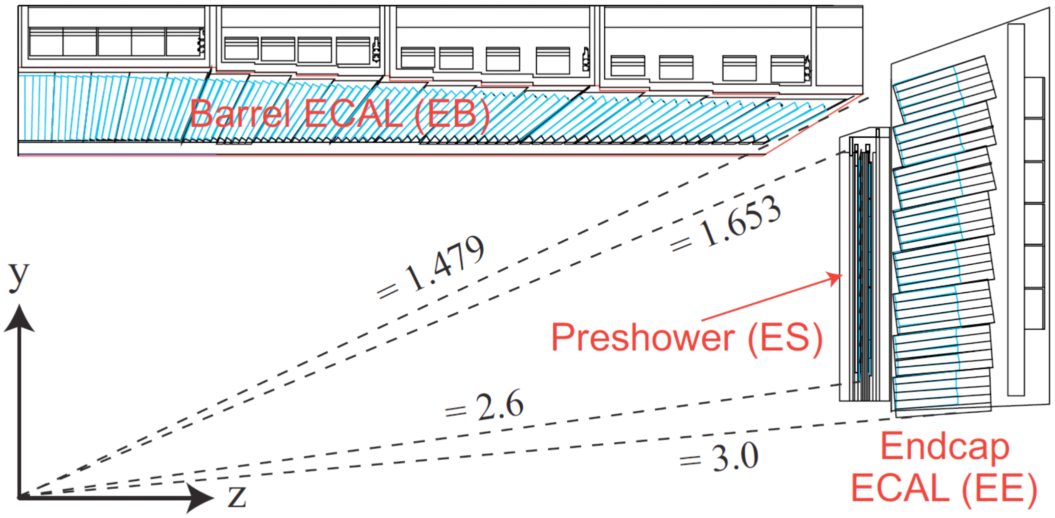

Figure 3.6: Schematic view of a quadrant of the electromagnetic calorimeter (ECAL). The numbers correspond to η and show the coverage of the different sections of the ECAL.

3.2.3 The Hadron Calorimeter

The HCAL surrounds the ECAL and its purpose is to measure the energy of hadrons. It is designed to be a hermetic detector because all particles from an interaction must be detected to accurately measure the missing transverse energy (MET) of an event. The HCAL is a sampling detector that is made up of alternating layers of absorber and scintillator. The absorbers are made of either brass or steel and when a particle hits them a shower of particles is produced. Light is then emitted when particles pass through the scintillation material and absorbed by wavelength-shifting fibers that are less than 1 mm in diameter. The HCAL is divided into 4 sections: the barrel (HB), the endcap (HE), the outer calorimeter (HO), and the forward calorimeter (HF). A schematic of the HCAL can be viewed in Figure 3.7[37].

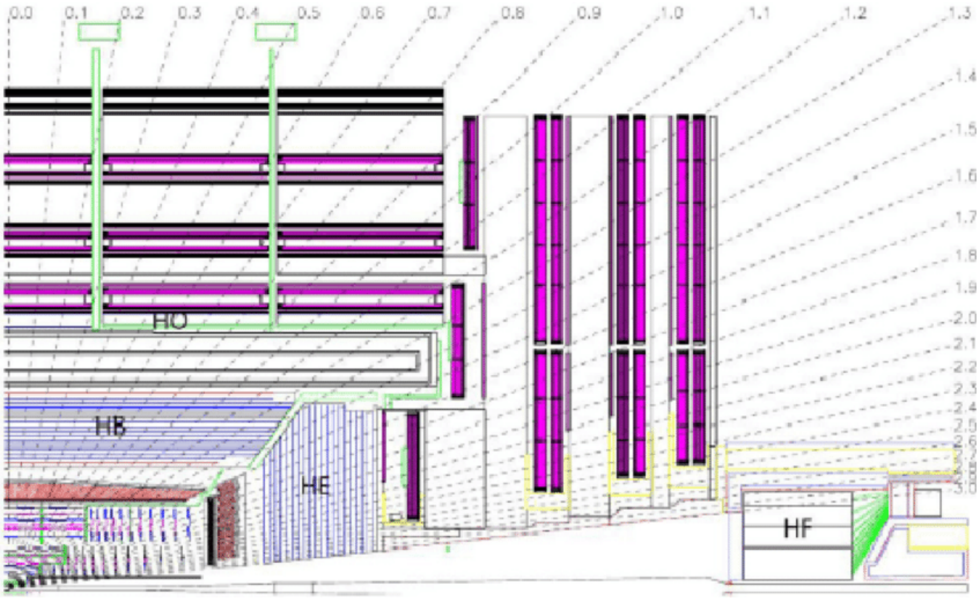

Figure 3.7: Schematic cross section of the hadron calorimeter (HCAL).

The HB sits inside the magnet and covers a pseudorapidity of $|\eta| < 1.3$. It is made up of 36 wedges aligned parallel to the beam axis, where each wedge consists of brass plates interspersed by plastic scintillator. The plastic scintillator plates are divided into 16 sections giving a granularity of $\Delta\eta \times \Delta\phi = 0.087 \times 0.087$. For structural support, the outermost layers of each wedge are steel plates.

The HE is designed to sustain a high radiation flux due to the pseudorapidity region it covers, $1.3 < |\eta| < 3$. It also must provide the maximum number of interaction lengths to contain hadronic showers. Thus, C26000 brass was chosen as the absorber and the combined material in the HE provides about ten interaction lengths. For $|\eta| < 1.6$ the granularity is $\Delta\eta \times \Delta\phi = 0.087^2$ while for $|\eta| >= 1.6$ the granularity is $\Delta\eta \times \Delta\phi = 0.17^2$.

Due to the limited space within the solenoid magnet, the HO sits outside of the magnet and detects any late starting showers. The HO covers $|\eta| < 1.3$ and adds more material to the barrel region to provide 11.8 radiation lengths. Since the HO detects energy that would otherwise be missed, it improves missing transverse energy (MET) measurements.

The HF sits 11.2 m from the interaction point down the beam line. It is a cylindrical structure with an outer radius of 130 cm. Due to the extreme, 760 GeV energy per proton-proton interaction deposited into the forward calorimeters, quartz fibers are used as the active medium. It has a granularity of $\Delta\eta \times \Delta\phi = 0.175 \times 0.175$ and covers a pseudorapidity range of $3.0 < |\eta| < 5.0$.

3.2.4 The Superconducting Magnet

As implied by the name of CMS, the superconducting magnet is a central design feature of the detector. By producing a uniform, 3.8 T magnetic field the paths of charged particles are bent and the momentum of these particles can be accurately measured. The magnet is a solenoid with a length of 12.5 m and a 6.3 m inside diameter. The magnet is made up of 4-layers of NbTi wires that are coiled and then cooled to $-268.5°$C to allow current to flow through with minimal resistance and produce the largest magnetic field possible. The magnetic flux is returned through a yoke that weighs 10,000 tons and is made up of six endcap disks and five barrel wheels.

3.2.5 The Muon System

The muon system is the outermost sub-detector of CMS since muons have a small cross section and can pass through several meters of iron without interacting. There are 1400 muon chambers that compose the muon system and these chambers consist of three different types of detectors: drift tubes (DTs), cathode strip chambers (CSCs), and resistive plate chambers (RPCs). The muon system sits between the magnet return yolk and covers a pseudorapidity of $|\eta| < 2.4$. The DTs and RPCs make up the barrel region of the sub-detector and the CSCs and RPCs make up the endcap regions. A detailed view of the muon system can be seen in Figure 3.8[37].

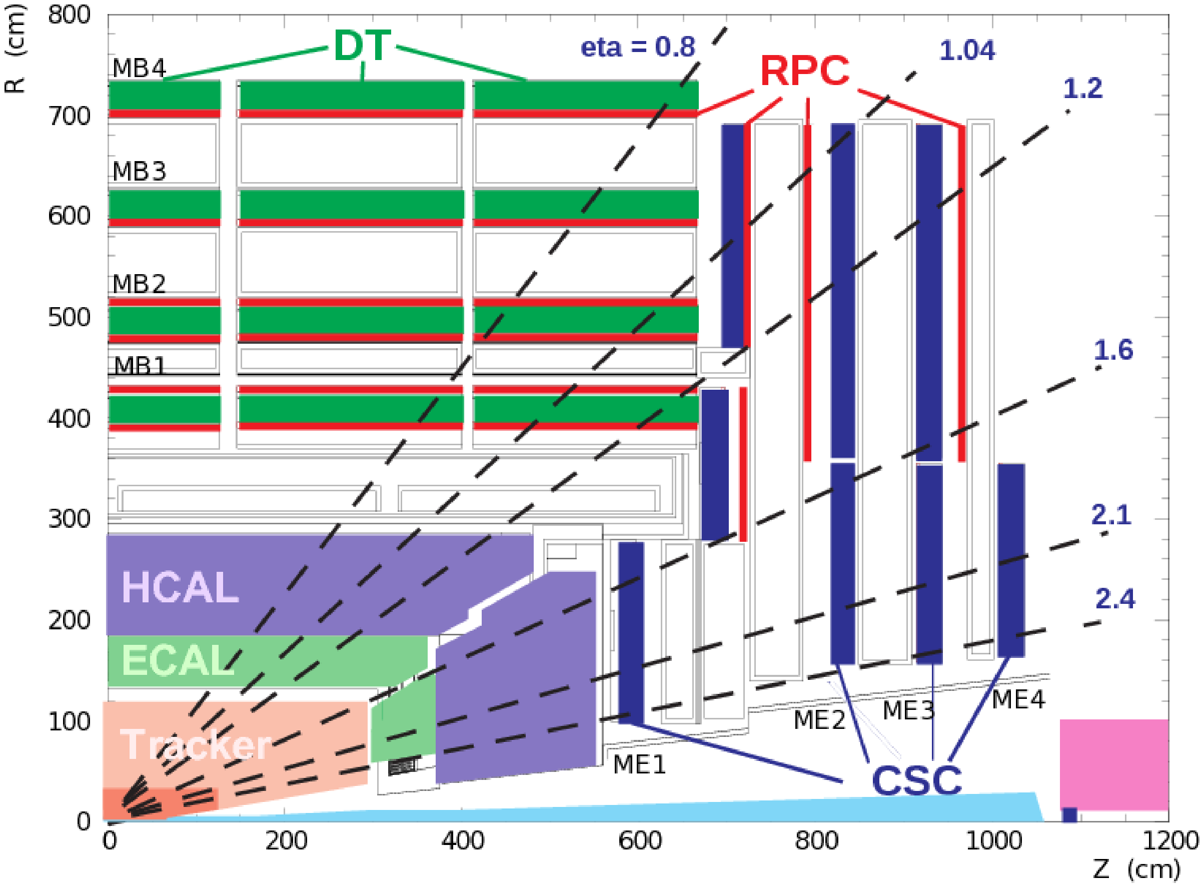
R (cm)
800
700
600
500
400
300
200
100
0
0
200
400
600
800
1000
1200
Z (cm)
DT
MB4
MB3
MB2
MB1
eta = 0.8
RPC
1.04
1.2
1.6
2.1
2.4
HCAL
ECAL
Tracker
ME1
ME2
ME3
ME4
CSC

Figure 3.8: Schematic view of the muon system.

The DTs are 4 cm wide tubes that contain a wire within a gas volume comprised of 85% Ar and 15% CO_2. The muons ionize electrons off the atoms of the gas and the liberated electrons collect on the wire where a positive voltage is applied. The drift velocity of electrons in the gaseous mixture is known and thus two position coordinates can be measured. The DTs are arranged in 4 concentric cylinders around the beamline and cover a pseudorapidity of $|\eta| < 1.2$.

CSCs are made of arrays of positively charged anode wires crossed with negatively charged cathode strips within a gas volume. Electrons from the traversing muons are detected in a similar way as the DTs and since the wires and strips are perpendicular to each other 2 position coordinates are measured. The CSCs cover the pseudorapidity range $0.9 < |\eta| < 2.4$ and are arranged in 5 separate layers that are made up of different numbers of rings.

RPCs are made of 2 oppositely charged parallel plates that are made of a high resistivity plastic material and separated by a gaseous volume. The plates are transparent to electrons which are detected by external metallic strips. The RPCs have a coarser resolution than the DTs and CSCs, but have a timing resolution on the order of nanoseconds. They cover $|\eta| < 1.6$ and are primarily used as a secondary muon identification tool to confirm the measurements in the DTs and CSCs.

3.2.6 The Trigger System

Collisions at CMS occur every 25 ns or at a rate of 40 MHz, which produces an impossible amount of data to store. To make the data storage manageable, CMS employs a trigger system that attempts to only save interesting events. To do this, the trigger system is made up of 2 triggers: the Level-1 (L1) trigger and the high level trigger (HLT). The L1 trigger consists of programmable electronics and reduces the rate of events accepted for possible storage to 100 kHz. The HLT uses software to reconstruct physics objects and reduces the rate to below 1 kHz.

3.2.6.1 The Level-1 Trigger

The L1 trigger uses information from every sub-detector, except for the tracker, to determine whether an event is passed to the HLT. It has a 3.2 μs latency period to make this decision and the tracker cannot provide information from its measurements in this small time frame. The final step of the L1 trigger that decides whether an event is kept or rejected is the Global Trigger and it uses information from the calorimeter trigger and muon trigger to make this decision.

The initial step of the calorimeter trigger are the Trigger Primitive Generators (TPG), which sum the transverse energies measured in ECAL crystals or HCAL read-out towers. This information is used to determine possible electrons or photons, transverse energy sums, and tau-veto bits by the Regional Calorimeter Trigger. The Global Calorimeter Trigger then determines the highest-rank calorimeter trigger objects across the entire detector. It determines jets, total transverse energy, MET, jet counts, HT, and the highest-rank isolated and non-isolated electron and photon candidates.

The muon trigger uses track segments combined from the DTs and CSCs, as well as separate track candidates from the RPCs. The Global Muon Trigger combines this information to achieve the best momentum resolution and efficiency possible and determine the four best muon candidates. The architecture of the L1 trigger system can be seen in Figure 3.9.

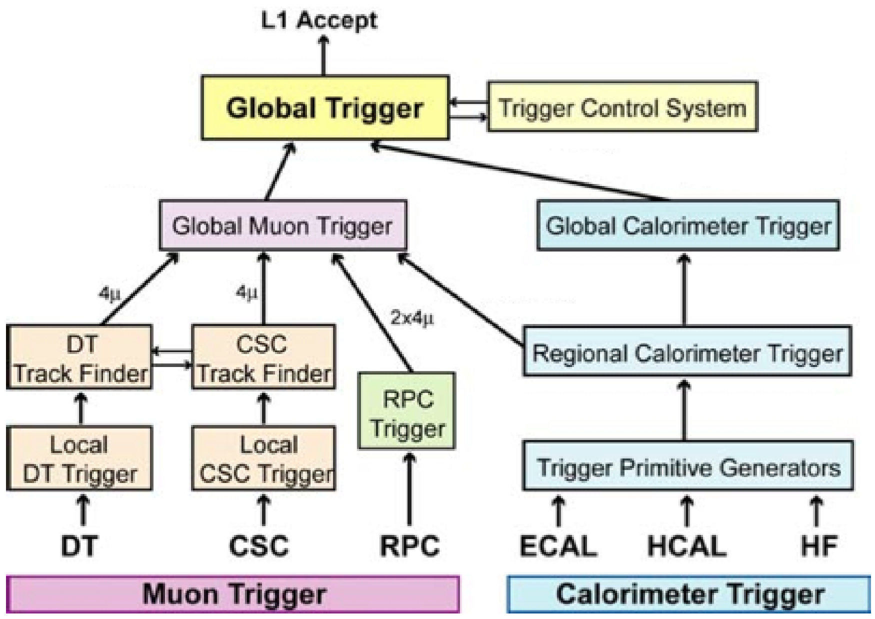
L1 Accept
Global Trigger
Trigger Control System
Global Muon Trigger
Global Calorimeter Trigger
4μ
4μ
2x4μ
DT Track Finder
CSC Track Finder
RPC Trigger
Regional Calorimeter Trigger
Local DT Trigger
Local CSC Trigger
Trigger Primitive Generators
DT
CSC
RPC
ECAL
HCAL
HF
Muon Trigger
Calorimeter Trigger

Figure 3.9: Schematic of the Level-1 trigger system.

3.2.6.2 The High Level Trigger

The HLT is a software based system that uses reconstructed physics objects to make complicated calculations. These calculations are done using similar software to what is used in offline analyses. The HLT is made up of many different HLT paths that are implemented for specific analyses and each consist of a sequence of steps of reconstructing and filtering in increasing complexity. The HLT paths used by the analysis presented in this thesis will be described in Section 6.3.

Chapter 4

Object Reconstruction

The CMS detector attempts to identify all particles produced in *pp* collisions. However, all of the data from an event is provided as hit patterns in the subdetectors and to simplify the analysis of these hit patterns they are first converted into physics objects. This chapter will describe the process of reconstructing physics objects from the information provided by the CMS detector.

4.1 The Particle Flow Algorithm

The Particle Flow (PF) algorithm [41, 42] optimally combines information from all of the subdetectors to identify and reconstruct every individual particle produced in a proton-proton (pp) collision. To accomplish this, the CMS detector was designed with a nearly fully efficient tracking system to precisely reconstruct tracks and vertices and a calorimeter with excellent granularity to disentangle overlapping showers. The PF algorithm is comprised of three main elements: iterative tracking, calorimeter clustering, and the link algorithm.

4.1.1 Iterative Tracking

To reconstruct the charged particles from a *pp* collision, the hits in the tracker need to be converted into a collection of tracks. The tracking software used by the PF algorithm is called the Combinatorial Track Finder (CFT) [43] and it allows pattern recognition and track fitting to occur in the same framework. The CFT is run six times with the reconstruction criteria loosening for each iteration to achieve both a high efficiency and low fake rate. Each iteration is comprised of four steps: seed generation, track finding, track fitting, and track selection.

Seed generation determines initial track trajectories from the minimum number of hits necessary to define a trajectory in a magnetic field. Five parameters are needed to define a helical trajectory and therefore, either 3 hits or 2 hits and an additional constraint that the particle originates from the beam spot are used to define the seeds. These seeds are required to pass some minimum p_T threshold and must be consistent with originating from the pp interaction region. Next, the initial track trajectories are extrapolated out and at each detector layer the hit with the position that produces the smallest χ^2 to the extrapolated trajectory is added to the track. This process is repeated at each detector layer until the end of the tracker is reached. When there is no hit along the trajectory at a certain layer, a "ghost" hit is added to the track. Tracks are discarded after a certain number of ghost hits are recorded. To obtain the full information of the trajectory, tracks are refitted with all hits using a Kalman filter and smoother [44]. Finally, tracks are selected if they pass a certain number of quality requirements such as the number of layers with hits, the χ^2/ndf of the track fit, and the compatibility that the track originates from the primary vertex. This greatly reduces the number of fake tracks.

4.1.2 Calorimeter Clustering

There are four purposes to the clustering algorithm in the calorimeter: detect and measure the energy and direction of neutral particles, separate these neutral particles from energy deposits of charged ones, reconstruct and identify electrons and all accompanying Bremsstrahlung photons, and assist the energy measurement of charged hadrons when track parameters are not accurately determined. The clustering algorithm is therefore designed for a high detection efficiency for low-energy particles and a separation of close energy deposits from the high granularity calorimeter. Clustering is performed separately in each subdetector as follows.

First, the seed for a cluster of nearby hits is identified as the hit with the maximum energy that is above a given threshold. Topological clusters are then created by adding cells that are adjacent to the cells already in the cluster and have an energy above a given threshold. Finally, the final energy and position of the clusters is determined through an iterative expectation-maximization algorithm.

4.1.3 The Link Algorithm

The purpose of the link algorithm is to connect the different PF elements from the subdetectors to fully reconstruct a particle. The elements that can be linked are charged-particle tracks, calorimeter clusters, and muon tracks. The link algorithm creates blocks of elements which contain two or three elements.

A link between a track and a calorimeter cluster is made if the extrapolated track from the tracker lands within the cluster. Clusters from different calorimeter subdetectors are linked when the position in the more granular calorimeter is within the cluster envelope in the less granular calorimeter. And finally, links between tracker tracks and muon tracks are made when a global fit of the combied tracks returns an acceptable χ^2.

4.1.4 Particle Identification

Each block of elements is identified as specific particles in the following way. First, muons are identified when the momentum of the combined tracks in the tracker and muon detector is within 3σ of the tracker momentum. The corresponding tracks are then removed from the block. Secondly, electrons are identified by finding tracks that fit the criteria of an electron track: short tracks that lose energy from Bremsstrahlung. These tracks are refit with a Gaussian-Sum fitter [45] to project their trajectories out to the ECAL and find an intersecting cluster. The corresponding track and ECAL cluster are then removed from the block. Thirdly, charged hadrons are identified from the remaining tracks and are associated to clusters in the HCAL if the cluster energy falls within the uncertainties of the track momentum. Finally, the remaining clusters in the HCAL and ECAL are associated with neutral hadrons and photons, respectively.

4.2 Vertex Reconstruction

Vertex reconstruction locates all of the *pp* interactions within an event so that they can be classified. The *primary* vertex results in high p_T particles and is of most interest because the primary signature of the event originates from it. The remaining vertices are referred to as *pileup* and most of these interactions produce soft particles that contribute to the overall hadronic activity within an event, and can obscure the interesting processes. In 2016, the CMS detector recorded between 45 to 60 pileup vertices for each event and therefore determining the activity from pileup is crucial for analyses.

Vertex reconstruction consists of three steps: track selection, clustering tracks originating from the same vertex, and fitting the tracks for the position of each vertex. Track are selected that are produced promptly in the primary interaction region. This is done by placing requirements on the impact parameter of the track relative to the center of the beam, the number of hits within the track, and the χ^2 of the fit trajectory. The tracks are then clustered according to their z-coordinate at their point of closest approach to the center of the beam spot. Finally, the position of each vertex is determined by fitting each cluster of tracks [43].

4.3 Jet Reconstruction

In an attempt to reconstruct the hadronization of a quark or gluon, the hadrons and non-isolated leptons of an event are clustered together to form jets. In this analysis, the "anti-k_t" algorithm is used to create jets. This algorithm iteratively clusters particles together by defining two distance parameters

$$d_{ij} = min(k_{ti}^{2p}, k_{tj}^{2p})\frac{\Delta_{ij}^2}{R^2}, \tag{4.1}$$

$$d_{iB} = k_{ti}^{2p}, \tag{4.2}$$

where k_{ti} is the transverse momentum of particle i, $\Delta_{ij}^2 = (\eta_i - \eta_j)^2 + (\phi_i - \phi_j)^2$, η_i is the rapidity, ϕ_i is the azimuth, R is the chosen cone radius, and $p = -1$ gives the anti-k_t algorithm. The distance between particles i and j, d_{ij}, is compared to d_{iB}, the distance between particle i and the beam. If d_{ij} is smaller than d_{iB} then i and j are recombined, but if d_{ij} is larger then i is called a jet and removed from the remaining particles. This continues until are particles have been clustered into jets.

The anti-k_t algorithm clusters soft particles to hard ones, so that a jet's axis is mainly defined by its hard constituents. This is a key feature of the algorithm because the jet's axis will not dramatically change when soft radiation from pileup is removed from the event. When two hard particles are nearby, they are either clustered together or the soft particles are shared between them based on the size of the cones being reconstructed.

4.4 Missing Transverse Energy

The initial momentum of the colliding constituents in the protons at CMS is unknown, however it is known that their transverse momentum is zero. Therefore, by conservation of momentum, the combined transverse momentum of all of the particles produced in the collision is zero. However, weakly interacting particles, such as neutrinos, can avoid detection and cause there to be an imbalance in the transverse momentum of a collision. These signatures are predicted by many theoretical models and therefore, a useful quantity in the analysis of CMS data is the missing transverse momentum

$$\vec{\not{E}}_T = - \sum_{detected\,particles} \vec{p_T}. \tag{4.3}$$

This quantity is referred to as MET throughout this paper.

4.5 b-tagging

The identification of jets arising from the hadronization of b quarks is crucial for searches for new physics and for measurements of standard model processes. These jets can be distinguished from jets initiated by gluons or light flavor quarks due to the long lifetime of B hadrons, about 1.5 ps, which causes the B hadron to decay within the jet and form a secondary vertex. These secondary vertices are displaced hundreds of micrometers away from the primary vertex and therefore, the high resolution of the pixel detector is the leading reason b quarks are identified efficiently.

CMS employs several b tagging algorithms [6], although the combined secondary vertex (CSVv2) algorithm is primarily used. The CSV algorithm uses secondary vertices, which are reconstructed from the tracks of charged particles within a jet, and track impact parameters, which are the points of closest approach from each track to the primary vertex, as input to a likelihood based discriminant. The shape of the CSVv2 discriminant is shown in Figure 4.1.

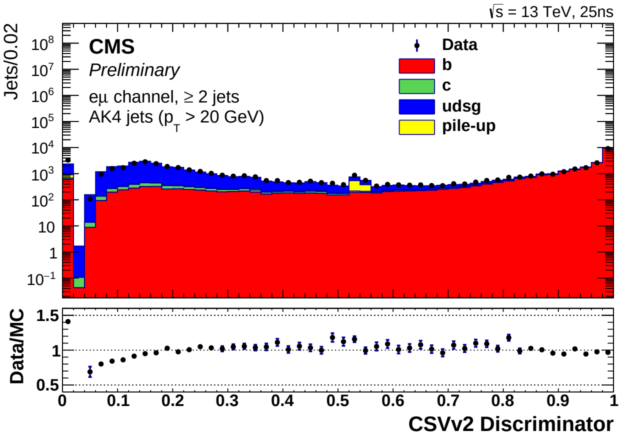

Figure 4.1: Discriminator values for the combined secondary vertex (CSVv2) algorithm in a dilepton $t\bar{t}$ topology. The total number of entries in the simulation is normalized to the observed number of entries in data. The small bump between discriminator values of 0.5 and 0.6 are due to tracks or jets from pileup collisions [6].

4.6 Double b-tagging

A more challenging tagging technique is the identification of jets that contain two b quarks. This is especially important for the analysis presented in this thesis, where a Higgs decaying to $\mathrm{b\bar{b}}$ is reconstructed within a single large cone jet, also referred to as a *fatjet*. In Run I of the LHC, two different techniques were used to identify jets containing two b quarks: fatjet b tagging and subjet b

tagging. Fatjet b tagging applies the standard b tagging algorithm to a fatjet but with the track and vertex criteria relaxed due to the larger jet cone size. Subjet b tagging defines two subjets within the fatjet and then individually b tags each of these. These two approaches complimented each other to an extent. Fatjet b tagging performs better in the high tagging efficiency regime where the presence of displaced tracks improves the performance, while subjet b tagging performs better in the high purity regime where it can rely on the reconstruction of two distinct secondary vertices. For jets with higher p_T, the subjets begin to overlap and subjet b tagging becomes inefficient due to the double counting of tracks. A diagram of these two approaches can be seen in Figure 4.2 and due to the complentary nature of these techniques it is clear that there is a possibility for improvement with a more efficient tagger.

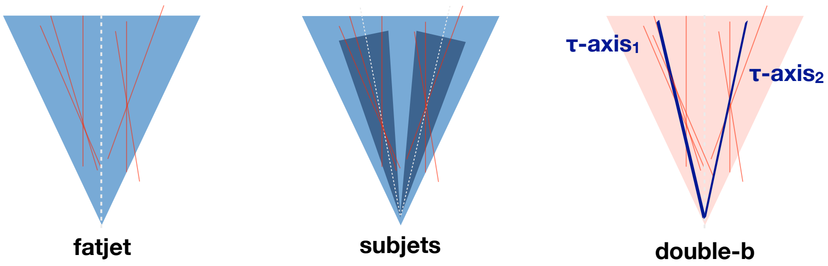

Figure 4.2: Schematic comparison of the fatjet and subjet b tagging approaches and the double-b tagger [7].

Therefore, a dedicated multivariate algorithm, called the "double-b tagger," was developed to holistically tag jets containing two b quarks. The double-b tagger reconstructs secondary vertices within the fatjet independently of the jet clustering and then associates each secondary vertex to a subjet axis in order to reconstruct the decay chains of the two B hadrons. At the same signal efficiency, the mistag rate of the double-b tagger is lower by about a factor of 2 compared to the previous tagging approaches, as shown in Figure 4.3.

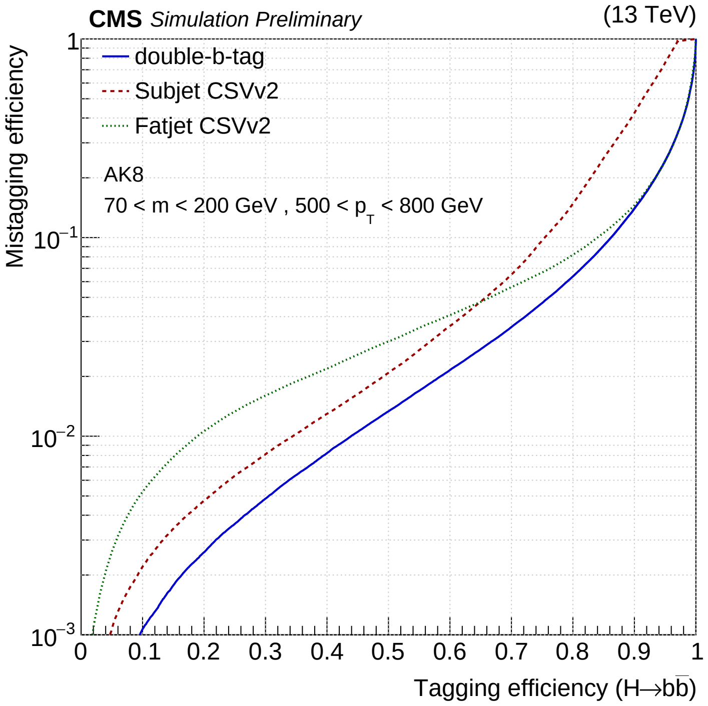

Figure 4.3: Comparison of the performance of the double-b tagger, the CSVv2 subjet b tagging, and fatjet b tagging using the CSVv2 algorithm for $500 < p_T < 800$ GeV jets. The tagging efficiency for signal is evaluated using boosted $\mathrm{H} \rightarrow \mathrm{b}\bar{\mathrm{b}}$ jets from simulation. The mistag rate is evaluated for simulated QCD jets containing zero, one or two b quarks[7].

Chapter 5

Radiation Tolerance of 65 nm CMOS Transistors

The need for extremely radiation tolerant electronics, especially in the era of High Luminosity running at the LHC (HL-LHC), is a major issue confronting high energy physics. The HL-LHC will begin running in 2025 and the expected peak luminosity is 5×10^{34} cm^{-2}s^{-1}. At this luminosity, the particle flux near the collision vertex will be extremely high and it will be vital for reconstruction and b-tagging algorithms that the electronics in the pixel detector operate while accumulating a total ionizing dose of about 1 Grad.

To lower the material density and power dissipation in the pixel detector, the plan for the HL-LHC readout chips in the pixel detector at CMS is to upgrade from the current 250 nm complementary metal-oxide-semiconductor (CMOS) technology to 65 nm CMOS technology. Previous studies [46] showed that the properties of 65 nm CMOS technology did not dramatically change after being exposed to a total dose of 200 Mrad. However, these studies were conducted at room temperature and the pixel detector will be operated at -20°C to limit the leakage current in the silicon strip trackers. At a lower temperature, the CMOS devices will not anneal as much and the radiation damage might be greater than had been observed in room temperature exposures. Therefore, this chapter summarizes an important study that characterizes the response of 65 nm CMOS technology to a cumulative radiation dose of 1 Grad while operating below -20°C.

5.1 Radiation Damage Mechanisms

Two types of radiation damage can occur when energetic particles pass through a semiconductor device and either electron-hole pairs ("ionization damage") are created or silicon atoms are displaced from their lattice sites ("displacement damage"). This section will focus on ionization damage because that is the damage mechanism that this study characterized.

Ionization damage occurs in the insulating layers of the device, usually SiO_2, when the electrons and holes drift to different locations where they are trapped and cause unwanted electromagnetic fields within the device. There are two locations of insulating layers within current semiconductors: the gate oxide and the shallow trench isolation (STI) oxide. A layout of a CMOS transistor can be seen in Figure 5.1[8].

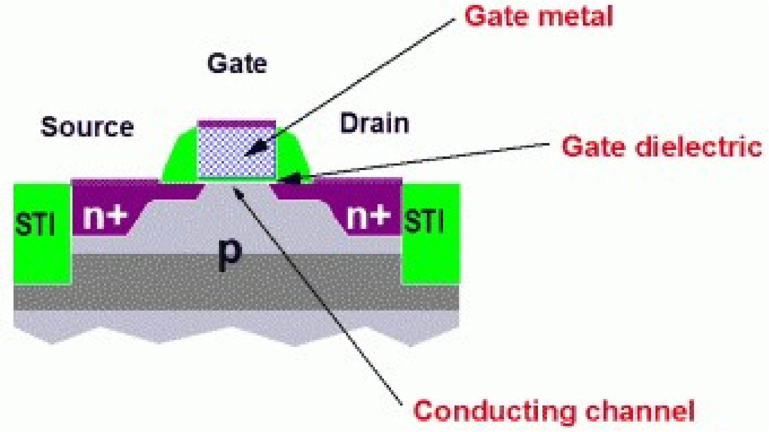

Figure 5.1: The cross section view of an n-channel transistor. The transistor is built on a p-type substrate with n-type implants as the source and drain. An inversion layer is formed in the conducting channel when a positive voltage is applied to the gate. The gate dielectric (gate oxide) and shallow trench isolation (STI) oxide are the green regions[8].

The gate oxide separates the gate terminal from the conductive channel that connects the source and drain and serves as a dielectric layer so that the gate can sustain a high electric field. When electron-hole pairs are created in the gate oxide the electrons are swept out of the oxide by the positive voltage applied on the gate terminal while holes move in the opposite direction toward the Si/SiO_2 interface. Two separate mechanisms can then occur [47]:

- **Deep Hole Trapping:** There is a transition region from SiO_2 to Si where the oxidation is not complete and there are oxygen vacancies. These vacancies cause weak Si-Si bonds, where each Si atom is also bonded to three oxygen atoms, that are broken by holes which then remain trapped there. The holes accumulate at the interface causing a buildup of positive charge.

- **Radiation-Induced Traps:** At the Si/SiO_2 interface there are tri-valent Si atoms that have been passivated by H atoms. Radiation-induced holes free protons from the oxide and the protons then travel to the Si/SiO_2 interface. At the interface the proton breaks the Si-H bond to form H_2 and a trivalent Si atom that is left with an unpassivated dangling bond that is an electrically active defect.

These effects cause the voltage seen by the conductive channel to differ from the actual voltage applied at the gate terminal and therefore, the transistor will turn on at a different voltage than it was designed to. These mechanisms are extremely dependent on the thickness of the gate oxide and more deep hole and radiation-induced traps will build up the thicker the gate oxide is.

STI oxide is implanted in the silicon between adjacent semiconductors to prevent leakage current. The same mechanisms that occur in the gate oxide also occur in the STI oxide, however they effect the transistor functionality differently. When charge builds up in the STI oxide, a conductive channel is opened between the source and drain of the transistor and leakage current can flow even when the transistor is turned off. This is illustrated in Figure 5.2[9].

The radiation induced charge that is trapped in the STI also prevents channel inversion near the STI and reduces the conductive channel width. This is referred to as Radiation Induced Narrow Channel Effect (RINCE)[48] and is more evident in narrow channel devices. A narrower conductive channel allows less current to flow from the source to drain and thus, the maximum drain to source current that can be achieved in a transistor is decreased.

Transistors can at least partially recover from these radiation induced damage mechanisms through a process called annealing. This is a complex process that occurs either when trapped

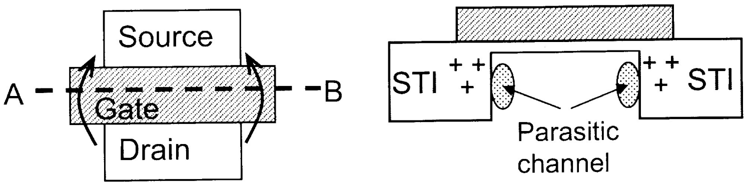

Figure 5.2: The crosses represent positive charge build up in the shallow trench isolation (STI) oxide, which allow current to pass between the source and the drain when no voltage is applied to the gate[9].

charge tunnels out of the oxide or is thermally excited enough to leave the oxide. Once a charge is free from the oxide, it is swept away by oppositely charged voltage contacts of the transistor. While this can improve the performance of individual transistors it is not a feasible solution for the entire pixel detector due to the complex interaction of numerous devices that react differently to annealing.

5.2 Experimental Details

5.2.1 Transistor Test Setup

A 65 nm CMOS Application Specific Integrated Circuit (ASIC) containing individual transistors connected to wire bond pads was built for radiation tolerance testing. Transistors within the ASIC were laid out in groups of similar transistors, for example all N-type metal-oxide-semiconductor (NMOS) transistors with the same channel length (L). Within a group, all transistors share a gate pad and a source/drain pad. The other drain/source of the transistor is connected to its own wire bonding pad, so that each transistor characteristic can be measured individually. The devices tested were P-type metal-oxide-semiconductor (PMOS) and NMOS core transistors operated at 1.2 V and NMOS input/output (I/O) transistors with double thickness gate oxide operated at 2.5 V. Several transistor sizes were included for core PMOS and NMOS transistors: transistors with L = 60 nm and a channel width (W) between 120 and 1000 nm, one transistor with size W/L = 500/500 nm, and one with size 5000/5000 nm. Additionally, triple deep well core NMOS transistors of size 120/60 nm and 5000/60 nm were included with a zero threshold voltage 1500/300 nm transistor and a zero threshold enclosed layout (ELT) 2240/300 nm transistor. The I/O NMOS transistor sizes were W = 280 nm and L between 400 and 1000 nm, a transistor with size 500/500 nm, and one with size 5000/5000 nm. The following different types of I/O NMOS transistors were also included: a triple deep well 800/280 nm transistor, an ELT 2220/280 nm transistor, a zero threshold 3380/1200 nm transistor, and a zero threshold ELT 3450/1200 nm transistor.

The test ASICs were wire bonded into pin grid array (PGA) chip carriers so that they could be irradiated on simple printed circuit boards (PCBs) containing only sockets for the ASICs and connectors for bias voltage. During irradiation PMOS transistors were biased in two different ways:

- The drains, sources, and gates were held at 1.2 V and the substrate was grounded.
- The gates and substrate were grounded while the drains and sources were held at 1.2 V.

The NMOS core (I/O) transistors were biased with the gates held at 1.2 V (2.5 V) and all other nodes grounded. These are the worst-case bias conditions.

Transistor characteristics were measured by mounting a single chip carrier at a time on a different PCB test board containing switches that allow individual transistors to be measured independently. The test board was connected to two source measurement units (SMUs), one to bias transistor gates and one to measure drain-source currents. Characteristics were made by holding the core (I/O) transistors drain-source voltage at 1.2 V (2.5 V) and the drain-source current was measured as the gate-source voltage was swept from 0 to 1.2 V (2.5 V).

5.2.2 Irradiation Setup

The irradiation of the test devices was performed at the Gamma Irradiation Facility (GIF) at Sandia National Laboratories. The GIF uses ^{60}Co sources to provide controlled doses of ionizing radiation. ^{60}Co decays by beta decay to an excited state of ^{60}Ni which then relaxes to the ground state by emitting two gamma rays of energy 1.17 and 1.33 MeV. The ^{60}Co is held in stainless steel “source pins” so that none of the beta electrons escape. Forty source pins are mounted in a straight-line array that is held at the bottom of an 18 foot deep pool of deionized water to provide shielding when not in use and raised out of the water when an irradiation takes place.

The test ASICs were held inside stainless steel thermos bottles positioned approximately two inches from the face of the array of pins. Cooling was provided by vortex tube coolers mounted in holes drilled through the plastic thermos bottle lids. Figure 5.3 shows the thermos bottle assembly. To maintain the temperature of the thermos bottles, which were heated by the gamma rays interacting with the walls of the thermos bottles, the compressed air that was input to the vortex tubes was precooled and passed through insulated copper tubes. The temperature within the thermos bottles was measured and recorded by a K-type thermocouple in each thermos bottle. Figure 5.4 shows the temperature of two thermos bottles during the irradiations.

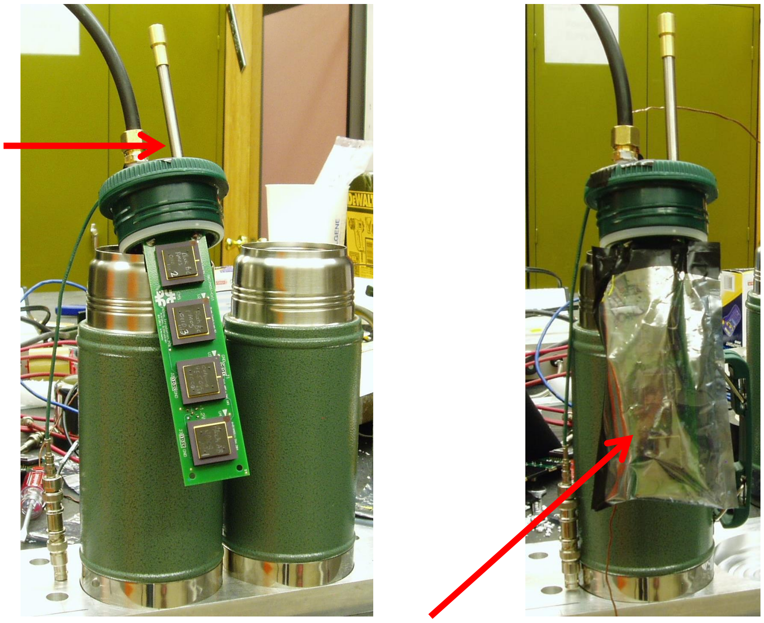

Figure 5.3: Pictures of the thermos bottle, including an irradiation printed circuit board with four chip carriers, before insertion of the irradiation board into the thermos bottle. On the left, the red arrow points to the vortex tube on top of the thermos bottle lid. On the right, the red arrow points to an antistatic bag which wraps the irradiation board and low-voltage cable before irradiation. These bags keep the boards and voltage cables dry during the irradiation.

The does rate the test ASICs received was 1425 rad/s and was measured by an ion chamber placed inside of a thermos bottle. The uniformity of the radiation field was checked by irradiating

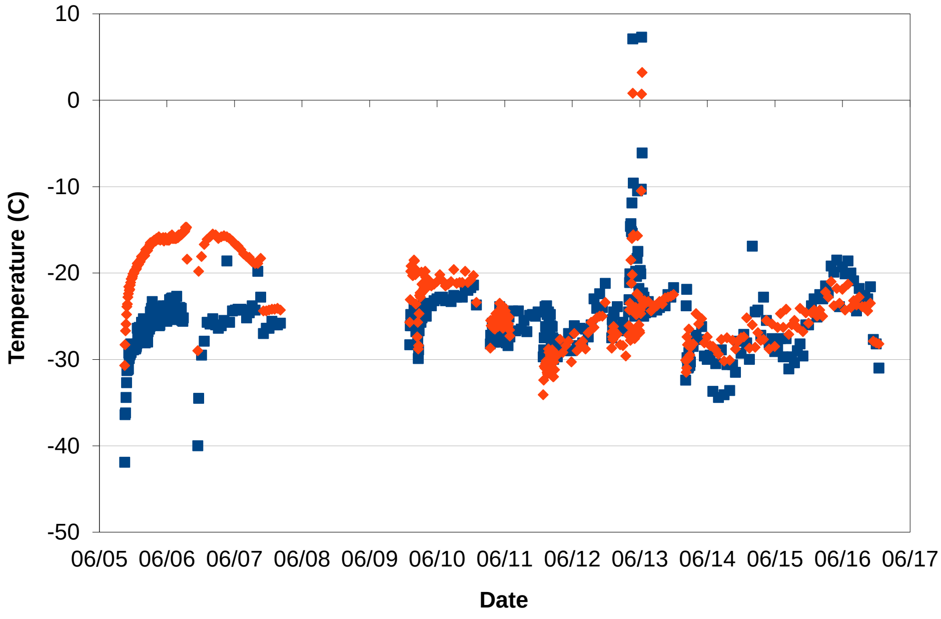

Figure 5.4: The temperature measured inside the two thermos bottles during the long irradiations. No irradiation was performed on June 8 or 9. The two spikes where the temperature reached about 8°C in both thermos bottles for 30 minutes on June 12 occurred because the compressed air unexpectedly turned off.

thermoluminescent dosimeters (TLDs) taped to each of the chip carriers on the irradiation PCB. The TLDs also provided a second measurement of the dose rate.

Twelve irradiations were performed over 15 days, as show in Table 5.1, and after each irradiation step a single characteristic curve was recorded for each transistor. All measurements were made at room temperature, but when a test ASIC wasn't being irradiated or measured they were stored at -20°C in a freezer. After the full irradiation, devices were kept at room temperature for a week and multiple characteristics were taken to characterize the annealing effects. The transistors were then held in an oven at 100°C for one week to simulate an extended annealing period and a final set of measurements was made.

Table 5.1: The irradiation schedule, showing the 2 weeks it took to accumulate 1 Grad.

Date	Length	Dose(Mrad)	Cumulative Dose(Mrad)
June 2	1 hour	5	5
June 3	1 hour	5	10
June 3	1 hour 45 mins	9	19
June 3	4 hour 15 mins	22	41
June 4-5	12 hours	62	103
June 5-6	22 hours	113	215
June 6-7	22 hours	113	329
June 9-10	22 hours	113	441
June 10-11	17 hours	87	528
June 11-12	22 hours	113	641
June 12-13	22 hours	113	754
June 13-16	66 hours	339	1093

5.3 Analysis

Two quantities were extracted from each transistor characteristic: the maximum drain-source current and the threshold voltage, V_{th}. The quadratic extrapolation method was used to determine the threshold voltage [49]. As shown in Figure 5.5, V_{th} is defined to be the voltage at which a line tangent to the curve $\sqrt{|I_{ds}|}$ vs V_{gs} at the point of maximum $\frac{d\sqrt{|I_{ds}|}}{dV_{gs}}$ intercepts the $I_{ds} = 0$ axis. The slope of the curve was determined by fitting it with a fifth order polynomial and differentiating the fit function.

5.4 Results

Figure 5.6 illustrates the radiation effects observed in the data. The most prominent effect is a decrease of the maximum drain-source current of core PMOS transistors. The fractional decrease is largest for the smallest PMOS transistors and they decreased by more than a factor of two. No significant difference was observed between the radiation-induced changes of PMOS transistors held at different bias voltages. This is illustrated in Figure 5.7. The maximum drain-source current of core NMOS transistors also decreased, but only by $\sim 5-10\%$. No significant threshold shift

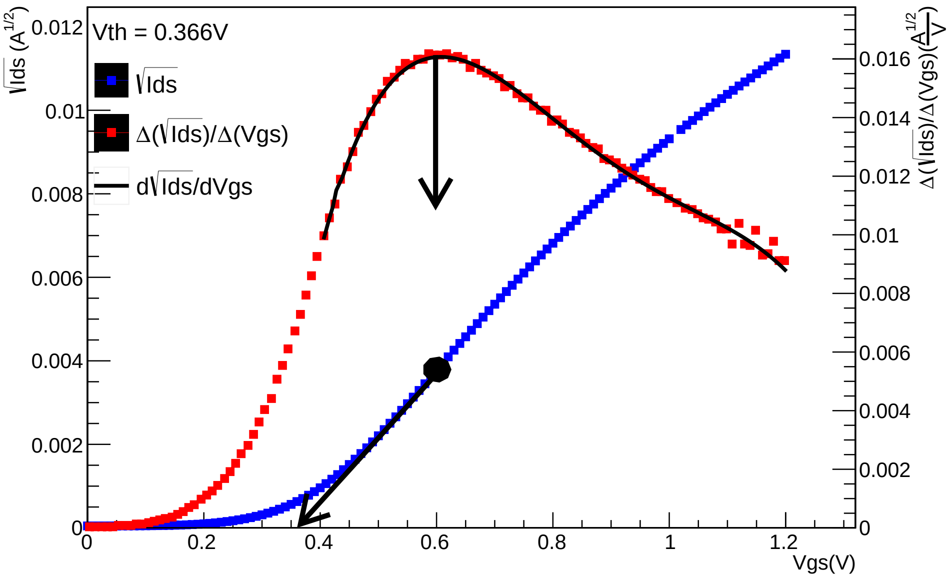

Figure 5.5: This figure illustrates the quadratic extrapolation method used to determine the threshold voltage (V_{th}) of an NMOS transistor. The blue data points are the transistor characteristic and the red ones are computed using finite differences $\frac{\sqrt{I_{ds}(N+1)}-\sqrt{I_{ds}(N)}}{V_{gs}(N+1)-V_{gs}(N)}$. The black curve is the result of differentiating the fifth order polynomial that was fit to the characteristic. V_{th} is the point on the $I_{ds} = 0$ axis where the tangent to the characteristic intersects. For PMOS transistors, $|I_{ds}|$ is used since I_{ds} is negative.

was observed for any of the core transistors, but the threshold voltage of NMOS I/O transistors increased by 100 - 200 mV.

Figure 5.8 demonstrates the annealing effects observed in our data. Both the PMOS core transistors and the NMOS I/O transistors recovered significantly during the annealing period.

Figures 5.9 and 5.10 show the evolution of the maximum drain-source current for a representative selection of PMOS and NMOS core transistors during irradiation and annealing. There were no significant differences in the effect of radiation on the various types of NMOS transistors tested (normal layout, enclosed layout, triple well, and zero V_{th}). Figure 5.11 shows the threshold shift of a representative selection of NMOS I/O transistors during irradiation and annealing.

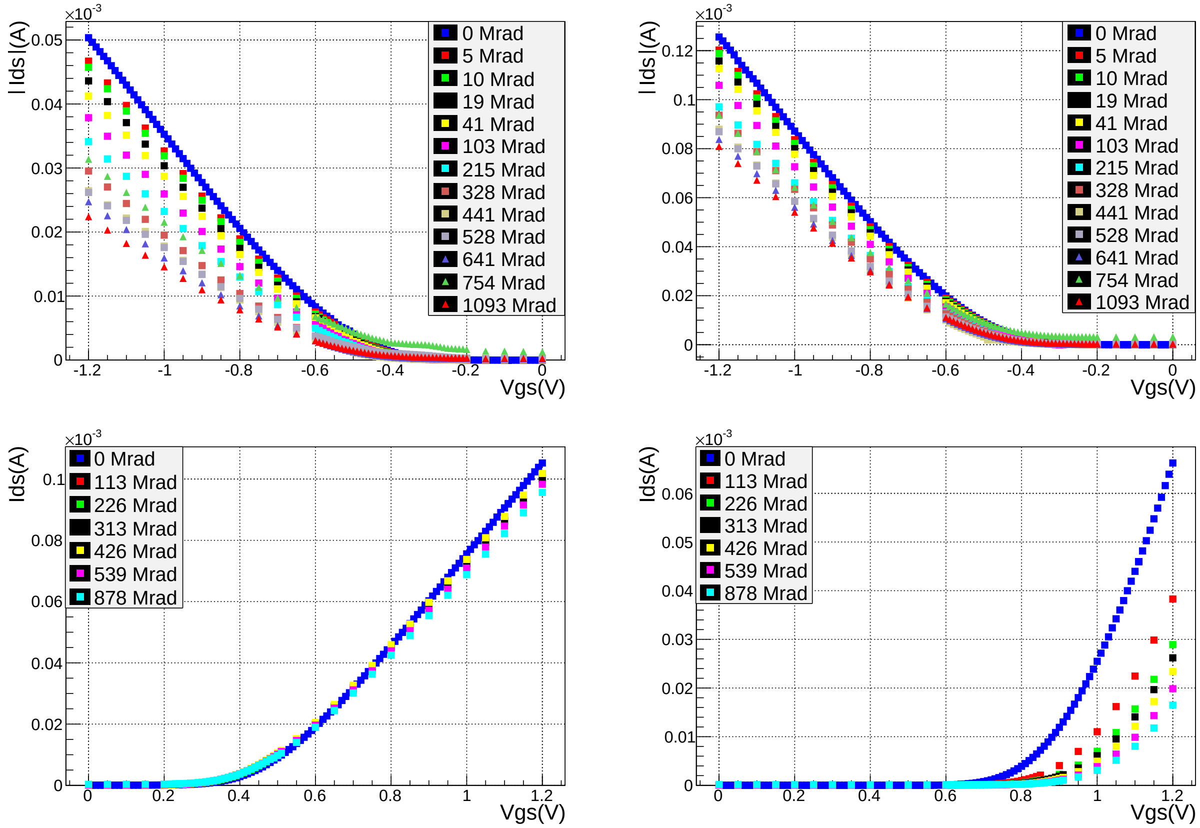

Figure 5.6: Transistor characteristic curves for total dose up to 1.1 Grad of (upper left) a 120/60 core PMOS, (upper right) a 360/60 core PMOS, and for total dose up to 878 Mrad of (lower left) a 240/60 core NMOS, and (lower right) a 1000/280 2.5 V NMOS.

5.5 Summary

The irradiation of 65 nm CMOS transistors held at −20°C was motivated by the need to simulate the actual operating conditions of the HL-LHC CMS pixel detector. Before these tests, it was expected that the radiation damage in 65 nm CMOS transistors would increase when the devices were held at lower temperatures due to less annealing occurring. However, these results show the same pattern of effects that had been observed at room temperature irradiations except the damage observed was less severe, rather than more severe. This could be due to holes and electrons traveling slower through the oxide at lower temperatures and thus, recombining more often[48]. A subsequent test was conducted where the devices were held at three different temperatures, 20, 0, and −20°C, and the results were consistent with the results presented here, where the warmer

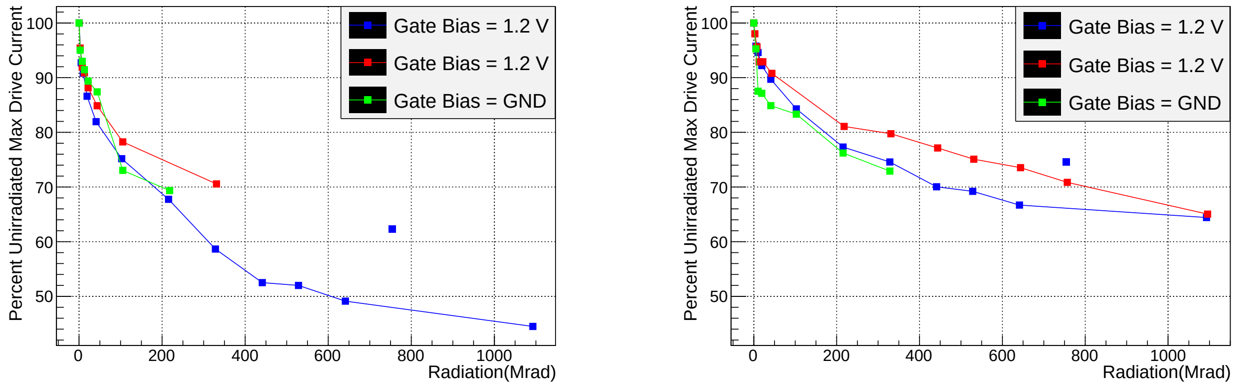

Figure 5.7: The change in maximum drain-source current for similar PMOS core transistors irradiated with different gate bias voltages. The graph on the left is for 120/60 transistors and the graph on the right is for 360/60 transistors. The lines connecting points do not represent a fit, and are included only to make the plots easier to read. The transistor characteristics measured for transistors in one of the test ASIC packages after 754 Mrad was accumulated were all offset by current not likely to have passed through the transistors (this can be seen in Figure 5.6). Lines are not drawn through these points. The most likely source of these offsets is leakage current due to moisture caused by condensation on the cold ASIC package.

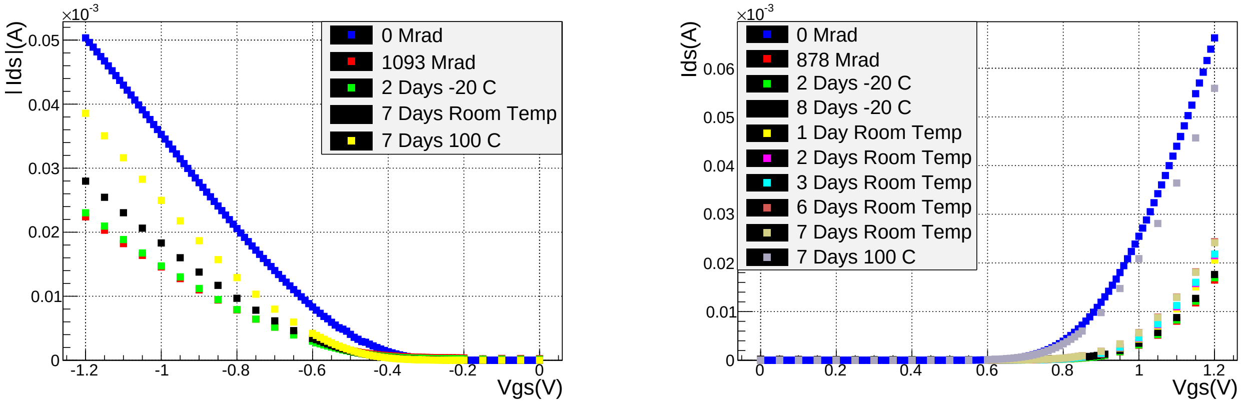

Figure 5.8: Transistor chararcteristic curves during the annealing period for (left) a 120/60 core PMOS and (right) a 1000/280 2.5 V NMOS.

devices had more radiation damage. Based on these studies, it is recommended that the electronics in the HL-LHC pixel detector use all but the smallest sized, 120/60 nm, 65 nm CMOS transistors.

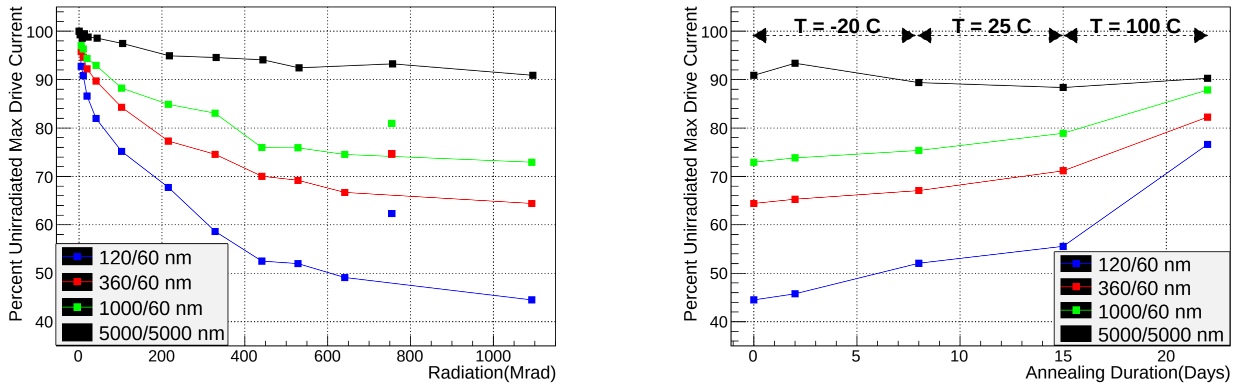

Figure 5.9: The graph on the left shows the loss of maximum drain-source current during irradiation for 4 PMOS core transistors. The graph on the right shows the recovery of maximum drain-source current for the same 4 transistors during and after annealing. As in Figure 5.11, lines are included to make the plots easier to read. Once again, lines are not drawn through the points corresponding to measurements made after 754 Mrad of transistors in one of the ASIC packages.

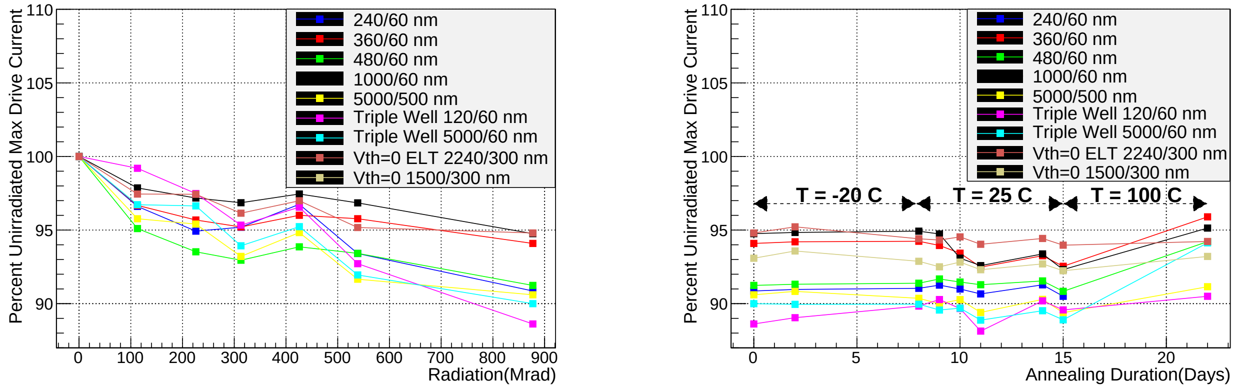

Figure 5.10: The graph on the left shows the loss in maximum drain-source current after each irradiation step for 9 NMOS core transistors. The graph on the right shows the change in maximum drain-source current for the same 9 transistors during and after annealing.

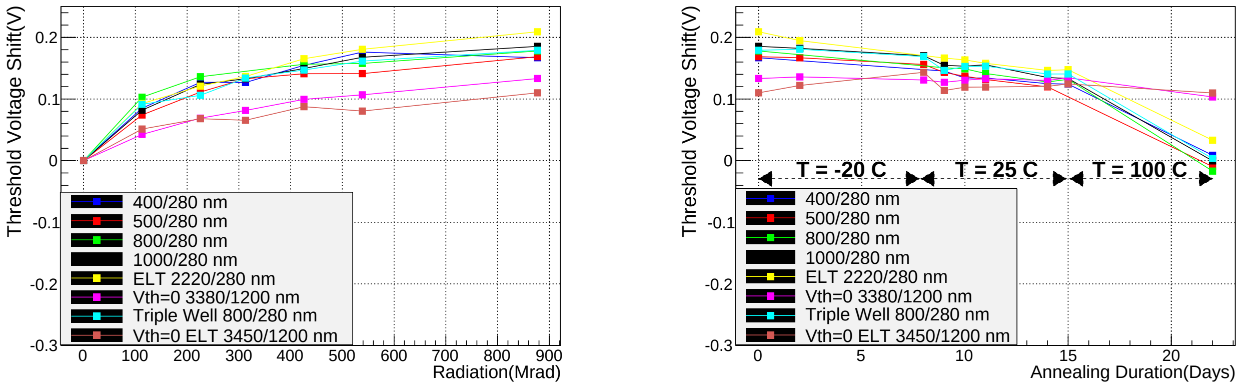

Figure 5.11: The shift in threshold voltage for 8 NMOS I/O transistors irradiated to 878 MRad is shown in the graph on the left, while the graph on the right shows V_{th} for the same 8 transistors during and after annealing. No significant annealing was observed for the two zero V_{th} I/O transistors.

Chapter 6

Search for a heavy resonance decaying to a pair of Higgs bosons in the four b quark final state in proton-proton collisions at $\sqrt{s} = 13$ TeV

The analysis presented in this thesis is the search for a massive resonance decaying into a pair of standard model Higgs bosons in a final state consisting of two b quark-antiquark pairs. The search is performed using a data sample of proton-proton (pp) collisions at a center-of-mass energy of 13 TeV collected by the CMS experiment in 2016 and corresponding to an integrated luminosity of 35.9 fb^{-1}. The Higgs bosons are highly Lorentz-boosted and are each reconstructed as a single large-area jet and identified using jet substructure and b-tagging variables. The signal is characterized by a peak in the dijet invariant mass distribution, above a background from the SM multijet production which is predicted using a data-driven method. The results are consistent with the SM expectations and are interpreted as upper limits on the production cross sections of narrow bulk gravitons and scalar radions in warped extra-dimensional models [50].

This chapter first outlines the strategy of the analysis in Section 6.1. Then, the datasets and triggers are listed in Sections 6.2 and 6.3, respectively. In Section 6.4 the event selection is summarized. A full description of the background estimation technique is given in Section 6.5, followed by the signal modeling in Section 6.6. Section 6.7 discusses the systematic uncertainties and finally, the results are summarized in Section 6.8.

6.1 Motivation and Strategy

The search for resonant Higgs pair production (HH) is a well motivated BSM search that probes the nature of electroweak symmetry breaking and the possible structure of extra dimensions, as outlined in Section 2.4. Previous searches have been performed by the ATLAS [51, 52, 53] and CMS [54, 55, 56, 57] Collaborations in pp collisions at $\sqrt{s} = 7$ and 8 TeV. These searches have included the $bbbb$, $\gamma\gamma bb$, $\tau\tau bb$, and $\gamma\gamma WW^*$ final states and the 95% confidence level upper limits for the searches done at CMS can be seen in Figure 6.1. There are no significant excesses in these results and up to $m_X = 1.1$ TeV the WED theory for $\Lambda_R = 1$ TeV has been excluded. However, the predicted cross section for $\Lambda_R = 3$ TeV is nine times smaller and therefore only limited m_X ranges have been excluded by 8 TeV results. With the LHC now running at 13 TeV and collecting a significantly larger amount of data, HH searches can improve their sensitivity, especially at high resonance masses. This is illustrated in the 8 TeV results, where there is an increase in the upper limits for $m_X > 2$ TeV, suggesting that the searches have reached the limit of their sensitivity. The four b quark final state is a useful topology to explore the high resonance mass region due to the $H \to b\bar{b}$ decay having the largest Higgs branching fraction.

The strategy of this HH analysis is to search for both Higgs bosons decaying through the $H \to b\bar{b}$ channel, where the final state topology is constrained by $m_X/2m_H \gg 1$. This requirement forces each Higgs into the boosted regime, which is defined when the Higgs has large momentum so that its decay products are collimated along its direction of motion and is characterized by $\Delta R \sim 2m/p_T$, where m and p_T are the mass and transverse momentum of the Higgs and ΔR is the angular separation between the two decay products. The hadronization of a narrowly separated $b\bar{b}$ pair arising from a Higgs boson decay will result in a single reconstructed jet, called a Higgs jet, of mass compatible with m_H. The Higgs candidates are selected by employing the jet-grooming algorithm called soft-drop mass [58, 59], a jet substructure variable called N-subjettiness [60, 61], and a double-b tagger [7]. The full Higgs jet selection will be given in Section 6.4.

The background consists mostly of SM multijet production, also called QCD, and is estimated

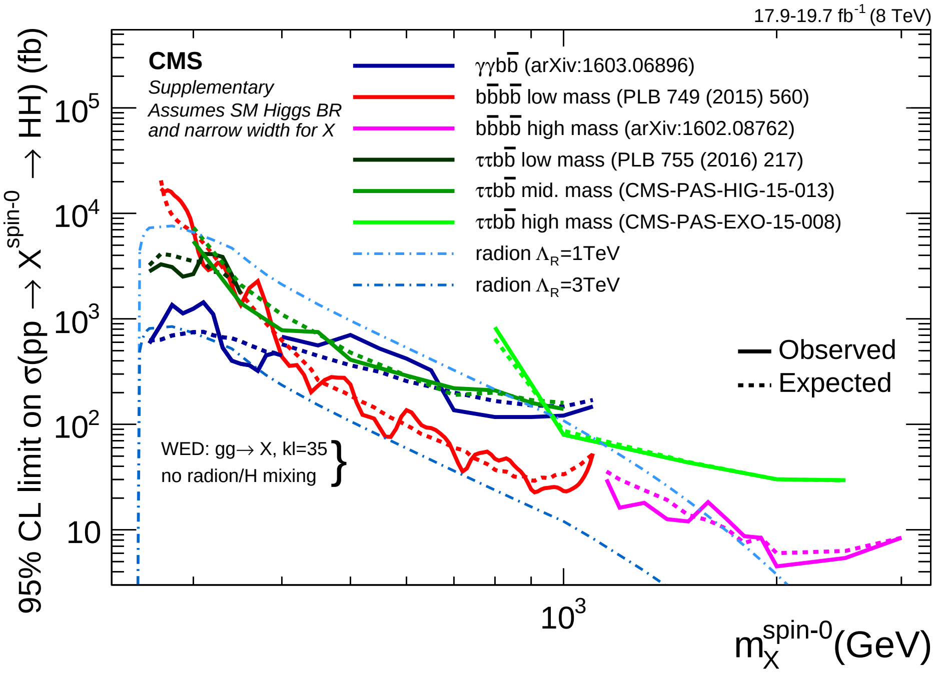

Figure 6.1: Observed and expected 95% confidence level upper limits on the product of the cross section and the branching fraction for the spin-0 radion obtained by different final states explored by the CMS Collaboration at $\sqrt{s}$ = 8 TeV. Theory lines corresponding to different ultraviolet cutoffs are shown.

using a fully data-driven technique that uses several control regions defined in the phase space of the mass and double-b tagging discriminator of the leading p_T Higgs jet. The background is predicted as a function of dijet invariant mass allowing the entire range of m_X to be explored. The signal would appear as a peak in the HH invariant mass spectrum above a smooth background distribution. The complete background estimation technique will be described in more detail in Section 6.5.

6.2 Data and Simulated Samples

The analysis presented in this thesis is performed using 35.9 fb^{-1} of pp collision data at $\sqrt{s} = 13$ TeV collected with the CMS detector in 2016. Table 6.1 lists all of the datasets used and their integrated luminosities.

The Monte Carlo (MC) signal samples used in this analysis are listed in Table 6.2. They include spin-0 bulk gravitons and spin-2 radions produced via gluon-gluon fusion and simulated

Dataset	Processing	Int. lumi. (fb^{-1})
/JetHT/Run2016B	03Feb2017	5.9
/JetHT/Run2016C	03Feb2017	2.6
/JetHT/Run2016D	03Feb2017	4.4
/JetHT/Run2016E	03Feb2017	4.1
/JetHT/Run2016F	03Feb2017	3.2
/JetHT/Run2016G	03Feb2017	7.7
/JetHT/Run2016H	03Feb2017	8.9
Total		35.9

Table 6.1: List of the primary datasets, their data reconstruction campaign, and their corresponding integrated luminosity. The different datasets correspond to different detector and trigger configurations used by CMS.

to leading order (LO) in QCD precision. The samples decay to the four b quark final state and the mass of the resonances range between $750 - 3000$ GeV with a width of 1 MeV, corresponding to the narrow width approximation. The primary versions of these samples are simulated using the MADGRAPH5_aMC@NLO2.3.3 [62] event generator with the NNPDF3.0 leading order parton distribution functions (PDFs) [63] taken from the LHAPDF6 PDF set [64, 65, 66, 67]. The showering and hadronization of partons is simulated with PYTHIA 8.212 [68] with the CUETP8M1-NNPDF23LO [69] tune. The alternate version of these samples are generated with HERWIG++ 2.7.1 and are used to evaluate the systematic uncertainty associated with the parton shower and hadronization, which will be described in Section 6.7. These samples use the EE5C tune [70].

The SM MC samples that were used to determine the background composition and validate the background estimation techniques are listed in Table 6.3. The multijet, diboson, and $W(\rightarrow qq)$+jets samples are generated using MADGRAPH5_aMC@NLO2.3.3, while the $\mathrm{t\bar{t}}$ sample is generated using POWHEG 2.0 [71, 72, 73]. All SM samples are showered and hadronized with PYTHIA 8.

Every MC sample is processed through a GEANT4-based [74, 75] simulation of the CMS detector. The pileup distribution in the generated samples does not exactly model the pileup distribution in data, and therefore the samples are weighted to match the number of pp interactions

Process	Events
Bulk graviton	
GluGluToBulkGravitonToHHTo4B_M-750_narrow_13TeV-madgraph	99200
GluGluToBulkGravitonToHHTo4B_M-800_narrow_13TeV-madgraph	100000
GluGluToBulkGravitonToHHTo4B_M-900_narrow_13TeV-madgraph	100000
BulkGravTohhTohbbhbb_narrow_M-1000_13TeV-madgraph	50000
BulkGravTohhTohbbhbb_narrow_M-1200_13TeV-madgraph	50000
BulkGravTohhTohbbhbb_narrow_M-1400_13TeV-madgraph	50000
BulkGravTohhTohbbhbb_narrow_M-1600_13TeV-madgraph	50000
BulkGravTohhTohbbhbb_narrow_M-1800_13TeV-madgraph	48400
BulkGravTohhTohbbhbb_narrow_M-2000_13TeV-madgraph	50000
BulkGravTohhTohbbhbb_narrow_M-2500_13TeV-madgraph	50000
BulkGravTohhTohbbhbb_narrow_M-3000_13TeV-madgraph	50000
Bulk graviton `Herwig++ samples`	
BulkGravTohhTohbbhbb_narrow_M-1000_13TeV-madgraph-herwig	50000
BulkGravTohhTohbbhbb_narrow_M-2000_13TeV-madgraph-herwig	50000
BulkGravTohhTohbbhbb_narrow_M-3000_13TeV-madgraph-herwig	50000
Radion	
GluGluToRadionToHHTo4B_M-750_narrow_13TeV-madgraph	99800
GluGluToRadionToHHTo4B_M-800_narrow_13TeV-madgraph	100000
GluGluToRadionToHHTo4B_M-900_narrow_13TeV-madgraph	100000
RadionTohhTohbbhbb_narrow_M-1000_13TeV-madgraph	50000
RadionTohhTohbbhbb_narrow_M-1200_13TeV-madgraph	50000
RadionTohhTohbbhbb_narrow_M-1400_13TeV-madgraph	50000
RadionTohhTohbbhbb_narrow_M-1600_13TeV-madgraph	50000
RadionTohhTohbbhbb_narrow_M-1800_13TeV-madgraph	50000
RadionTohhTohbbhbb_narrow_M-2000_13TeV-madgraph	50000
RadionTohhTohbbhbb_narrow_M-2500_13TeV-madgraph	50000
RadionTohhTohbbhbb_narrow_M-3000_13TeV-madgraph	50000

Table 6.2: List of Monte Carlo signal samples used and the number of events generated for each sample.

observed in the data.

6.3 Triggers

Events used in this analysis are selected by trigger algorithms that save events with a large amount of hadronic activity. The L1 seeds for these triggers either select events with a large scalar sum of jet transverse momentum (H_T) or that contain a jet with a high p_T. The HLT algorithms then place requirements on either the event H_T, jet p_T, groomed jet mass, or jet b-

Background		
Process	σ (pb)	size
QCD_HT-100to200	2.785×10^7 (LO)	81,906,377
QCD_HT-200to300	1.717×10^6 (LO)	18,752,566
QCD_HT-300to500	3.513×10^5 (LO)	20,312,907
QCD_HT-500to700	3.163×10^4 (LO)	19,755,616
QCD_HT-700to1000	6.831×10^3 (LO)	15,595,234
QCD_HT-1000to1500	1.207×10^3 (LO)	4,966,123
QCD_HT-1500to2000	119.9 (LO)	3,964,488
QCD_HT-2000toinf	25.24 (LO)	1,984,407
TT_TuneCUETP8M1_13TeV-powheg-pythia8	831.76 (NNLO)	19,757,190
TT_TuneCUETP8M1_13TeV-powheg-pythia8	831.76 (NNLO)	96,834,559
WW_TuneCUETP8M1_13TeV-pythia8	118.7 (NNLO)	993214
WZ_TuneCUETP8M1_13TeV-pythia8	47.13 (NLO)	1000000
ZZ_TuneCUETP8M1_13TeV-pythia8	16.52 (NLO)	989312
WJetsToQQ_HT-600ToInf_TuneCUETP8M1_13TeV-madgraphMLM-pythia8	95.14 (LO)	1025005

Table 6.3: List of background Monte Carlo samples used. The two $t\bar{t}$ POWHEG samples correspond to two different productions with the same generator parameters, but the latter with much higher statistics. The cross sections, σ, and number of events generated are also given.

tagging. The trigger paths used are listed in Table 6.4. In Run2016H, the `HLT_PFHT800` trigger is prescaled, meaning the overall trigger output rate is reduced by a set amount, and hence the path `HLT_PFHT900` is added to compensate for this.

The trigger requirement is applied to both data and MC and to compensate for the difference in trigger response between data and simulation, trigger efficiency scale factors, defined as the ratio of the trigger efficiency as measured in data to that in MC, are applied to the simulated events. A baseline trigger of `HLT_PFJet260` is used to select events for the measurement of the trigger efficiency. This trigger is prescaled over much of the run period, yet provides enough events for measurements of the efficiencies and the scale factors. Events passing the baseline trigger are further required to pass selection criteria close to the signal selection in the actual analysis:

- The leading two AK8 jets in the event have $p_T > 300$ GeV and $|\eta| < 2.4$.
- The soft-drop mass of the two AK8 jets is $105 < m_{\text{soft drop}} < 135$ GeV, with all necessary

HLT path	L1 seeds
`PFHT650_WideJetMJJ900DEtaJJ1p5`	`HTT160/300/320/270/280/240/220/200/255`
`AK8PFHT650_TrimR0p1PT0p03Mass50`	`HTT240/255/270/280/300/320`
`AK8PFHT700_TrimR0p1PT0p03Mass50`	`HTT240/255/270/280/300/320`
`PFHT800`	`HTT160/300/320/270/280/240/220/200/255`
`PFHT900`	`HTT160/300/320/270/280/240/220/200/255`
`AK8PFJet360_TrimMass30`	`SingleJet180/200`
`AK8DiPFJet280_200_TrimMass30_BTagCSV_p20`	`SingleJet180/200`

Table 6.4: The trigger paths used and their corresponding L1 seeds.

jet mass corrections applied.

- $|\Delta\eta(\mathrm{j}_1, \mathrm{j}_2)| < 1.3$ for the leading two AK8 jets.

The details of these variables and selections are later described in Section 6.4.

The trigger efficiency is measured as a function of the "reduced dijet invariant mass," m_{jj}^{red}, which is the invariant mass of the leading two AK8 jets after a kinematic transformation has been applied. Section 6.4.2.3 explains the kinematic transformation. The efficiency has a slight dependence on $|\Delta\eta(\mathrm{j}_1, \mathrm{j}_2)|$ and hence the efficiency is measured in three $|\Delta\eta(\mathrm{j}_1, \mathrm{j}_2)|$ regions: 0.0 – 0.434, 0.434 – 0.868, and 0.868 – 1.3. The efficiencies in data and MC are shown in Fig. 6.2. The combined set of triggers reaches full efficiciency for $m_{jj}^{red} > 1100$ GeV over all of the $|\Delta\eta(\mathrm{j}_1, \mathrm{j}_2)|$ ranges. For $m_{jj}^{red} < 1100$ GeV, the trigger efficiencies are higher for smaller $|\Delta\eta(\mathrm{j}_1, \mathrm{j}_2)|$, where most of the signal lie, and are smaller at larger values of $|\Delta\eta(\mathrm{j}_1, \mathrm{j}_2)|$.

Since the search begins from $m_{jj}^{red} = 750$ GeV, the modeling of the trigger efficiency curves in data and simulation is done extremely carefully. Originally, the trigger efficiency was measured using an orthogonal trigger path `HLT_Mu50`. However, the switch to the `HLT_PFJet260` trigger was made because the final event selection vetoes events with isolated leptons and therefore the `HLT_Mu50` selection is completely orthogonal to the signal region. The baseline trigger `HLT_PFJet260` has some inefficiency for low m_{jj}^{red} and therefore an additional uncertainty is assigned to the trigger efficiency scale factor based on this trigger's efficiency in MC. Figure 6.3 shows the `HLT_PFJet260` trigger turn-on curves for different $|\Delta\eta(\mathrm{j}_1, \mathrm{j}_2)|$ in MC, with respect to only the event selection. The

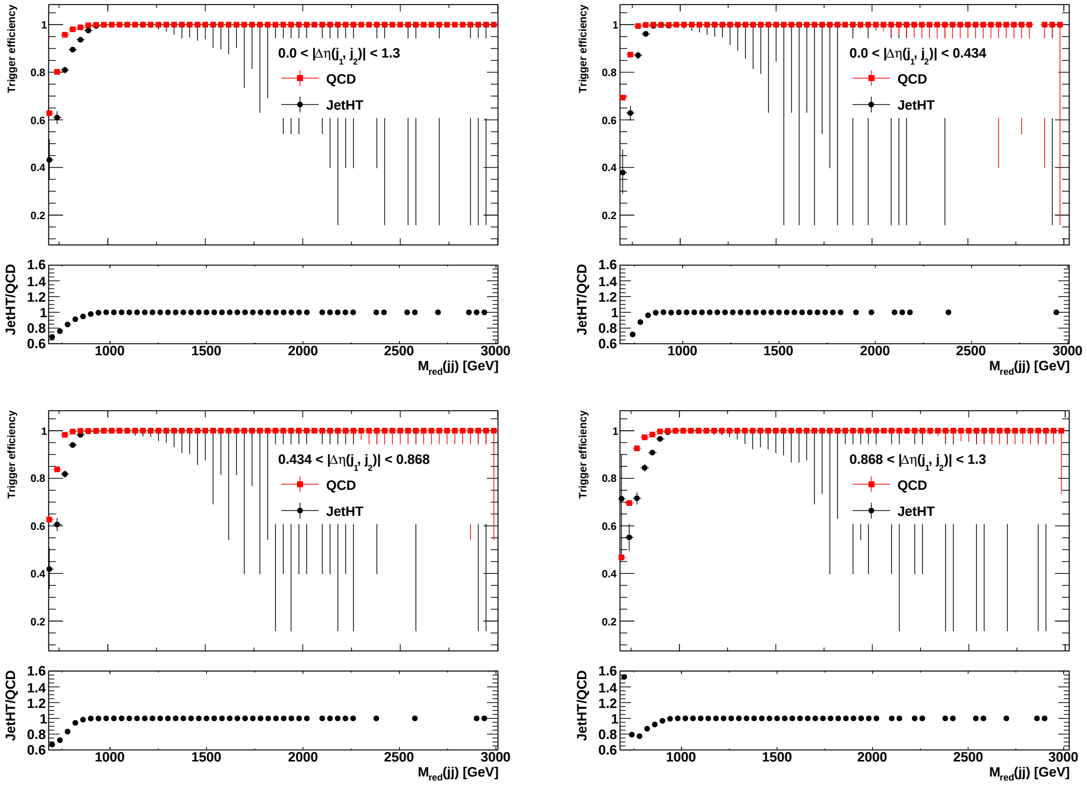

Figure 6.2: The trigger efficiency, as a function of m_{jj}^{red}, in the JetHT dataset and QCD MC for different $|\Delta\eta(\mathrm{j}_1, \mathrm{j}_2)|$ regions: 0.0 – 1.3 (upper left), 0.0 – 0.434 (upper right), 0.434 – 0.868 (lower left), and 0.868 – 1.3 (lower right).

difference between unity and the trigger efficiency is propagated to the scale factor as a systematic uncertainty.

6.4 Event Selection

After passing the triggers, events are required to have at least one reconstructed *pp* collision vertex satisfying the following criteria:

- Vertex number of degrees of freedom > 4.
- Absolute displacement from the beamspot position along the z direction < 24 cm.
- Absolute displacement from the beamspot position along the transverse direction < 2 cm.

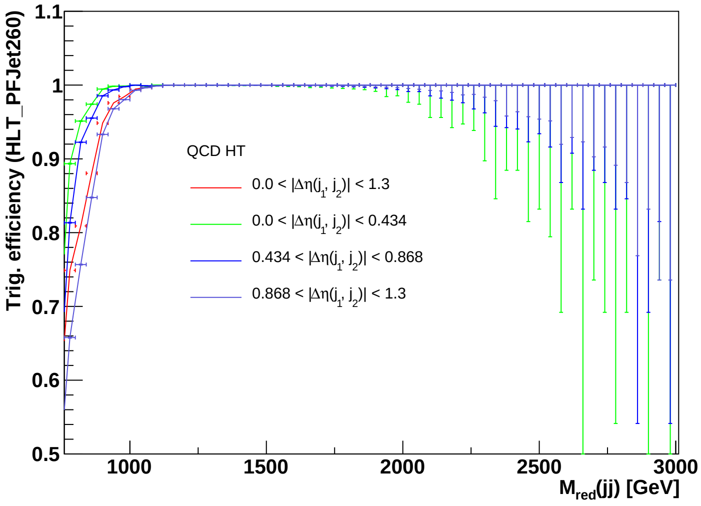

Figure 6.3: The trigger efficiency in QCD MC for the baseline trigger HLT_PFJET260, as a function of m_{jj}^{red}, for different $|\Delta\eta(\mathrm{j}_1, \mathrm{j}_2)|$ regions: $0.0 - 1.3$, $0.0 - 0.434$, $0.434 - 0.868$, and $0.868 - 1.3$. The percentage difference between one and these turn-on curves is taken as an uncertainty on the trigger efficiency scale factor.

Many additional vertices, corresponding to other overlapping pp collisions (pileup), are usually reconstructed in an event using charged particle tracks. The primary interaction vertex (PV) corresponds to the vertex that maximizes the sum in p_T^2 and the magnitude of $\sum p_T$ from the associated physics objects.

6.4.1 Lepton Selection

To suppress $\mathrm{t\bar{t}}$ and diboson backgrounds, events containing an isolated electron or muon with $p_T > 20$ GeV are removed. The isolation requirement is designed to remove jets misidentified as leptons and is defined as the ratio of energy surrounding the lepton to the lepton's momentum. The energy surrounding a lepton is the scalar p_T sum of the charged hadrons, neutral hadrons, and photons in a cone with size $\Delta R = 0.3$ and $\Delta R = 0.4$ for electrons and muons, respectively. The identification criteria for an electron are listed in Table 6.5 and the muon identification criteria are listed in Table 6.6. The combined isolation and identification requirement of the electron is such that the overall selection efficiency is 90% (70%) for the "loose" ("medium") requirement. For the “loose” (“medium”) muons, the selection efficiency is 100% (95%). Events are rejected if they contain one lepton passing the medium requirement or two leptons passing the loose requirement that have the same flavor but opposite charge.

	Barrel Selection		Endcap Selection	
Variable	Loose	Medium	Loose	Medium
$5 \times 5\ \sigma_{i\eta i\eta} <$	0.011	0.00998	0.0314	0.0298
$\Delta\eta_{seed} <$	0.00477	0.00311	0.00868	0.00609
$\Delta\phi_{in} <$	0.222	0.103	0.213	0.045
H/E <	0.298	0.253	0.101	0.0878
$\lvert\frac{1}{E} - \frac{1}{p}\rvert <$	0.241	0.134	0.14	0.13
Missing hits $\leq$	1	1	1	1
Conversion veto	yes	yes	yes	yes

Table 6.5: Loose and medium electron identification criteria used in the analysis. The selection criteria vary depending on if the electron is in the barrel or endcap of the detector. $\sigma_{i\eta i\eta}$ is the energy weighted standard deviation of a single crystal within the 5×5 cluster of crystals centered at the crystal with maximum energy and $\Delta\eta_{seed}$ refers to the η difference between the seed and the track. $\Delta\phi_{in}$ is the difference ϕ difference between the supercluster and positions of the inner track extrapolated from the interaction vertex and H/E refers to the energy measured in the hadronic calorimeter divided by the energy measured in the electromagnetic calorimeter.

Loose	Medium
Global or Tracker Muon	Global Muon
PF Muon	Normalized χ^2 of the global track < 3
	Tracker-Standalone position match < 12
	Kink finder < 20
	segment compatibility > 0.303
	OR
	segment compatibility > 0.451

Table 6.6: Loose and medium muon identification criteria used in the analysis. The segment compatibiliy refers to the compatibility of the global muon track to the track formed using just the segments in the muon detector.

6.4.2 Jet Selection

Particle Flow (PF) candidates are clustered using the anti-k_t algorithm [76], implemented in FastJet [77], into jets with a distance parameter $R = 0.8$ (referred to as AK8 jets). To mitigate the effect of pileup, particles are assigned weights using the pileup per particle identification (PUPPI) algorithm [78]. This method uses local shape information, event pileup properties, and tracking information to compute a weight describing the degree to which a particle is pileup-like. Charged particles from pileup vertices receive a weight of zero, while those from the primary vertex receive a weight of one. Neutral particles are assigned a weight between zero and one, where higher values correspond to a particle more likely to originate from the primary vertex.

To account for detector response nonlinearity, jet energy corrections (JECs) are applied as a function of jet η and p_T [79, 80]. The JECs applied to both data and MC are known as L2L3 MC-truth corrections. This correction is derived from simulation and is designed to make the jet response uniform in η and p_T. An additional L2L3 residual correction is applied to data events to correct for the small differences within jet response in data and MC. The procedure for the uncertainties associated with these corrections is described in Section 6.7.

In each event, the $H \to \mathrm{b\bar{b}}$ system is reconstructed as a single high-p_T AK8 jet, where the decay products have merged within the jet, and the two highest p_T jets in the event are assumed to be the Higgs boson candidates. At lower Higgs momentum, the two b quarks from the Higgs decay have a large angular separation and can be reconstructed as two smaller cone size jets. The turnover in reconstruction efficiency between the boosted and resolved case takes place between a p_T of 200 and 300 GeV, which is illustrated in Figure 6.4. Therefore, the Higgs candidates in this analysis are required to have $p_T > 300$ GeV. The candidates are also required to have $|\eta| < 2.4$ because that is the coverage of the tracker barrel and the double-b tagger is only certified in the barrel region due to the granularity of the tracker.

Each jet is also required to pass the tight jet identification requirements provided by the CMS JetMET physics analysis group. These selections require a jet to have a neutral hadron fraction < 0.9, a neutral EM fraction < 0.9, a muon fraction < 0.8, a charged hadron fraction > 0, a charged EM fraction < 0.9, and more than 1 constituent. The hadron fraction is the percentage of jet constituents taken from HCAL hits, the EM fraction is the percentage of jet constituents taken from ECAL hits, and the muon fraction is the percentage of constituents taken from the muon

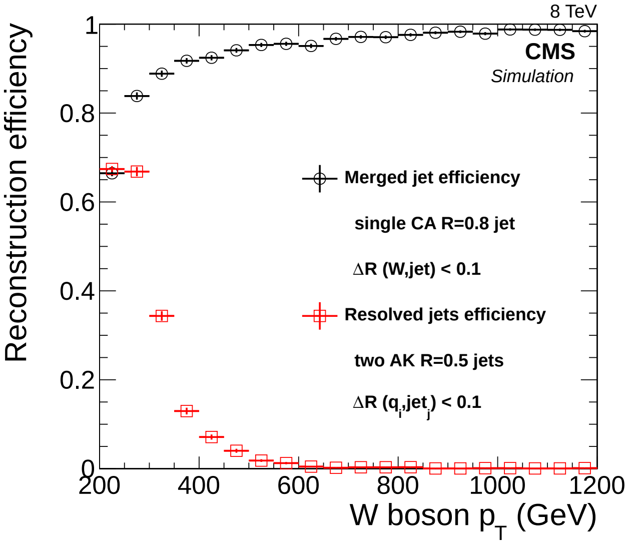

Figure 6.4: Efficiency to reconstruct a Cambridge-Aachen jet with a cone size of 0.8 (CA8) within $\Delta R < 0.1$ of a generated W boson, and the efficiency to reconstruct two anit-k_t jets with a 0.5 cone size (AK5) within $\Delta R < 0.1$ of the generated quarks from the W boson, as a function of the p_T of the W boson [10] Here, the fatjet is clustered with the CA algorithm but the reconstruction efficiency does not depend on the jet algorithm that is used to cluster the jets. Also, the same trend occurs for reconstructed Higgs bosons with large p_T, although the turnover in efficiency between a single fatjet and two smaller jets takes place at a slightly higher p_T due to the higher mass of the Higgs compared to the W boson.

detector. These requirements are summarized in Table 6.7.

Variable	Cut
Neutral Hadron Fraction	< 0.90
Neutral EM Fraction	< 0.90
Number of Constituents	> 1
Muon Fraction	< 0.8
Charged Hadron Fraction	> 0
Charged Multiplicity	> 0
Charged EM Fraction	< 0.90

Table 6.7: Tight jet identification quality criteria used in the analysis.

6.4.2.1 Candidate Higgs Selection

To further reduce the large amount of QCD background, a set of jet requirements is applied that distinguish a quark/gluon-initiated jet (QCD jet) from a Higgs jet. Jets that originate from a Higgs have different phenomenological properties than QCD jets and these properties can be exploited by comparing the mass of the jet, the substructure of the jet, and the flavor of the jet.

To begin, the masses of the two leading jets can be used to suppress the multijet and $\mathrm{t\bar{t}}$ backgrounds. The jet is first groomed [81] to mitigate the effects of initial state radiation, underlying event activity, and pileup using the soft-drop algorithm [82, 59]. The soft-drop algorithm is a declustering algorithm that recursively removes soft, wide-angle radiation from a jet. The soft-drop declustering procedure begins by undoing the last step of jet clustering by breaking the jet, j, into two subjets, j_1 and j_2. If the subjets pass the soft-drop condition

$$\frac{\min(p_{T1}, p_{T2})}{p_{T1} + p_{T2}} > z_{cut}\left(\frac{\Delta R_{12}}{R_0}\right)^{\beta}, \tag{6.1}$$

then the original jet is kept as the final jet. Otherwise, the subjet with the lowest p_T is thrown away, j is redefined as the remaining subjet, and the declustering is repeated until the soft-drop condition is satisfied. Here, p_{Ti} is the transverse momenta of the two constituents, ΔR_{12} is the angular distance between the constituents, R_0 is the size of the jet, z_{cut} is the soft-drop threshold, and β is an angular component where $\beta \to \infty$ returns an ungroomed jet. In this analysis, z_{cut} is set to 0.1 and $\beta = 0$.

The groomed jet is used to calculate the soft-drop jet mass and dedicated mass corrections, which are derived from data and simulation in a region enriched in $\mathrm{t\bar{t}}$ events with merged $W \to q\bar{q}$ decays [83], are applied in a two step procedure. First, a weight to account for a p_T dependent soft-drop jet mass shift introduced at generator level is computed. Then an additional weight, to account for any residual p_T and η dependence, is calculated based on the difference between the reconstructed and the generated soft-drop mass. These corrections applied to a Higgs jet yield a mass stable with p_T and number of pileup interactions, peaking around 120 GeV. The difference of ∼5 GeV relative to the nominal Higgs mass is related to the presence of neutrinos produced by the semi-leptonic decays of B mesons. For quark/gluon-initiated jets, the removal of underlying events pushes the jet mass to lower values and the distribution has much smoother behavior than ungroomed jets, as seen in Figure 6.5. In this analysis, the soft-drop masses of each jet are required to fall within the range $105 - 135$ GeV, which corresponds to an efficiency of about $60 - 70\%$ depending on the mass of the X resonance.

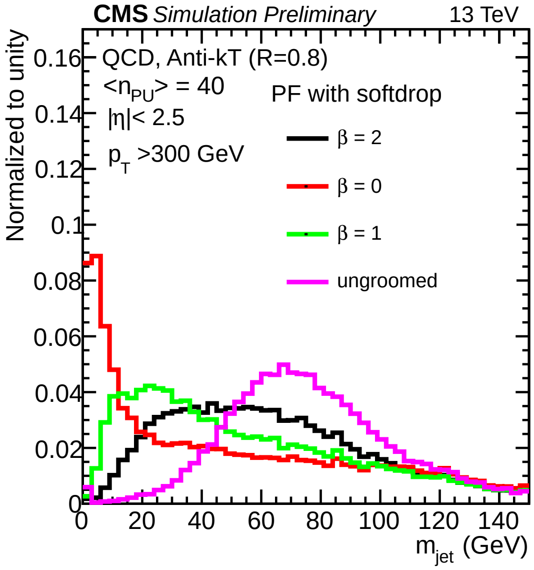

Figure 6.5: Jet mass distributions of simulated QCD jets with $p_T > 300$ GeV for jets with different soft-drop parameters. The ungroomed jet mass is also shown [11].

An additional observable that can distinguish QCD jets from Higgs jets is the substructure of a jet. A Higgs jet has two prongs of energy within it corresponding to each of the b quarks, whereas a QCD jet has energy uniformly distributed throughout the jet cone. The algorithm used to quantify the degree to which a jet's constituents can be arranged in N subjets is called "N-subjettiness" [61], or τ_N, where

$$\tau_N = \frac{1}{\sum_k p_{T,k} R_0} \sum_k p_{T,k} \mathrm{min}(\Delta R_{1,k}, \Delta R_{2,k} ..., \Delta R_{N,k}). \tag{6.2}$$

Here, k runs over the constituents of a jet, $\Delta R_{j,k}$ is the angular distance between a subjet axis j and a constituent k, and R_0 is the size of the jet. The subjet axes are identified using the exclusive-k_t clustering algorithm [84, 85]. Jets with $\tau_N = 0$ are consistent with a jet containing N or fewer subjets since all of their constituents are aligned with the subjet axes.

To distinguish jets containing two subjets from jets with a single subjet, the ratio $\tau_{21} = \tau_2/\tau_1$ has been shown to have the most discrimination power [60]. Figure 6.6 illustrates that small values of τ_{21} indicate a jet is consistent with containing two subjets. Both of the jets in this analysis are required to have $\tau_{21} < 0.55$ which is the loose working point supported by the CMS JetMET Algorithms and Reconstruction POG and was chosen because tighter working points caused a reduction in expected sensitivity. The τ_{21} selection has a jet p_T-dependent signal efficiency of $50 - 70\%$, before applying the soft-drop mass requirement.

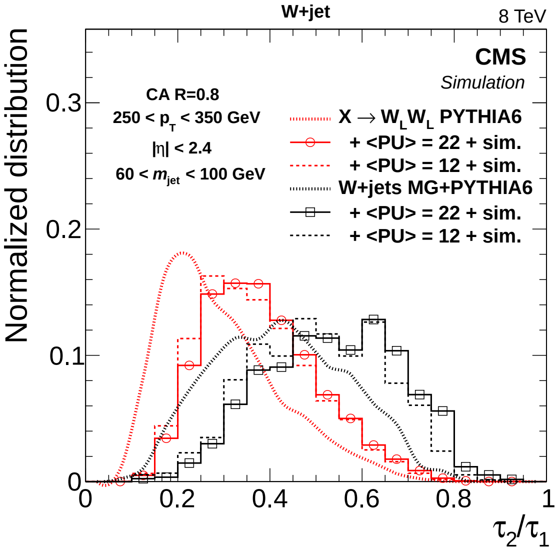

Figure 6.6: Distribution of τ_2/τ_1 in simulated samples of highly boosted W bosons and inclusive QCD jets after a jet mass selection of $60 < m_{jet} < 100$ GeV. Thick dashed lines represent the generator predictions without pileup interactions and without CMS detector simulation. The histograms are the expected distributions after full CMS simulation with pileup corresponding to an average number of 12 and 22 interactions [11]. Here, the W bosons decay to a pair of quarks, but the τ_{21} distribution is very similar for Higgs bosons decaying to a pair of b quarks.

Finally, the main method to suppress multijet background is through b tagging and since a Higgs jet is expected to contain two b quarks, the dedicated "double-b tagger" algorithm [7] is used. Due to the long decay time of a b quark, there are secondary vertices (SV) within a Higgs jet corresponding to each of the b quarks. These secondary vertices are then associated to a subjet axis, which are defined in the N-subjettiness observables, to form a two-SV system. The secondary vertices, reconstructed tracks, and information from the two-SV system are used as input to the multivariate tagging discriminator with an output between -1 and 1, where a higher value indicates a greater probability for the jet to contain a $b\bar{b}$ pair, as shown in Figure 6.7.

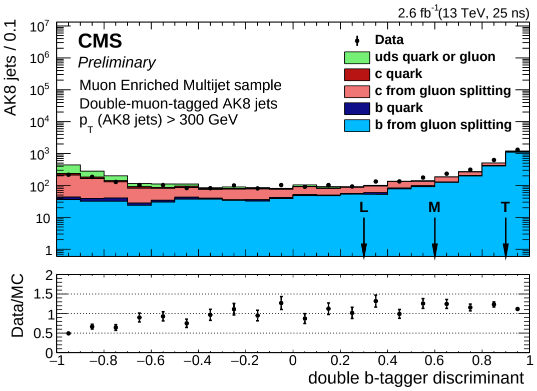

Figure 6.7: Double-b tagger discriminant distribution in data and simulated samples for the double-muon tagged jets selection. Simulated events are normalized to the yield observed in data. The loose, medium and tight operating points are also reported. The bottom panel shows the ratio of the number of events observed in data to that of the MC prediction [7].

The double-b discriminator working points that are supported by the CMS BTagging and Vertex POG are loose (“L”, > 0.3), medium (“M”, > 0.6), and tight (“T”, > 0.8) corresponding to signal efficiencies of 80%, 65%, and 30%, respectively. The working points used in this analysis were optimized separately for low and high p_T jets by applying the full event selection and running the analysis framework on data to calculate the 95% confidence level expected upper limits on the production cross section $\sigma(\text{pp} \to \text{X})B(\text{X} \to \text{HH} \to \text{b}\bar{\text{b}}\text{b}\bar{\text{b}})$ as a function of bulk graviton mass. The following combinations of double-b tagger working points were investigated:

- TT: both jets pass the tight selection;
- TM: one jet passes the tight selection and one passes the medium selection;

- TL: one jet pass the tight selection and one passes the loose selection;
- MM: both jets pass the medium selection;
- ML: one jet passes the medium selection and one passes the loose selection;
- LL: both jets pass the loose selection.

Figure 6.8 compares the expected limits for these combinations across a wide range of bulk graviton masses. The optimal choice results in the tight working point for low and medium p_T jets while the loose working point is optimal for high p_T jets. Therefore, our events were classified into two orthogonal categories, TT and LL. These categories are kept orthogonal by requiring at least one jet in the LL category to fail the tight working point. The backgrounds are estimated separately for each category, and the combination of the likelihoods for the TT and LL categories gives the optimal signal sensitivity over a wide range of resonance masses, according to studies performed using simulated signal and multijet samples. The TT category has a good background rejection for $m_X < 2000$ GeV while at higher resonance masses, where the background is small, the LL category provides better signal sensitivity.

6.4.2.2 Jet η Separation

For multijet background events, the two candidate Higgs jets have a large separation in η. In contrast, the signal events are characterized by a small separation of the two leading p_T jets in η. To determine the optimal value for the $|\Delta\eta(\mathrm{j}_1, \mathrm{j}_2)|$ selection, the value of $\frac{\epsilon_{\mathrm{signal}}}{1+\sqrt{N_{\mathrm{bkg}}}}$ was used as a figure of merit (FOM), where $\epsilon_{\mathrm{signal}}$ is the signal efficiency, and N_{bkg} is the number of background events passing the $|\Delta\eta(\mathrm{j}_1, \mathrm{j}_2)|$ selection criteria. The results are shown in Figure 6.9 and 6.10 for different bulk graviton and radion masses, respectively. Below a resonance mass of 2 TeV, the FOM favors $|\Delta\eta(\mathrm{j}_1, \mathrm{j}_2)| < 1.1 - 1.3$, while for higher masses, a looser $|\Delta\eta(\mathrm{j}_1, \mathrm{j}_2)|$ selection is optimal, given that the background levels fall steeply. The η separation between the Higgs bosons in the resonance decay varies depending on the spin of the resonance, where the decay products from a graviton

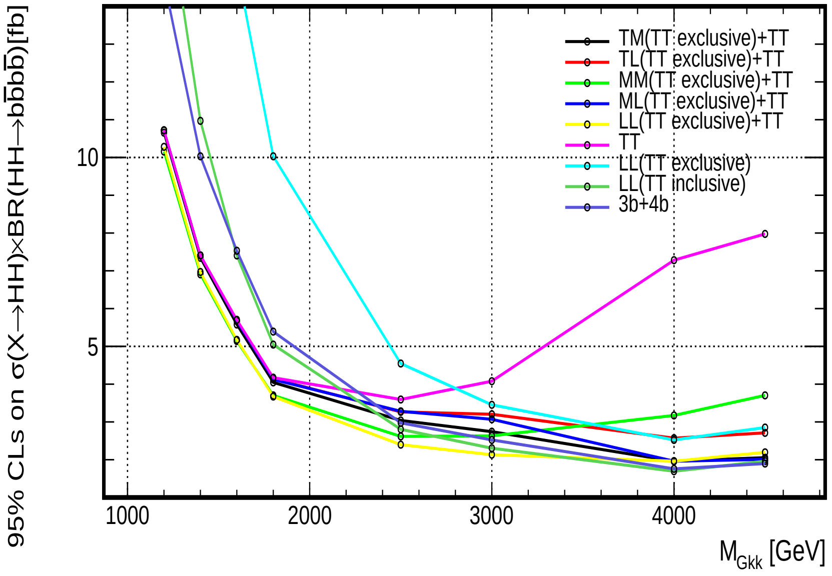

Figure 6.8: The 95% confidence level expected upper limits as a function of bulk graviton resonance mass for different b-tagging categories. Note, when combining the TT category with other categories, the TT events are excluded, which is labeled as "TT exclusive." The limits using a subjet single b tagging selection (3b + 4b) are also shown for comparison.

have a smaller separation than the decay products from a radion of the same mass. However, the $|\Delta\eta(\mathrm{j}_1, \mathrm{j}_2)|$ selection changes the trigger turn-on, and hence the background shapes would differ for low and high mass searches, or radion and graviton searches, if different trigger turn-ons are used. Therefore, a single selection of $|\Delta\eta(\mathrm{j}_1, \mathrm{j}_2)| < 1.3$ for all masses for both the bulk graviton and the radion is used.

6.4.2.3 Di-jet Mass

The di-jet mass of the leading two Higgs jets in the event correspond to the invariant mass of the resonance searched for. However, it is well known that techniques such as a kinematic fit that constrains the mass of each Higgs candidate to the mass of the Higgs, m_H, improves the resonance resolution and ultimately the sensitivity [86]. For this analysis, the groomed and ungroomed Higgs candidate masses constrained by m_H were considered to improve the resolution of m_{jj}. It was

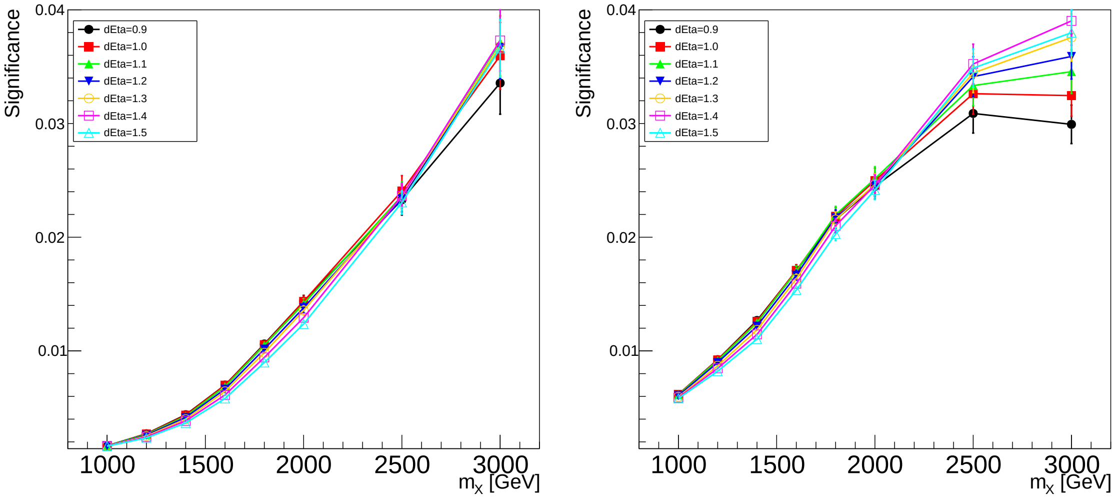

Figure 6.9: The significance, $\frac{\epsilon_{\text{signal}}}{1+\sqrt{N_{\text{bkg}}}}$, of the $|\Delta\eta(\mathrm{j}_1,\mathrm{j}_2)|$ selection for various selection values as a function of the bulk graviton signal mass for the LL category (left) and the TT category (right).

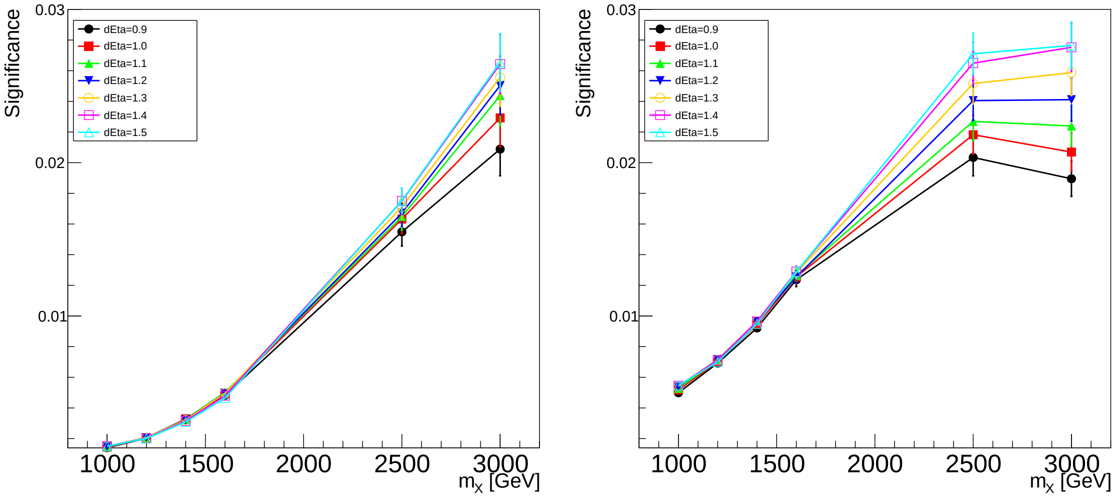

Figure 6.10: The significance, $\frac{\epsilon_{\text{signal}}}{1+\sqrt{N_{\text{bkg}}}}$, of the $|\Delta\eta(\mathrm{j}_1,\mathrm{j}_2)|$ selection for various selection values as a function of the radion signal mass for the LL category (left) and the TT category (right).

found that the "reduced di-jet invariant mass,"

$$m_{jj}^{red} \equiv m_{jj} - (m_{j_1} - m_H) - (m_{j_2} - m_H), \tag{6.3}$$

provides the best resolution improvement and the mean position of m_{jj}^{red} remained at $\approx m_X$. Here,

m_{j_1} and m_{j_2} are the soft-drop masses of the two candidate Higgs. A comparison between m_{jj} and m_{jj}^{red} is shown in Figure 6.11 for different resonance masses. The kinematic transformation of m_{jj} corrects for fluctuations in m_{j_1} and m_{j_2} due to the jet mass resolution which leads to an $8-10\%$ improvement in the di-jet mass resolution. A requirement of $m_{jj}^{red} > 750$ GeV is applied to events because this is the high resonance mass range that this search looked for.

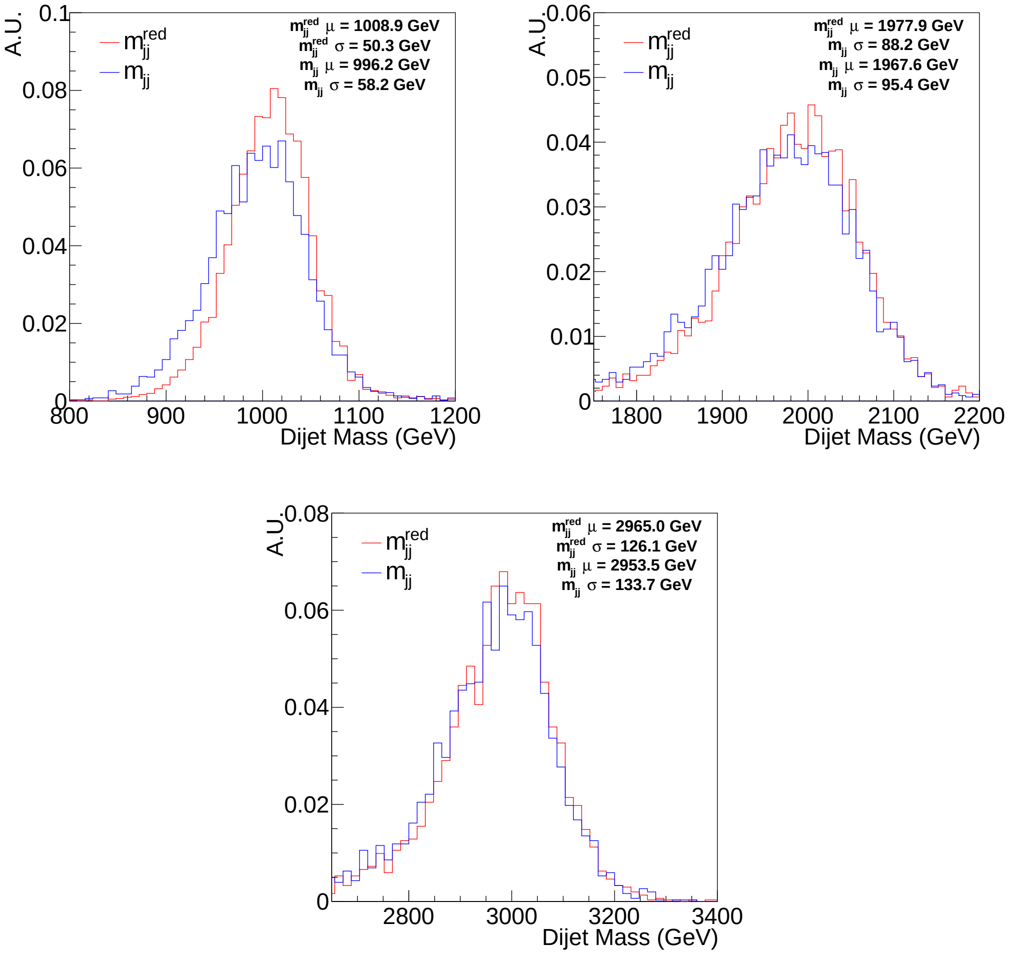

Figure 6.11: The reduced di-jet mass distribution computed as described in Eqn. 6.3 compared to the standard di-jet invariant mass for simulated signal events. The m_{jj}^{red} distributions have a narrower di-jet mass distribution than the m_{jj} distribtuions for each mass point. The simulated bulk graviton mass points are 1000 (top left), 2000 (top right), and 3000 (bottom) GeV.

6.4.3 Full Selection

The entire event selection is summarized in Table 6.8. To determine the background composition, the full event selection is applied to QCD, $\mathrm{t\bar{t}}$, and diboson simulated events. The non-QCD events comprise $\sim$1% of the total background and this can be seen in the invariant di-jet mass distribution in simulation that is shown in Figure 6.12. Therefore, the background is estimated using a single technique rather than a different method for each separate process.

The cut-flow efficiency for the bulk graviton and radion samples is shown in Tables 6.9 and 6.10, respectively. The full event selection efficiencies for both double-b tagger categories are also shown in Figure 6.13. The radion has a smaller efficiency than the bulk graviton because its $|\Delta\eta(\mathrm{j}_1, \mathrm{j}_2)|$ distribution is considerably wider than that of a bulk graviton of the same mass, as shown in Figure 6.14. Figures 6.14−6.17 compare the distributions of simulated QCD events to bulk graviton and radion signals with a mass of 1.4 and 2.5 TeV for the kinematic, jet substructure, and double-b tagger variables of the candidate Higgs jets after the full selection except for b-tagging is applied. In addition, when comparing a variable X, such as τ_{21}, the selection criteria on that variable is removed. For the comparison, a signal cross section of 20 pb is assumed for each signal mass point. The simulated QCD events are subdivided into different categories based on the matched hadron flavor: jets having two B hadrons (bb) or one (b), jets having a charm hadron (c), and all other jets (light).

6.5 Background Estimation

The background is estimated in bins of the m_{jj}^{red} distribution, where two different background modeling techniques are used depending on whether the resonance mass is in the m_{jj}^{red} region where the triggers are fully efficient or not. Above the trigger turn-on, $m_{jj}^{red} \geq 1100$ GeV, the background is smoothly falling and therefore the shape can be modeled by a monotonically decreasing function and the “Alphabet Assisted Bump Hunt” (AABH) method is used. Below the trigger turn-on, $m_{jj}^{red} < 1100$ GeV, the inefficiency in the trigger causes the background to not fall smoothly and

Selection
`PFHT650_WideJetMJJ900DEtaJJ1p5` OR `AK8PFHT650_TrimR0p1PT0p03Mass50` OR `AK8PFHT700_TrimR0p1PT0p03Mass50` OR `PFHT800` OR `PFHT900` OR `AK8PFJet360_TrimMass30` OR `AK8DiPFJet280_200_TrimMass30_BTagCSV_p20`
Veto events with one medium lepton or two opposite sign loose leptons
Number of good vertices ≥ 1
Candidate Higgs jet ID passes the tight working point
Candidate Higgs jet $p_T > 300$ GeV
Candidate Higgs jet $\lvert\eta\rvert < 2.4$
$\lvert\Delta\eta(\mathrm{j}_1, \mathrm{j}_2)\rvert < 1.3$
$m_{jj}^{red} > 750$ GeV
Candidate Higgs jet soft-drop mass $105 < m_j < 135$ GeV
Candidate Higgs jet $\tau_{21} < 0.55$
Candidate Higgs jet double b discriminator > 0.3

Table 6.8: Full selection criteria for the analysis.

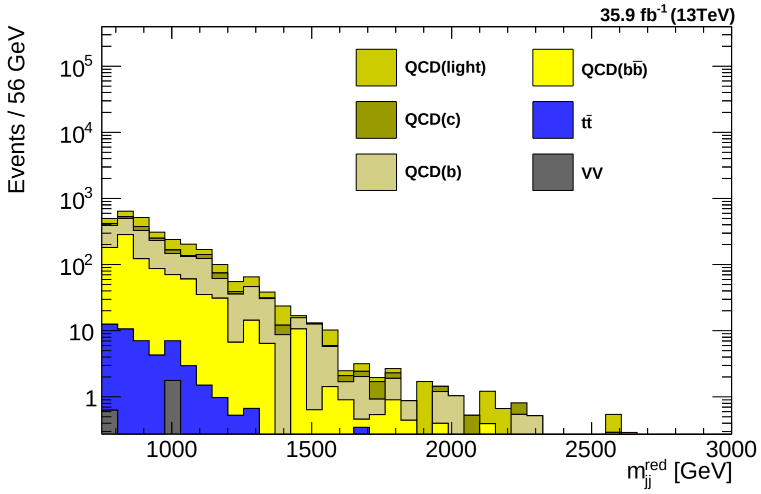

Figure 6.12: The reduced invariant di-jet mass distribution in simulated QCD, $\mathrm{t\bar{t}}$, and diboson events after the full event selection applied. The multijet background components for the different jet flavors are shown: events containing at least one jet with two B hadrons ($\mathrm{b\bar{b}}$) or a single one (b), events containing a jet having a charm hadron (c), and all other events (light).

therefore an estimation is made by reweighting every event in a control region with a technique called the “Alphabet” method. Both of these techniques are data-driven methods which exploit a number of sidebands that are defined with respect to the soft-drop mass and the double-b tagger discriminant of the leading p_T jet.

Mass (GeV)	≥ 2 AK8 jets + triggers	jet p_T, η	Tight jet ID	$\Delta\eta_{jj}$	Lepton Veto	τ_{21}	m_j	m_{jj}^{red}	double-b tag > 0.3	double-b tag > 0.8
750	0.610	0.368	0.368	0.331	0.330	0.149	0.049	0.039	0.027	0.015
800	0.758	0.541	0.541	0.503	0.502	0.237	0.080	0.079	0.057	0.032
900	0.903	0.772	0.771	0.716	0.715	0.371	0.125	0.124	0.092	0.051
1000	0.958	0.885	0.885	0.801	0.799	0.434	0.151	0.151	0.111	0.062
1200	0.988	0.962	0.961	0.843	0.842	0.499	0.178	0.178	0.129	0.068
1400	0.996	0.984	0.983	0.854	0.853	0.524	0.182	0.182	0.129	0.064
1600	0.998	0.993	0.993	0.858	0.857	0.532	0.186	0.186	0.128	0.061
1800	0.999	0.996	0.996	0.864	0.863	0.543	0.193	0.193	0.130	0.059
2000	1.000	0.998	0.998	0.861	0.860	0.541	0.190	0.190	0.123	0.054
2500	1.000	0.999	0.999	0.862	0.862	0.538	0.188	0.188	0.113	0.044
3000	1.000	1.000	0.999	0.865	0.865	0.530	0.186	0.186	0.102	0.034

Table 6.9: Efficiencies of various spin-2 bulk graviton masses after each selection selection requirement.

.

Mass (GeV)	≥ 2 AK8 jets + triggers	jet p_T, η	Tight jet ID	$\Delta\eta_{jj}$	Lepton Veto	τ_{21}	m_j	m_{jj}^{red}	double-b tag > 0.3	double-b tag > 0.8
750	0.432	0.248	0.247	0.213	0.213	0.093	0.029	0.024	0.016	0.009
800	0.547	0.367	0.367	0.327	0.326	0.152	0.051	0.050	0.036	0.021
900	0.693	0.552	0.552	0.487	0.485	0.245	0.083	0.083	0.061	0.033
1000	0.772	0.666	0.666	0.552	0.550	0.296	0.101	0.101	0.075	0.041
1200	0.859	0.792	0.792	0.585	0.584	0.335	0.116	0.116	0.084	0.044
1400	0.902	0.854	0.854	0.591	0.590	0.355	0.123	0.123	0.087	0.044
1600	0.928	0.890	0.889	0.592	0.591	0.358	0.124	0.124	0.086	0.041
1800	0.946	0.913	0.913	0.595	0.594	0.365	0.124	0.124	0.082	0.036
2000	0.957	0.931	0.931	0.598	0.598	0.365	0.127	0.127	0.081	0.036
2500	0.975	0.956	0.955	0.596	0.595	0.367	0.125	0.125	0.076	0.030
3000	0.981	0.966	0.965	0.589	0.589	0.357	0.123	0.123	0.068	0.022

Table 6.10: Efficiencies of various spin-0 radion masses after each selection selection requirement.

.

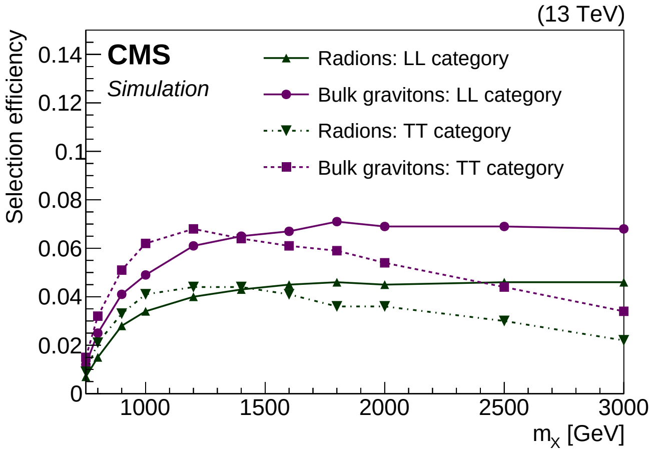

Figure 6.13: The signal selection efficiencies for the bulk graviton and radion models for different mass hypotheses of the resonances, shown for the LL and the TT signal event categories. Owing to the large sample size of the simulated events, the statistical uncertainties are negligible.

Considering these two variables, a set of regions is outlined in Figure 6.18, where the *pre-*

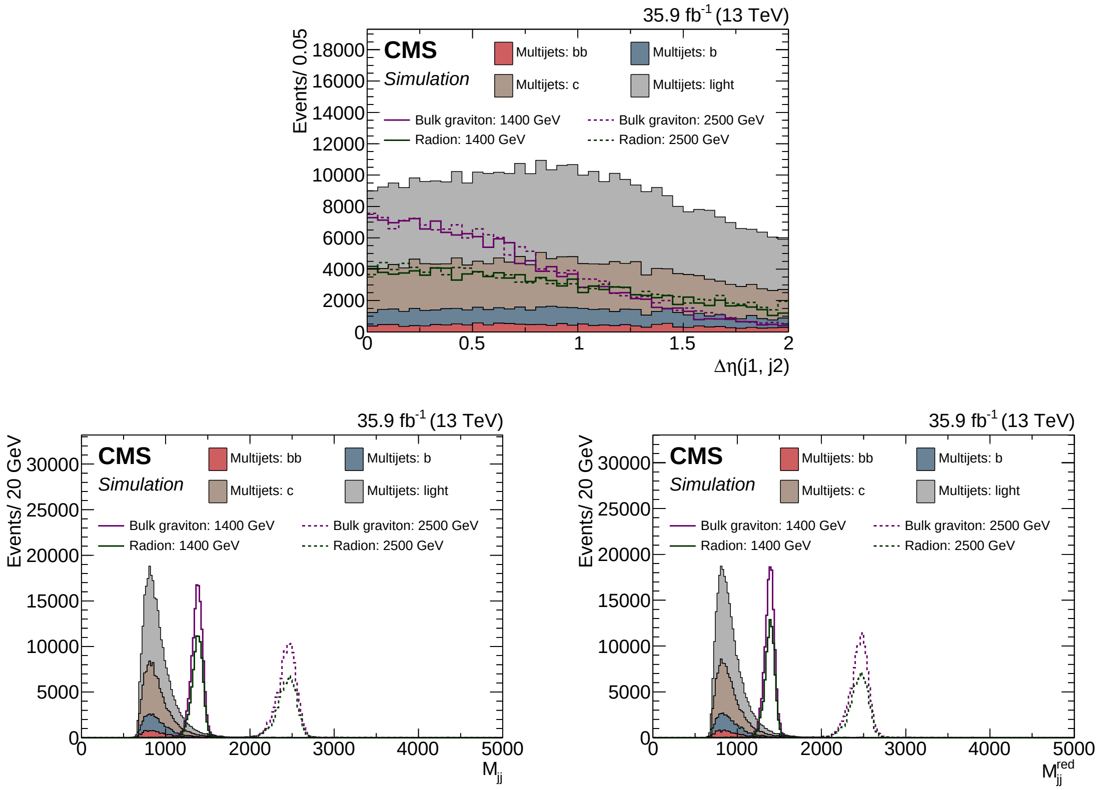

Figure 6.14: Comparison of simulated events after the full selection excluding b-tagging, $|\Delta\eta(\mathrm{j}_1, \mathrm{j}_2)|$ (upper), m_{jj} (lower left), and m_{jj}^{red} (lower right). A signal cross section of 20 pb is assumed for each signal mass point.

tag region is the superset of all the regions and is populated by events that pass every selection requirement except for the soft-drop mass and double-b tagger requirements on the leading jet. The *signal* region is the subset of those events where the soft-drop mass of the leading jet is inside the Higgs mass window, $105 - 135$ GeV, and the double-b tagger discriminator is greater than 0.3 or 0.8, for the LL and TT regions, respectively. The *anti-tag* region requires the leading jet double-b discriminator to be less than 0.3, with the requirement on the subleading jet either being between $0.3 - 0.8$ or greater than 0.8 for the LL or TT signal regions, respectively. The anti-tag regions are dominated by multijet background, as shown in Figure 6.19, and therefore can be used to predict the multijet background in the signal region. The four signal and anti-tag regions across the two categories are completely orthogonal to each other. The *sideband* regions consist of events in the pre-tag region, where the the soft-drop mass of the leading jet lies outside the Higgs mass window.

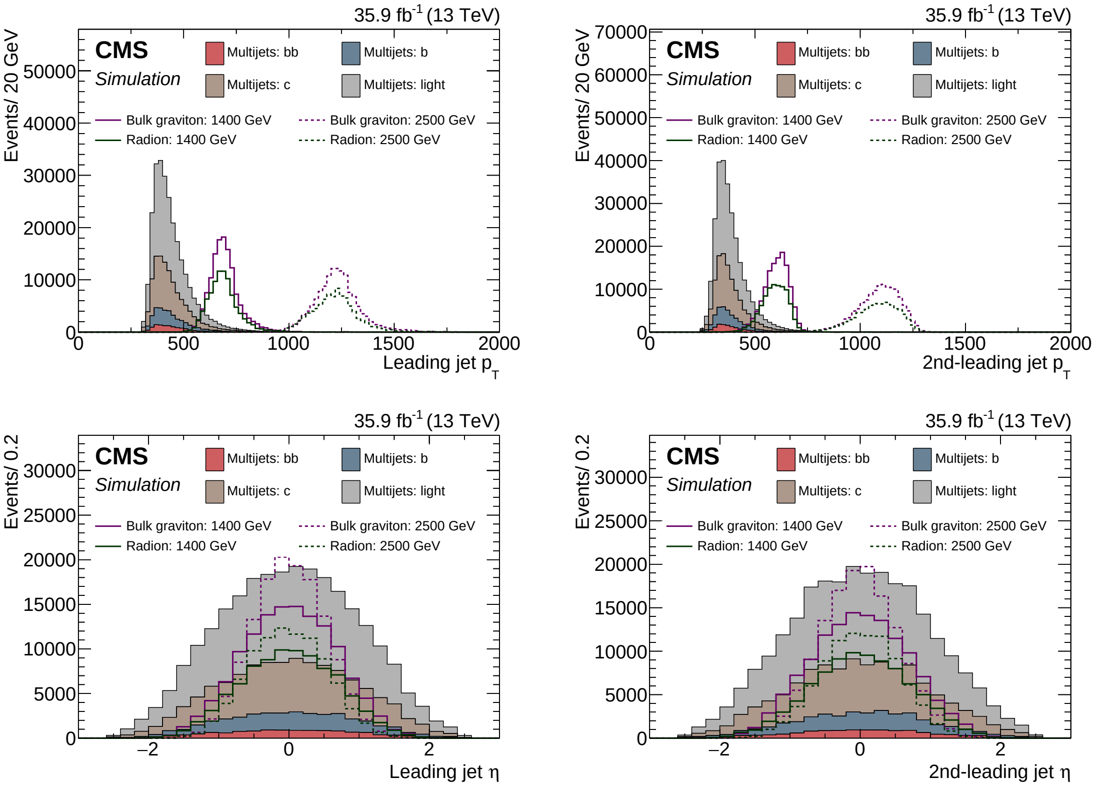

Figure 6.15: Comparison of simulated events after the full selection excluding b-tagging, for the p_T (upper) and η (lower) of leading (left) and sub-leading (right) Higgs jets. A signal cross section of 20 pb is assumed for each signal mass point.

Based on whether the leading jet passes or fails the double-b tagger discriminator threshold, the sideband region is divided into either “passing” or “failing’ categories,’ respectively. The definitions of the signal, the anti-tag, and the sideband regions are given in Table 6.11.

6.5.1 Alphabet Method

In the absence of correlation between the soft-drop mass and the double-b tagger discriminator, the background could be estimated by measuring the ratio of the number of events passing and failing the double-b tagger selection, $R_{p/f} \equiv N_{pass}/N_{fail}$ i.e. the “pass-fail ratio”, in a single jet mass sideband. The yield in the anti-tag region could then be scaled by $R_{p/f}$ to obtain an estimate of the background normalization in the signal region. This is a technique commonly referred to as the “ABCD” method. However, there is a small correlation between the double-b tagger discrim-

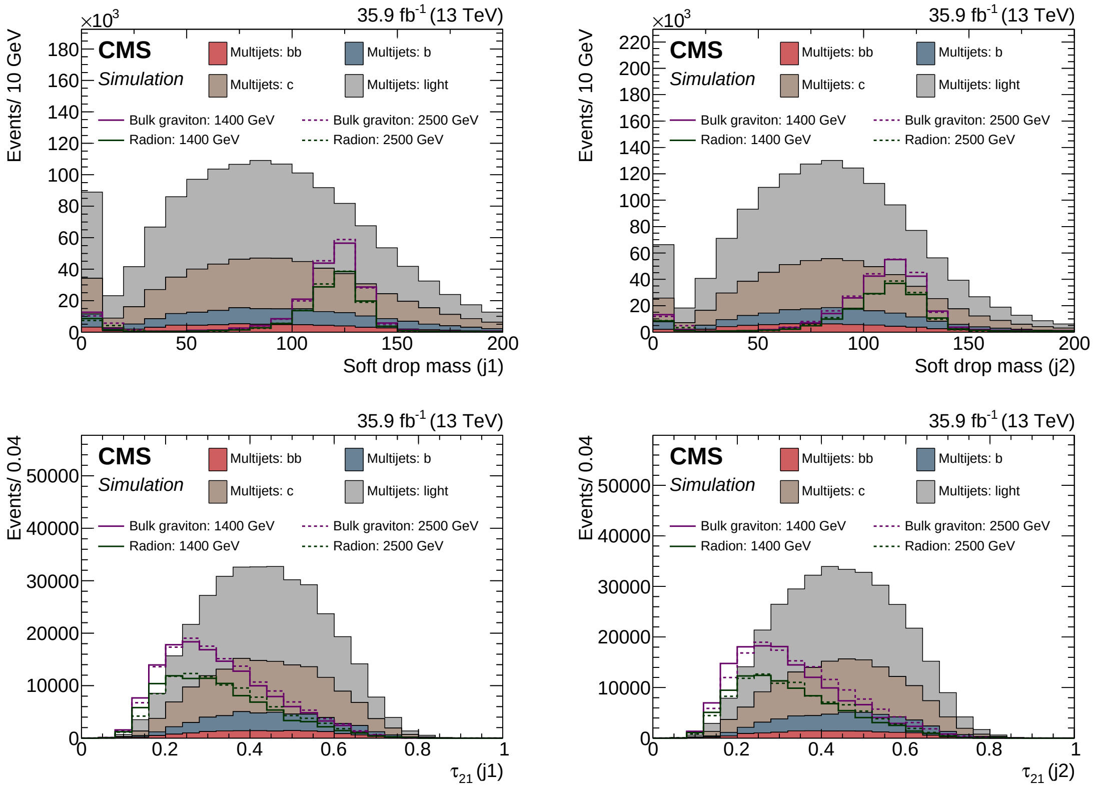

Figure 6.16: Comparison of simulated events after the full selection excluding b-tagging, for the soft-drop mass (upper) and the τ_{21} (lower) of the leading (left) and sub-leading (right) Higgs jets. A signal cross section of 20 pb is assumed for each signal mass point.

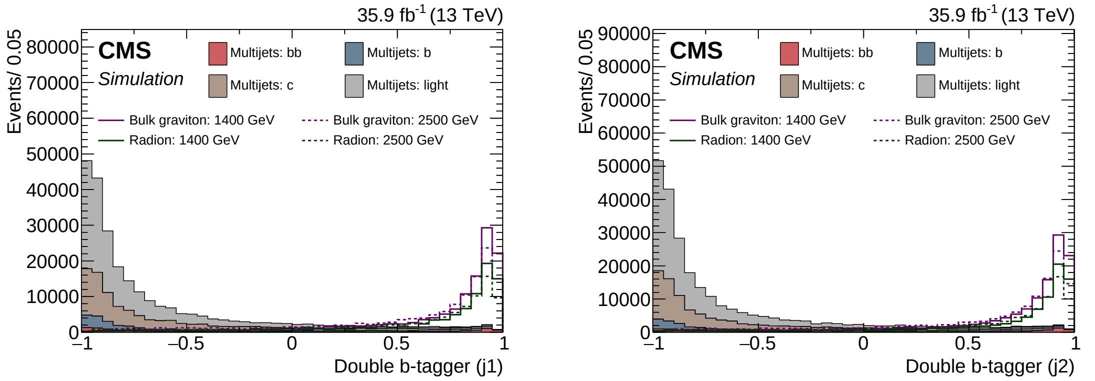

Figure 6.17: Comparison of simulated events after the full selection excluding b-tagging, for the double b-tagger discriminant of the leading (left) and sub-leading (right) Higgs jets. A signal cross section of 20 pb is assumed for each signal mass point.

inator and the soft-drop mass, which can be seen in Figure 6.20 where all events that fall in the

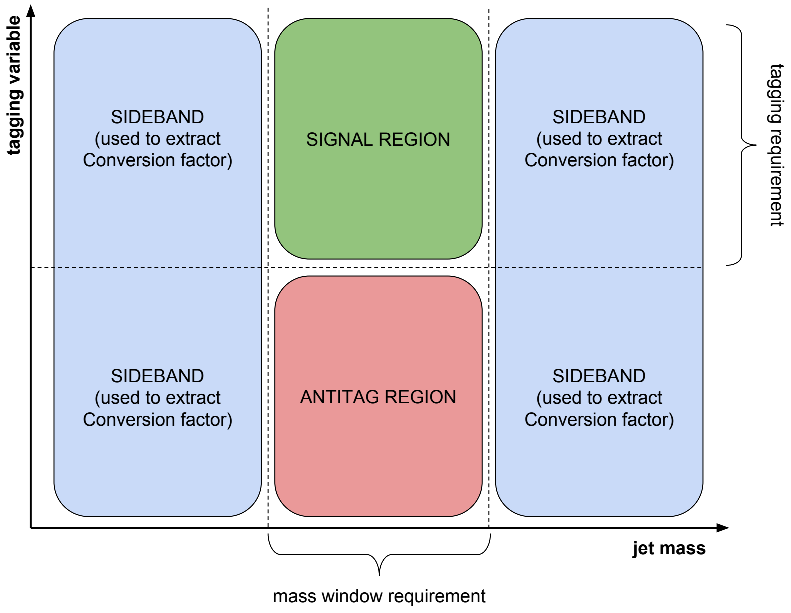
tagging variable
SIDEBAND
(used to extract
Conversion factor)
SIGNAL REGION
SIDEBAND
(used to extract
Conversion factor)
tagging requirement
SIDEBAND
(used to extract
Conversion factor)
ANTITAG REGION
SIDEBAND
(used to extract
Conversion factor)
jet mass
mass window requirement

Figure 6.18: Schematic representation of the regions used to perform the background estimate.

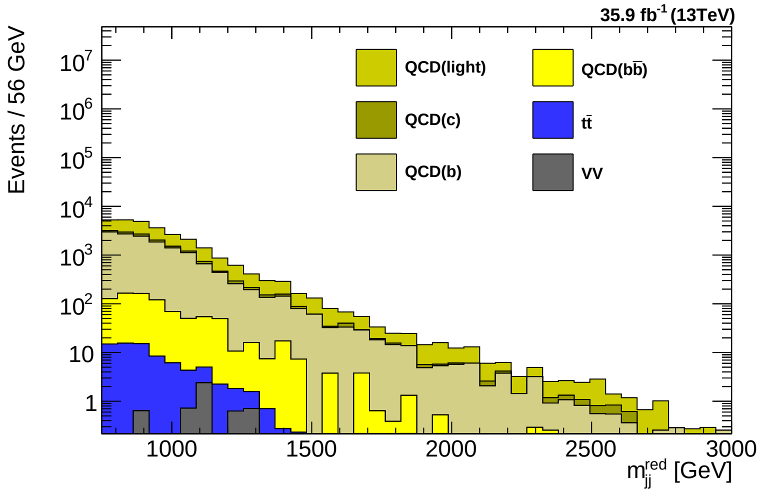

Figure 6.19: The reduced invariant di-jet mass distribution in simulated QCD, $t\bar{t}$, and diboson events in the combined LL and TT anti-tag region. The multijet background components for the different jet flavors are shown: events containing at least one jet with two B hadrons ($b\bar{b}$) or a single one (b), events containing a jet having a charm hadron (c), and all other events (light).

pre-tag region are plotted, and therefore $R_{p/f}$ is measured as a function of the soft-drop mass of the leading p_T jet.

Event Category	Jet	Soft-drop mass (GeV)	Double-b tagger discriminator
Signal (LL)	Leading	$105 - 135$	> 0.3, but not both > 0.8
	Sub-leading		
Signal (TT)	Leading		> 0.8
	Sub-leading		
Antitag (LL)	Leading	$105 - 135$	< 0.3
	Sub-leading		$0.3 - 0.8$
Antitag (TT)	Leading		< 0.3
	Sub-leading		> 0.8
Sideband (LL, passing)	Leading	< 105 or > 135	> 0.3, but not both > 0.8
	Sub-leading	$105 - 135$	
Sideband (TT, passing)	Leading	< 105 or > 135	> 0.8
	Sub-leading	$105 - 135$	
Sideband (LL, failing)	Leading	< 105 or > 135	< 0.3
	Sub-leading	$105 - 135$	$0.3 - 0.8$
Sideband (TT, failing)	Leading	< 105 or > 135	< 0.3
	Sub-leading	$105 - 135$	> 0.8

Table 6.11: Definition of the signal, the anti-tag, and the sideband regions used for the background estimation.

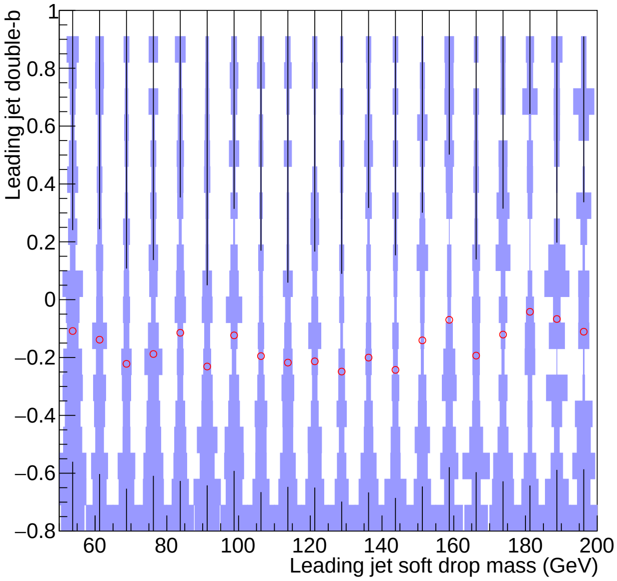

Figure 6.20: Distribution in the pre-tag region of the leading jet double-b tagger discriminator vs soft-drop mass in QCD simulation. The red points represent the 50% quantile and show that there is a slight dependence of the double-b tagger on jet mass.

The $R_{p/f}$ for the LL region is measured using the ratio of the number of events in the "LL, passing" and "LL, failing" sideband regions, as defined in Table 6.11. Likewise, the $R_{p/f}$ for the TT region is measured using the ratio of the number of events in the "TT, passing" and "TT, failing" sideband regions. The variation of $R_{p/f}$ as a function of the leading jet mass in each soft-drop mass sideband is fitted with a quadratic function and the fit is interpolated to the Higgs mass window of the leading jet mass. An alternative fit using a third order polynomial was found to give the same interpolated value of $R_{p/f}$ in the Higgs jet mass window. Every event in the anti-tag region is scaled by the pass-fail ratio evaluated for the leading jet mass of that event, to obtain the background prediction in the signal region.

Since the background prediction in the signal region is obtained by scaling the events in the anti-tag region, the Alphabet method assumes that the shapes of the m_{jj}^{red} distributions in the pass and fail regions are the same. This is verified in QCD simulation and the m_{jj}^{red} distributions in the signal region and anti-tag region for both LL and TT categories can be seen in Figure 6.21. As a further check, the m_{jj}^{red} distributions in the pass and fail regions of each sideband are compared in data and shown to have similar shapes, which can be seen in Figures 6.22 and 6.23.

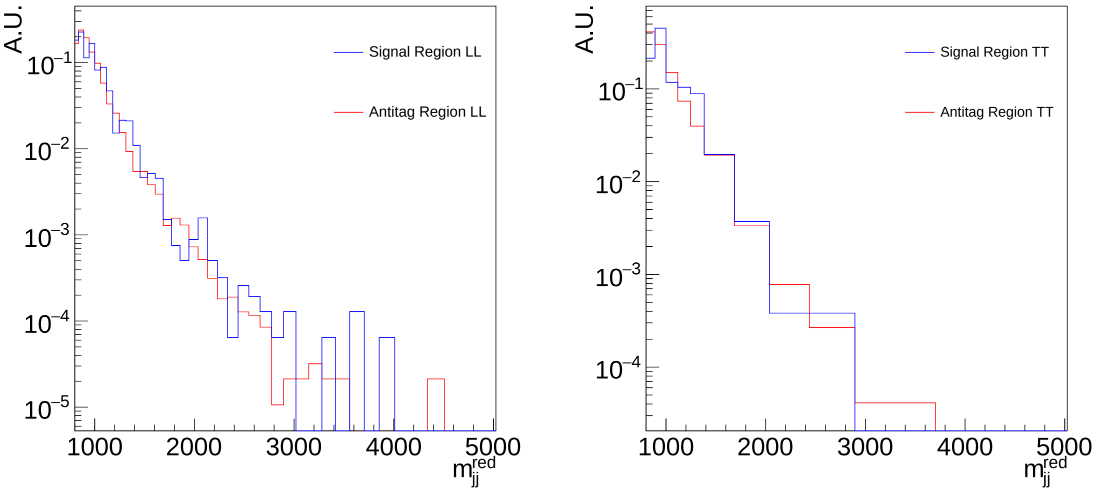

Figure 6.21: Distributions of m_{jj}^{red} in the signal and anti-tag regions for the LL category (left) and the TT category (right). Events are from QCD simulation and the distributions are normalized to unity to show that the distributions have similar shapes.

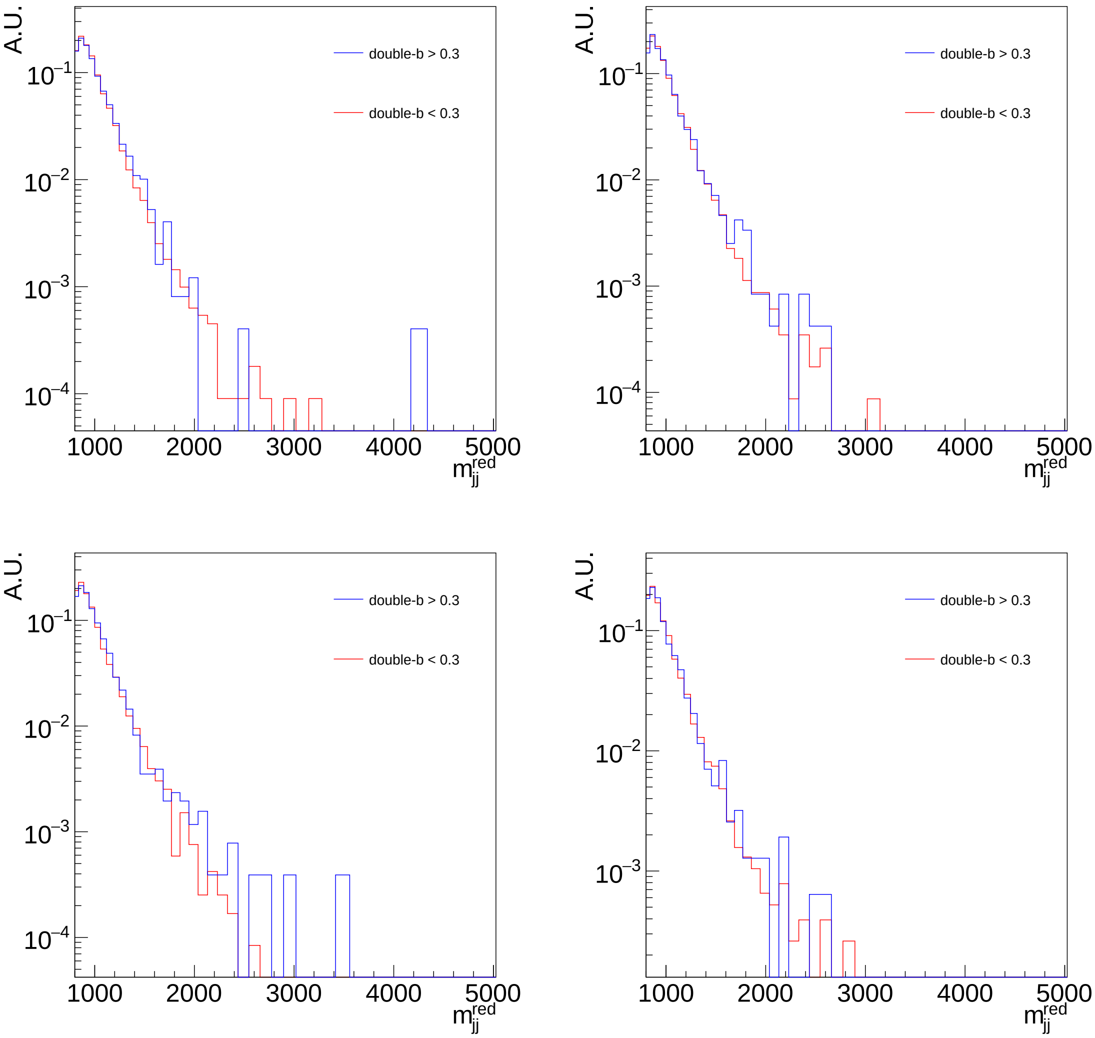

Figure 6.22: Distributions of m_{jj}^{red} in data normalized to unity in the $50-65$ GeV sideband (top left), the $65-80$ GeV sideband (top right), the $80-95$ GeV sideband (bottom left), and the $95-105$ GeV sideband (bottom right).

6.5.1.1 Results in Simulation

Prior to unblinding the data, the validity of the Alphabet method was tested on simulation. Figure 6.24 shows the quadratic fit in the mass sidebands of $R_{p/f}$ for both the LL and TT regions. Note that the pass-fail ratios in the Higgs mass window are not included in the fit and the true value of the pass-fail ratio in the Higgs mass window is shown to agree within uncertainties to the $R_{p/f}$ prediction. The estimated background after scaling the anti-tag region by the predicted $R_{p/f}$

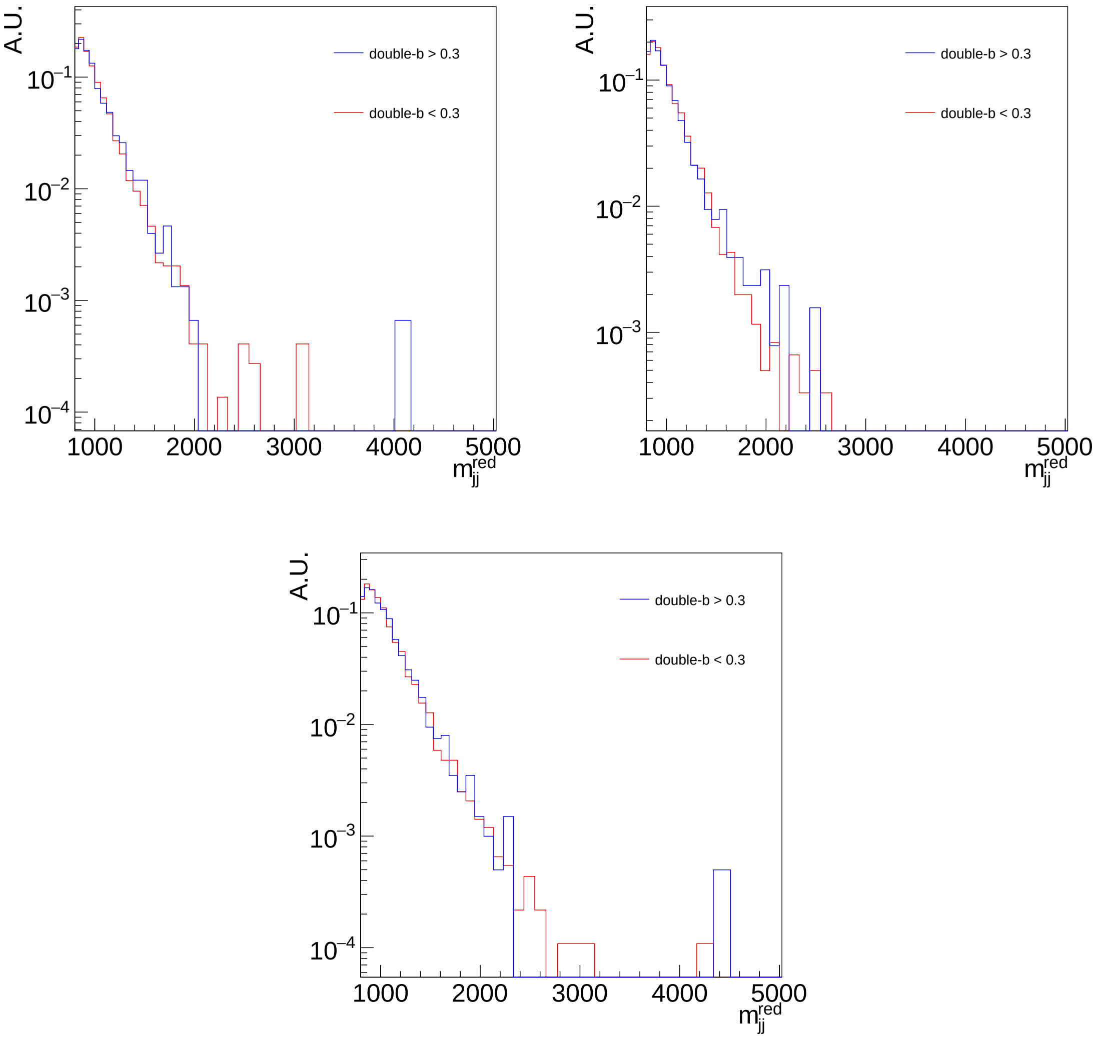

Figure 6.23: Distributions of m_{jj}^{red} in data normalized to unity in the $135 - 150$ GeV sideband (top left), the $150 - 165$ GeV sideband (top right), and the $165 - 200$ GeV sideband (bottom).

is compared to the true background in the signal region in Figure 6.25.Two systematic uncertainties arise naturally from this estimate. The dominant error comes from the statistical uncertainty in the $R_{p/f}$ fit to the mass sideband regions, which is shown as a dashed line enveloping the fit in Figure 6.24. This error can be treated as fully correlated between all mass bins when setting limits. A smaller source of error is from propagating the statistical uncertainty in the anti-tag region to the signal region and is uncorrelated between bins.

To further test this method, a check was performed to verify that the estimate is free of bias

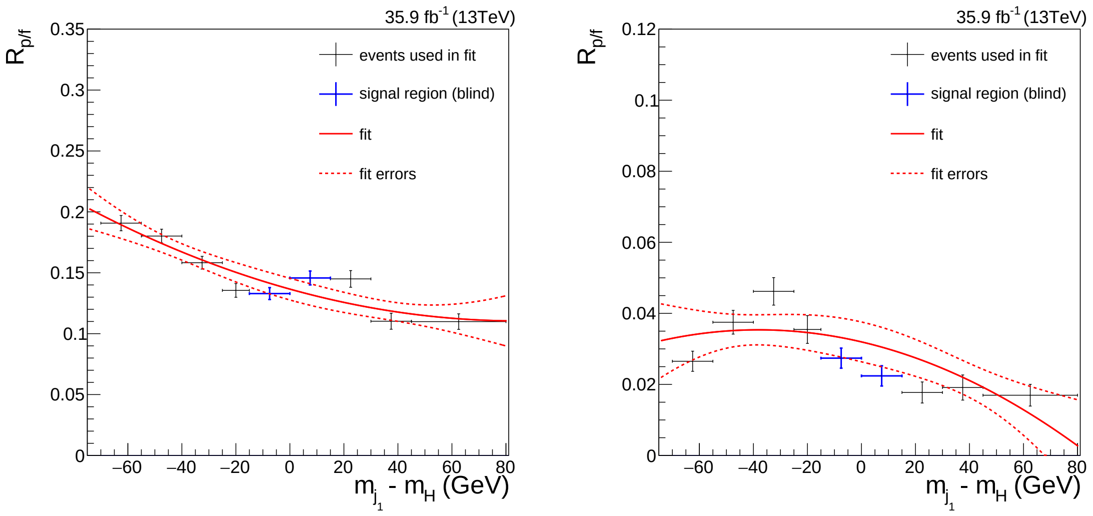

Figure 6.24: The pass-fail ratio in simulation of the leading p_T jet for the LL (left) and TT (right) signal region categories as a function of the difference between the soft-drop mass of the leading jet and the Higgs boson mass. The measured ratio in different bins of $m_{j_1} - m_H$ is used in the fit (red solid line), except in the region around $m_{j_1} - m_H = 0$, which corresponds to the signal region (blue markers).

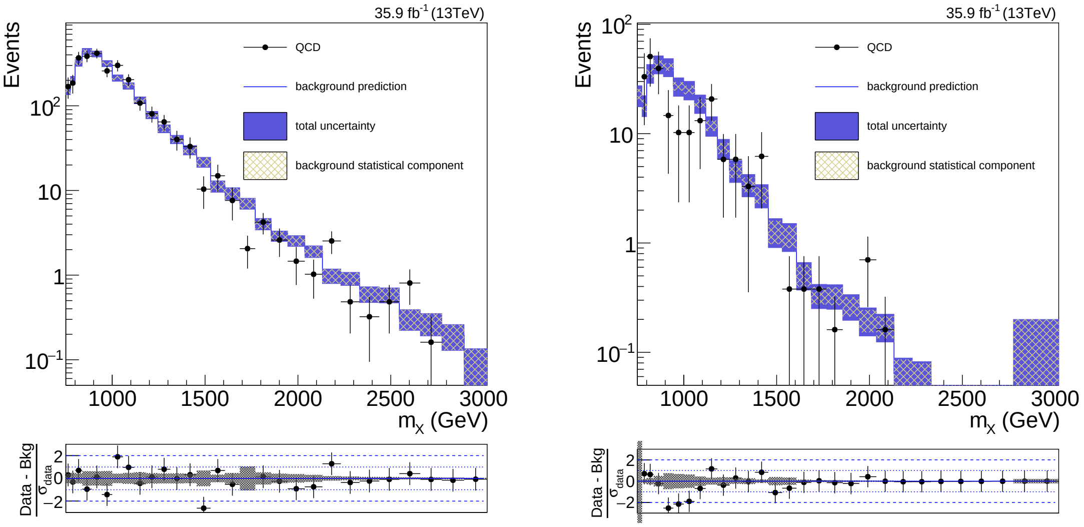

Figure 6.25: The reduced mass distributions in simulation for the LL (left) and TT (right) signal region categories. The point with bars show the actual events in the signal region, while the histogram shows the estimated background and associated uncertainty. The difference between the events and the predicted background, divided by the statistical uncertainty is shown in the lower panels.

when a signal is introduced. This was done by injecting a bulk graviton signal sample with bulk graviton mass at 1800 GeV and the cross section scaled to 10 fb into the QCD MC. The Alphabet method was then performed and the results can be seen in Figure 6.26. The background estimate performs well, with the addition of this signal having no significant effect on the background estimate.

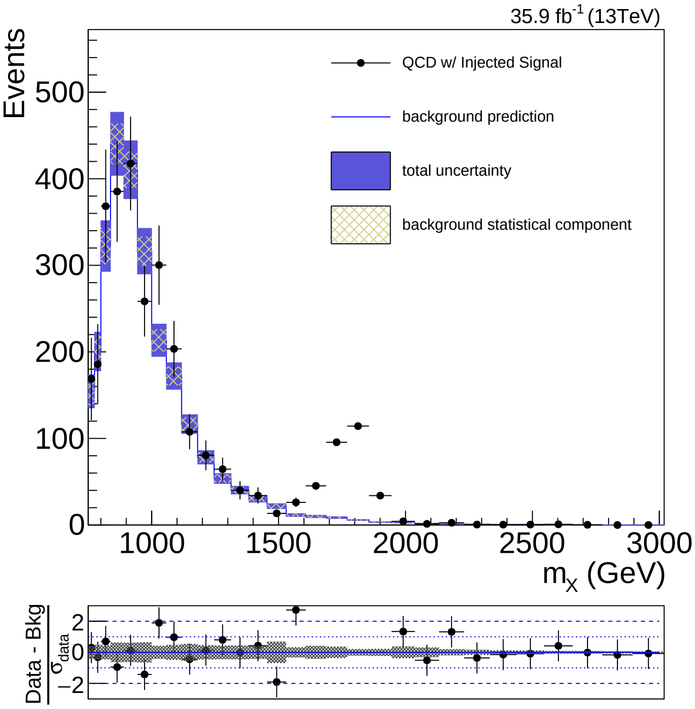

Figure 6.26: Reconstruction of QCD background in the presence of a bulk graviton signal with a cross section of 10 fb and bulk graviton mass of 1800 GeV. The background estimate is not biased by the signal.

To ensure that the double-b tagger discriminator does not have any jet p_T or equivalently m_{jj}^{red} dependence that is not accounted for since the pass-fail ratio is only measured as function of jet mass, the dependence of the estimated $R_{p/f}$ in different di-jet mass bins was measured in simulation. This is shown in Figure 6.27, where the Alphabet method was performed in the LL category separately on events in three different m_{jj}^{red} regions: $750 < m_{jj}^{red} < 900$ GeV, $900 < m_{jj}^{red} < 1300$ GeV, and $m_{jj}^{red} > 1300$ GeV.

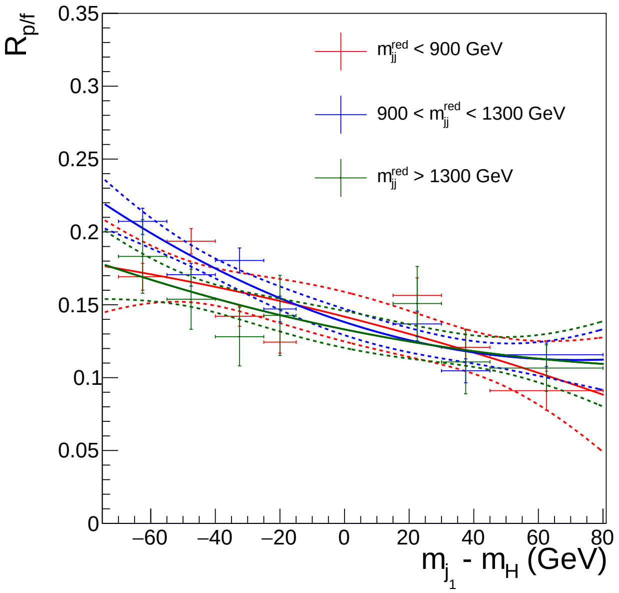

Figure 6.27: The pass-fail ratio in the LL category from events in three different m_{jj}^{red} bins. The predicted pass-fail ratio in the Higgs mass window between all three cases agree with their uncertainties.

6.5.1.2 Closure Test in Data

As a second test of the dependence of the double-b tagger discriminator on jet p_T, the pass-fail ratio as a function of m_{jj}^{red} was explicitly measured in data for the TT region. The ratio of events in the anti-tag region to events predicted in the signal region by the pass-fail ratio is shown, binned in di-jet mass, in Figure 6.28. The plot illustrates that there is no dependence on the pass-fail ratio as a function of di-jet mass.

As a further test of closure, the Alphabet method was run in data in a control region similar to the signal region except that the sub-leading jet is constrained to fail the double-b requirement, double-b discriminator < 0.3. The Alphabet method is able to accurately predict the pass-fail ratios in the Higgs mass window, as well as the m_{jj}^{red} distribution in the control region. Results are shown in Figure 6.29 for two values of the cut on the leading jet double-b: 0.8 and 0.3.

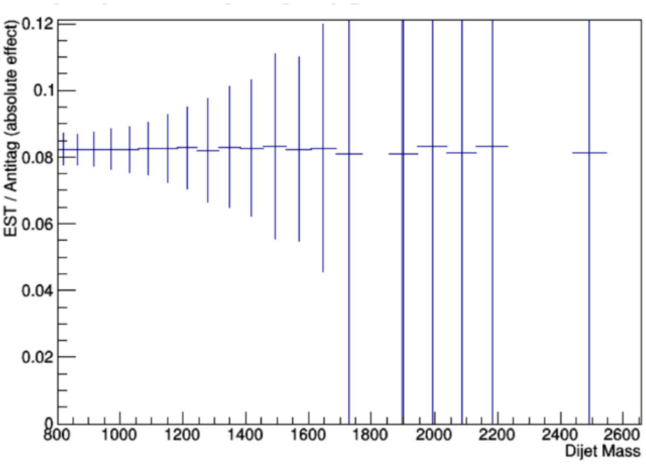

Figure 6.28: The ratio of events in the anti-tag region to events predicted in the signal region by the transfer factor is shown, binned in m_{jj}^{red}. The plot illustrates that there is no dependence on the pass-fail ratio as a function of di-jet mass.

6.5.2 Alphabet Assisted Bump Hunt Method

The AABH method predicts the background where $m_{jj}^{red} > 1100$ GeV and improves upon the Alphabet method by modeling the background shape as a monotonically falling function. This smooth background modeling helps reduce uncertainties in the background estimation from local statistical fluctuations in m_{jj}^{red}, therefore improving the signal sensitivity. The AABH method simultaneously fits a parametric model to both the anti-tag and signal region while the normalization between the two regions is constrained by the pass-fail ratio that is obtained from the sidebands in the Alphabet method. Therefore, the background is modeled as

$$B(m_{jj}^{red}) = R_{p/f} \times A(m_{jj}^{red}), \tag{6.4}$$

where $B(m_{jj}^{red})$ is the background model in the signal region and $A(m_{jj}^{red})$ is the model of anti-tag region. To account for a slight $R_{p/f}$ dependence on m_{jj}^{red} at high m_{jj}^{red} values (see Figure 6.28), $R_{p/f}$ is allowed to vary linearly in m_{jj}^{red} by multiplying it by the factor $(1 + lin * m_{jj}^{red})$. The signal normalization is unconstrained in the fit, while the uncertainties in the parameters of the functions used to model the background and $R_{p/f}$ are treated as nuisance parameters.

Three models were considered to parameterize the background shape in the signal and anti-

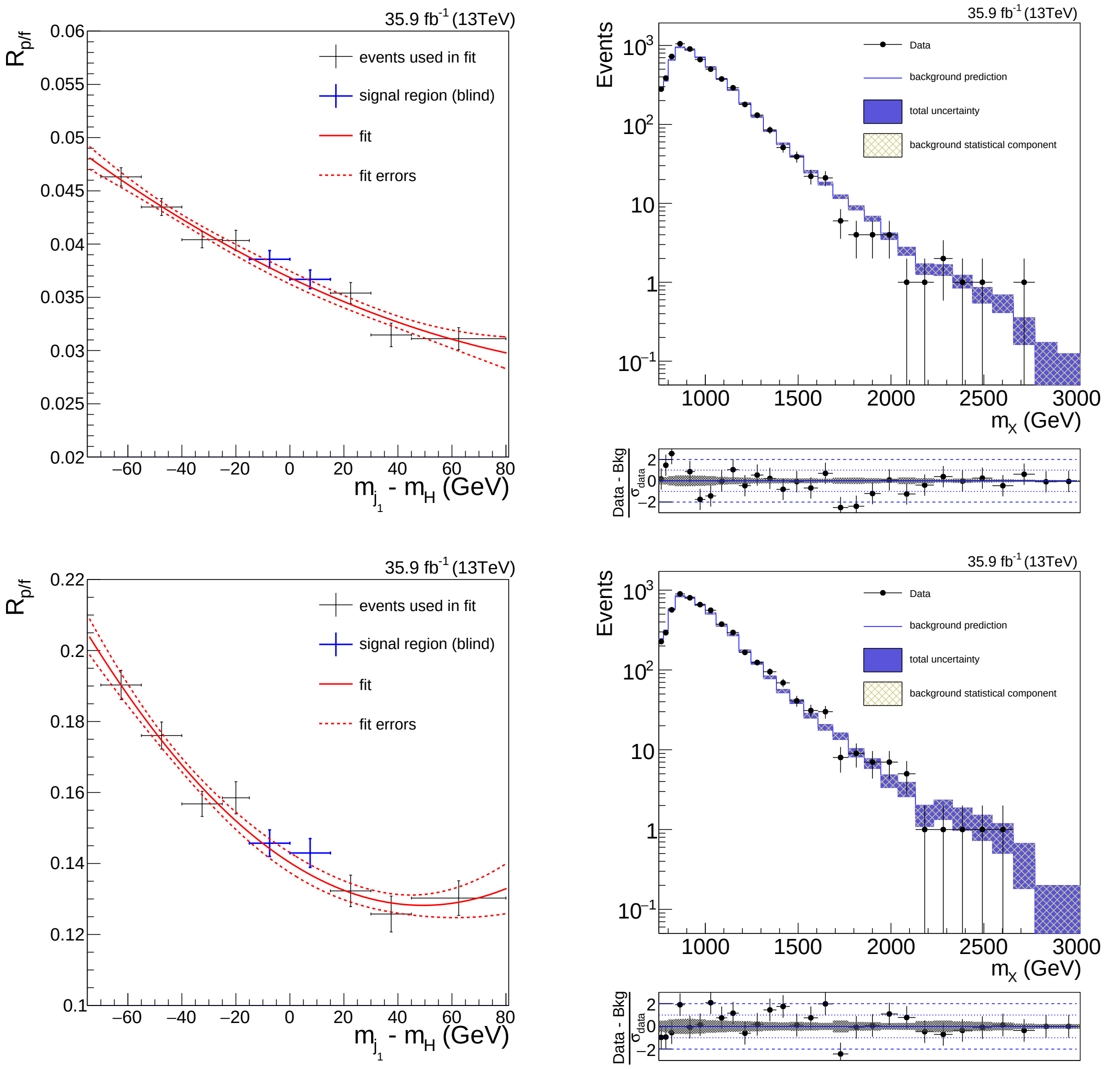

Figure 6.29: (left) Fits in the mass sideband regions for the pass-fail ratio $R_{p/f}$ for (from top to bottom) the tight and loose working point. (right) Application of those fits to the anti-tag region to estimate the background in the control regions, compared with the true background (black markers).

tag region:

- Exponential (1-parameter): $Ne^{-am_{jj}^{red}}$
- Leveled exponential (2-parameter): $Ne^{\frac{-am_{jj}^{red}}{1+abm_{jj}^{red}}}$
- Quadratic levelled exponential (3-parameter): $Ne^{\frac{-am_{jj}^{red}}{1+abm_{jj}^{red}}-\frac{c(m_{jj}^{red})^2}{1+bc(m_{jj}^{red})^2}}$.

To determine which function to use a Fisher F-test [87] was employed. An F-test is a way to compare statistical models that have been fitted to a data set, in order to identify the model that best fits the data. It compares variances between the data and the model for two different model functions and checks if there is a real variance reduction on using an extra parameter. The p-values tell the probability that n parameters describe the data significantly worse than $n+1$ parameters. If the p-value is below 0.05 it means roughly that at 95% confidence level (CL) we need $(n+1)$ parameters. The results of the F-test indicate that a 2-parameter function is optimal for modeling the background. Therefore, the final models used are

$$N * e^{-m_{jj}^{red} * bgp2/(1+m_{jj}^{red} * bgp1 * bgp2)}, \tag{6.5}$$

$$N * R_{p/f} * (1 + lin * m_{jj}^{red}) e^{-m_{jj}^{red} * bgp2/(1+m_{jj}^{red} * bgp1 * bgp2)}, \tag{6.6}$$

where Eq 6.5 and Eq 6.6 parameterize the signal and anti-tag regions, respectively. The parameters N, $bgp1$, and $bgp2$ are shared between the two fit functions.

6.5.2.1 Closure Tests

The first validation of this method was done using QCD MC, in both the LL and TT regions. Plots of the signal and anti-tag regions with the AABH fit applied are shown in Figs. 6.30 and 6.31. The fits are shown with and without the linear constraint on the pass-fail ratio $R_{p/f}$ and these are consistent, showing that $R_{p/f}$ has very little dependence on m_{jj}^{red}. A goodness of fit (GOF) test was done using the data to confirm that the leveled exponential models the background well. The signal strength was set to zero for this fit and a p-value of 0.97 was obtained showing that the model describes the data well.

A bias study was conducted for the AABH method by injecting a certain number of signal events, n_i, for three different resonance mass hypothesis: 1600 GeV, 2000 GeV, and 2500 GeV. The number of events injected for each hypotheses was zero events, two events, corresponding to a $\sim 5\sigma$ excess at $m_X = 1.2$ TeV, and 5 events, corresponding to a $\sim 10\sigma$ excess at $m_X = 2$ TeV. A

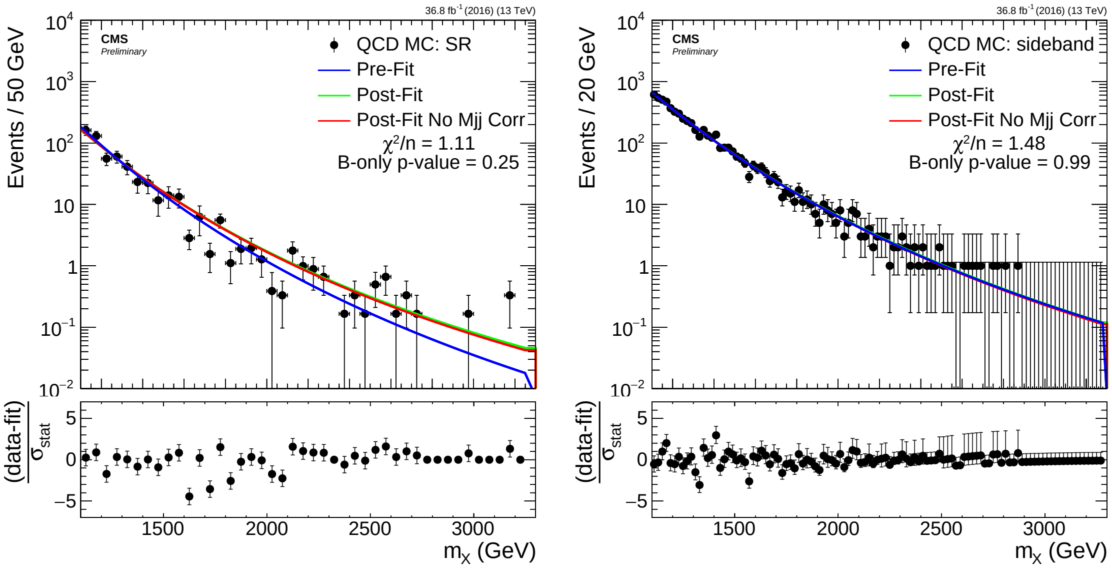

Figure 6.30: Fits in the LL region in the signal (left) and anti-tag (right) regions from QCD as used by the AABH approach. The fits before (pre-fit) and after the likelihood fit are shown. The pre-fit curve is obtained using only the anti-tag region.

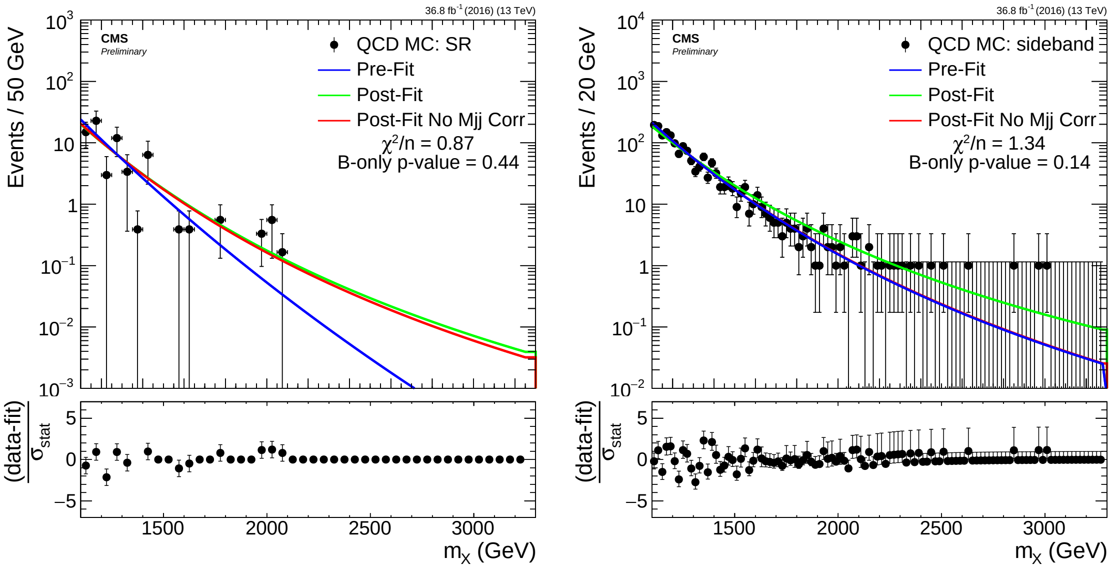

Figure 6.31: Fits in the TT region in the signal (left) and anti-tag (right) regions from QCD as used by the AABH approach. The fits before (pre-fit) and after the likelihood fit are shown. The pre-fit curve is obtained using only the anti-tag region.

maximum likelihood fit was then performed to extract the signal strength and for each combination of number of injected events and mass hypothesis the observed signal strength matched.

6.6 Signal Modelling

For $m_X > 1100$ GeV, the m_{jj}^{red} distributions for the signals are modeled using the sum of a Crystal Ball function and a Gaussian, where the two function are constrained to have the same mean value. The same modeling is used in the LL and TT categories, with parameters for the Gaussian and the Crystal Ball function differing as shown in Figure 6.32.

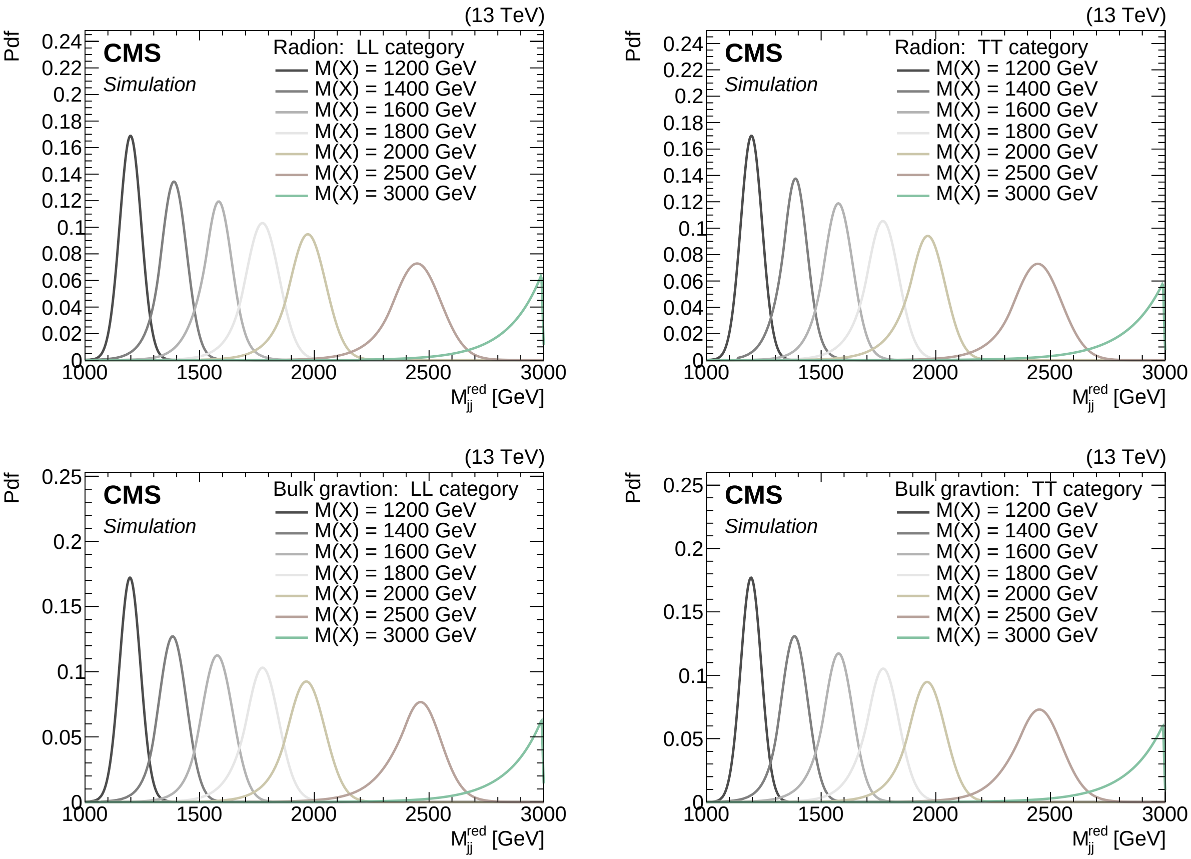

Figure 6.32: Signal modeling for the radion (upper row) and bulk graviton (lower row) signal using the sum of a Gaussian and Crystal Ball functions. Shown are the probablity density functions (Pdfs) for the LL (left) and TT (right) categories.

6.7 Systematic Uncertainties

The following sources of systematic uncertainty only affect the expected signal yields without causing any significant change in the signal shape. The background is unaffected by them because it is computed entirely from data, which brings different uncertainties that will be described following the signal uncertainties. All of the systematic uncertainties are summarized in Table 6.12.

- **Luminosity:** The luminosity during 2016 data taking was measured with an overall uncertainty of 2.5% [88].

- **Pileup:** Simulated samples are reweighted so that their pileup distribution matches the pileup distribution in data. The uncertainty on this reweighting is estimated by varying the minimum bias cross section by ±4.6%, resulting in an uncertainty of 2%.

- **Parton Distribution Functions:** The impact on the signal acceptance due to the uncertainties in the parton distribution functions (PDFs) is estimated following the PDF4LHC procedure [89], where three different PDF sets are used: CT14 [90], MMHT2014 [91], and NNPDF3.0 [92]. The PDF uncertainties are found to be between $0.1 - 2\%$ depending on the resonance mass.

- **Trigger Efficiency:** To correct the difference in trigger efficiency observed between the data and simulation a scale factor that is a function of m_{jj}^{red} and $|\Delta\eta(j_1, j_2)|$ (see Section 6.3) is applied. For $m_{jj}^{red} > 1100$ GeV, the efficiency in data and MC is above 99% and the uncertainty in the scale factor is negligible. For $m_{jj}^{red} < 1100$ GeV, the uncertainty in the scale factor is between 1% and 15%.

- **Double-b Tagging:** The efficiency of the double-b tagger is measured in an enriched gluon splitting to $\mathrm{b\bar{b}}$ data sample and signal yields are corrected to match this efficiency [7]. The corresponding uncertainty is $2 - 5\%$ depending on the double-b tagger requirement.

- τ_{21} **Scale Factor:** The data to simulation scale factor for the τ_{21} selection is measured using a semi-leptonic $\mathrm{t\bar{t}}$ sample of boosted hadronic W bosons and is found to be $+30/-26\%$ for the two Higgs jets combined. An additional correction factor is applied to account for the difference in the jet shower profile of $\mathrm{W \rightarrow q\bar{q}}$ and $\mathrm{H \rightarrow b\bar{b}}$ decays. This correction is calculated by taking the ratio of the Higgs-tagging efficiency to the W-tagging efficiency calculated in different shower generators, PYTHIA 8 and HERWIG++. The efficiencies are measured using different mass bulk gravition MC samples, where the bulk graviton either decays to a pair of Higgs bosons or a pair of W bosons. A double ratio of efficiencies, $R_{\text{HERWIG}}/R_{\text{PYTHIA}}$, is then calculated to provide the correction factor. The double ratio provides an estimate of how different showering algorithms handle the difference between hadronically decaying Higgs and W bosons. The corresponding uncertainty from the correction factor is in the range $7-20\%$ depending on the resonance mass.

- **Higgs Mass Tagging:** The difference in modeling in simulation compared to data of the jet mass scale and resolution is measured in a similar manner as the τ_{21} scale factor, using a semi-leptonic $\mathrm{t\bar{t}}$ sample of boosted hadronic W bosons. The scale factor for both is one, but a 1% and 20% uncertainty per jet is associated with each scale factor for the jet mass scale and resolution, respectively.
- **Jet Energy Scale:** An uncertainty on the jet energy scale is applied to the signal acceptance, according to the CMS JetMET POG. The uncertainty causes a 2% fluctuation to the signal yield.
- **Jet Energy Resolution:** An uncertainty on the jet energy resolution is applied to the signal acceptance, according to the CMS JetMET POG. The uncertainty causes a 2% fluctuation to the signal yield.

The remaining uncertainties impact the multijet background estimate and depend on which background estimation method is used.

- **Alphabet:** For $m_{jj}^{red} < 1100$ GeV, the main source of uncertainty is due to the statistical uncertainty in the fit to the $R_{p/f}$ ratio performed in the leading Higgs jet mass sidebands. This uncertainty is fully correlated between all m_{jj}^{red} bins of a particular estimate and amounts to $2.6-6.8\%$. An additional statistical uncertainty in the anti-tag region is propagated to the signal region when the estimate is made. This uncertainty is uncorrelated from bin to bin. The Barlow-Beeston Lite method [93] is used to treat the bin-by-bin statistical uncertainty. These uncertainties affect both the shape of the background and the total background yield.

- **AABH:** For $m_{jj}^{red} > 1100$ GeV, the uncertainty from the AABH background estimate is simply the uncertainty in the simultaneous fit of the anti-tag and signal regions. The dependence of $R_{p/f}$ on m_{jj}^{red} is accounted for by providing a Gaussian constraint on this dependence. However, this was found to be negligible.

Source	Uncertainty(%)
Signal Yield	
Trigger efficiency	$1-15$
H jet energy scale	2
H jet energy resolution	2
H jet mass scale	1
H jet mass resolution	20
H jet τ_{21} selection	$+30/-26$
H-tagging correction factor	$7-20$
Double-b tagger	$2-5$
Pileup modeling	2
PDFs	$0.1-2$
Luminosity	2.5
Background Yield	
$R_{p/f}$ fit	$2.6-6.8$

Table 6.12: Summary of systematic uncertainties in the signal and background yields.

6.8 Results

The quadratic fit in the leading jet p_T sidebands of the pass-fail ratio for the LL and TT regions in data is shown in Figure 6.33. The predicted $R_{p/f}$ has good agreement with the measured $R_{p/f}$ in the Higgs mass window. The background prediction from the Alphabet method for both regions, along with the number of observed events in the signal region is shown in Figure 6.34. A representative signal of a bulk graviton of mass 1000 GeV is overlaid for comparison. Figures 6.35 and 6.36 present the results of the AABH method's simultaneous fits to both the anti-tag and signal regions in both the LL and TT categories. In Figure 6.36 the expected distribution from bulk gravitons of masses 1600 and 2500 GeV are overlaid in the signal regions. The fit to the background in the AABH method is extended just beyond the last observed event in the four fitted regions which occurs in the anti-tag region in the LL category, which is at 2838 GeV. As the parametric model is only reliable within the range of observed events, the likelihood is only evaluated up to $m_{jj}^{red} = 3000$ GeV. This results in a truncation of the signal distribution for resonances having m_X of 2800 GeV and above, with the signal efficiency losses increasing to 30% for $m_X = 3000$ GeV, as shown in Figure 6.32.

Over the whole mass range searched, 750$-$3000 GeV, the data and the estimated backgrounds agree within uncertainties and therefore the results are interpreted in terms of upper limits on the product of the production cross sections and the branching fractions, $\sigma(\mathrm{pp} \to \mathrm{X})B(\mathrm{X} \to \mathrm{HH} \to \mathrm{b\bar{b}b\bar{b}})$, for bulk graviton and radion of various mass hypothesis.

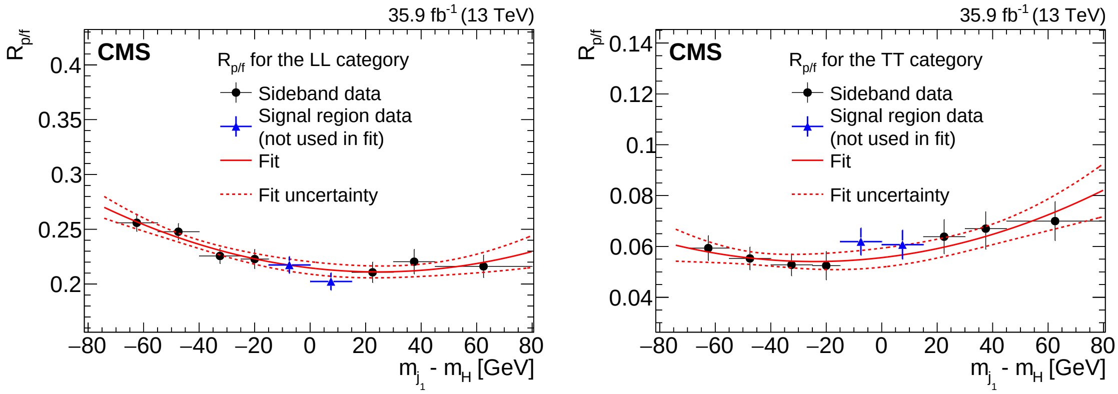

Figure 6.33: The pass-fail ratio $R_{p/f}$ of the leading p_T jet for the LL (left) and TT (right) signal region categories as a function of the difference between the soft-drop mass of the leading jet and the Higgs boson mass, $m_{j1} - m_H$. The measured ratio in different bins of $m_{j_1} - m_H$ is used in the fit (red solid line), except in the region around $m_{j_1} - m_H = 0$, which corresponds to the signal region (blue triangular markers). The horizontal bars on the data points indicate the bin widths.

The asymptotic approximation of the modified frequentist approach for confidence levels, taking the profile likelihood as a test statistic [94, 95, 96], is used to compute the limit at 95% confidence. The systematic uncertainties are represented as nuisance parameters in the likelihood and profiled by maximizing the likelihood with respect to the nuisances and obtaining them in terms

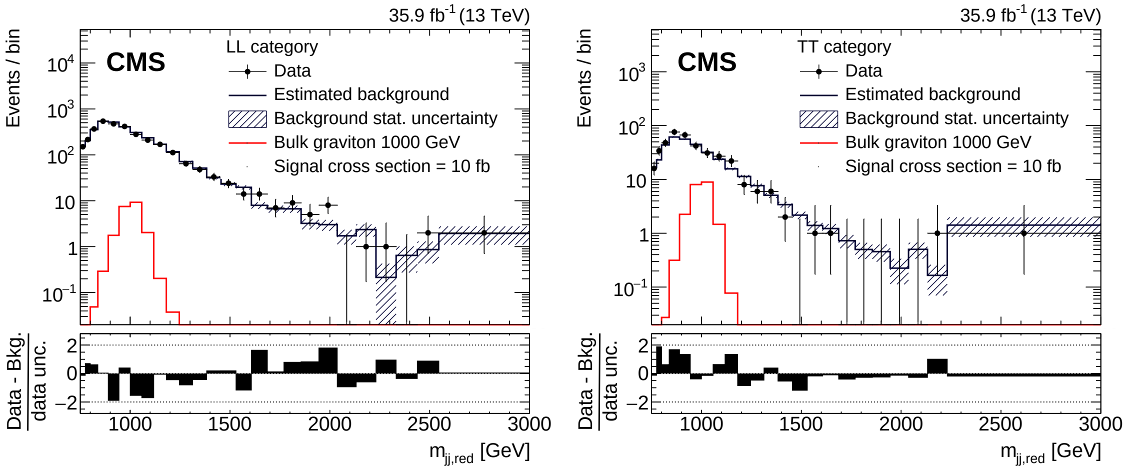

Figure 6.34: The reduced mass distributions m_{jj}^{red} for the LL (left) and TT (right) signal region categories. The points with bars show data, the histogram with a shaded band shows estimated background and associated uncertainty. The signal predictions for a bulk graviton of mass 1000 GeV, are overlaid for comparison, assuming a production cross section of 10 fb. The last bins of the distributions contain all events with $m_{jj}^{red} > 3000$ GeV. The difference between the data and the predicted background, divided by the data statistical uncertainty are shown in the lower panels.

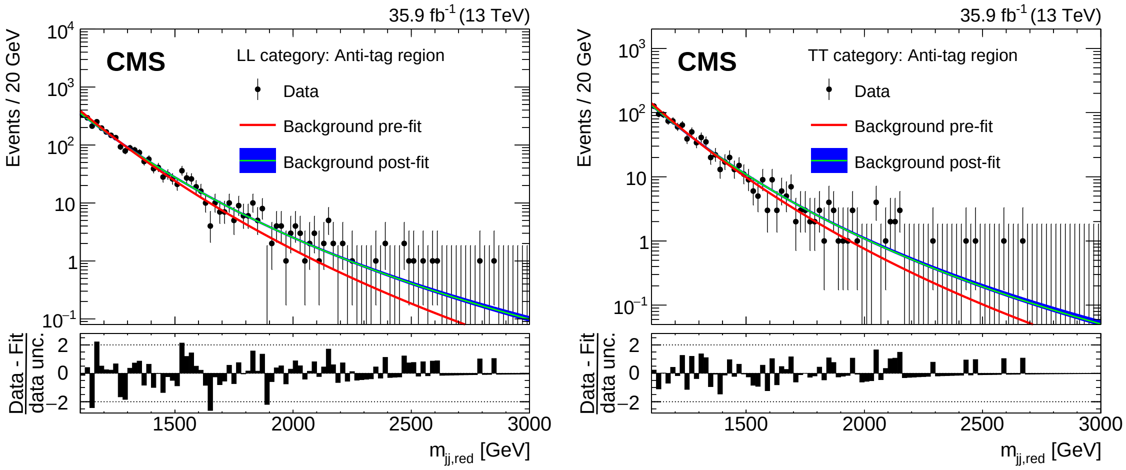

Figure 6.35: The m_{jj}^{red} distributions in the anti-tag region for the LL (left) and TT (right) categories. The black markers are the data while the curves show the pre-fit and post-fit background shapes. The difference between the data and the predicted background, divided by the data statistical uncertainty are shown in the lower panels.

of the parameter of interest, which is the signal strength. The LL and TT categories are combined by correlating the nuisance parameters that they share. The limits from the combination are shown in Figure 6.37 and Table 6.13 for a narrow width radion and a bulk graviton produced through

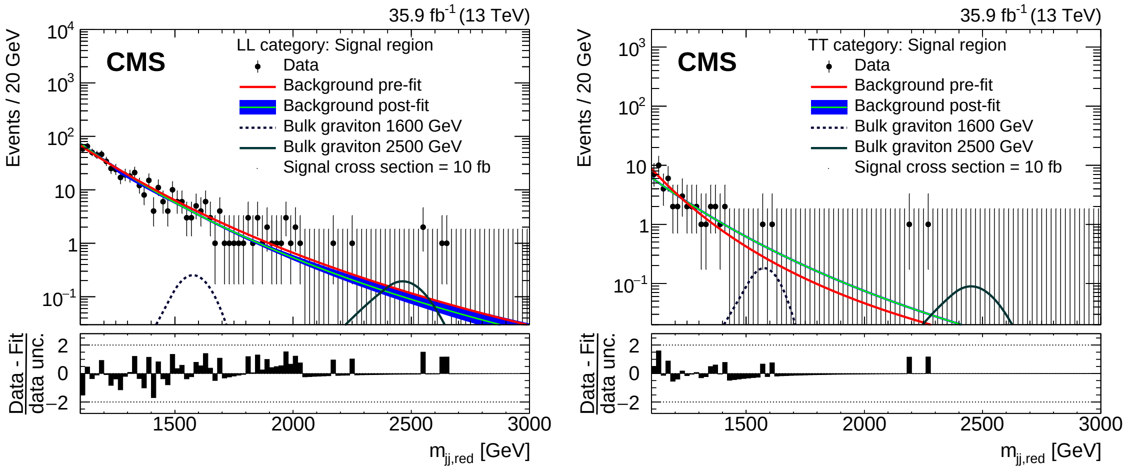

Figure 6.36: The m_{jj}^{red} distributions in the signal region for the LL (left) and TT (right) categories. The black markers are the data while the curves show the pre-fit and post-fit background shapes. The contributions of bulk gravitons of masses 1600 and 2500 GeV are shown assuming a production cross section of 10 fb. The difference between the data and the predicted background, divided by the data statistical uncertainty are shown in the lower panels.

gluon-gluon fusion and assumed to decay to a pair of Higgs bosons with a branching fraction of 23% and 10%, respectively. The expected limit on the bulk graviton is more stringent than those on the radion due to the $|\Delta\eta(j_1, j_2)| < 1.3$ requirement. The bulk gravitons, being spin-2 particles, produce more central jets, and hence have higher efficiency with respect to this selection criterion, than the radions. Thus, the signal sensitivity for a bulk graviton is higher than that for a radion of the same mass.

The upper limits on the production cross sections and branching fraction lies in the range $126 - 1.4$ fb for a narrow resonance X of mass $750 < m_X < 3000$ GeV. Assuming $\Lambda_R = 3$ TeV, a radion with a mass between 970 and 1400 GeV is excluded at 95% confidence level, except in a small region close to 1200 GeV, where the observed limit is 11.4 pb, the theoretical prediction being 11.2 pb.

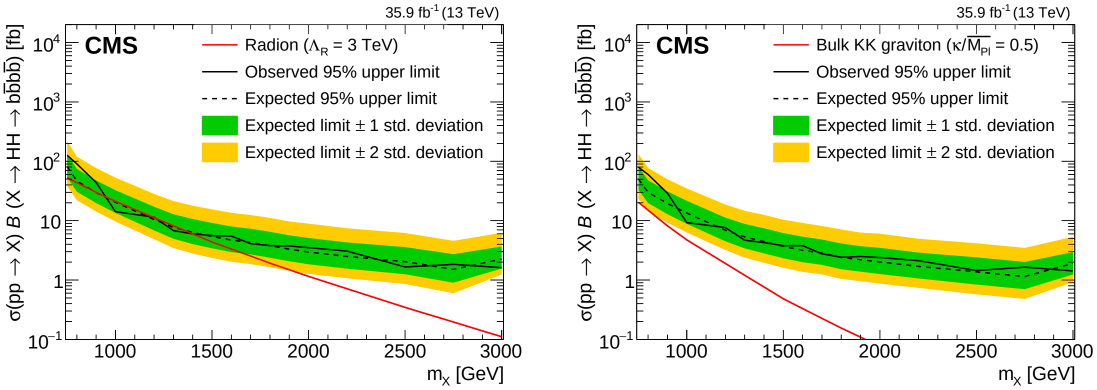

Figure 6.37: The limits for the spin-0 radion (left) and the spin-2 bulk graviton (right) models. The result for $m_X < 1100$ GeV uses the background predicted by the Alphabet method, while for $m_X \geq 1100$ GeV the background is derived from the AABH method. The predicted theoretical cross sections for a narrow radion or a bulk graviton are also shown.

Resonance Mass (GeV)	Radion		Bulk graviton	
	Expected	Observed	Expected	Observed
750	81.6	125.9	50.2	79.4
800	46.4	90.4	29.9	59.9
900	29.8	44.0	19.5	29.0
1000	20.4	14.2	13.4	9.3
1200	10.4	11.4	6.9	7.6
1400	6.3	6.0	4.4	4.3
1600	4.7	5.5	3.2	3.8
1800	3.8	3.8	2.4	2.4
2000	3.0	3.5	2.0	2.4
2500	2.0	1.7	1.4	1.4
3000	2.5	1.4	1.7	1.1

Table 6.13: Comparison of expected and observed limits on the production cross section of a resonance decaying to HH for the bulk graviton and the radion signal hypotheses, for different values of the resonance mass. The limits for masses below 1200 GeV are obtained using the Alphabet background estimation method, while those above use the AABH method.

Chapter 7

Summary and Outlook

This thesis presents a search for a narrow massive resonance decaying to a pair of Higgs bosons in the four b quark final state using the LHC proton-proton collision data collected at a center-of-mass energy of 13 TeV by the CMS detector, and corresponding to an integrated luminosity of 35.9 fb^{-1}. The $H \rightarrow bb$ decays are reconstructed as large-area jets and identified using jet substructure and b-tagging techniques. The main background is multijet production through QCD interactions and is estimated entirely from the data. The data are found to be consistent with the standard model expectations, and therefore upper limits are set on the products of the resonant production cross sections of a Kaluza-Klein bulk graviton and a Randall-Sundrum radion, and their branching fraction to $\mathrm{HH} \rightarrow \mathrm{b\bar{b}b\bar{b}}$. The limits range from 126 to 1.4 fb at 95% confidence level for bulk gravitons and radions in the mass range $750 - 3000$ GeV. For the mass scale $\Lambda_R = 3$ TeV, a radion of mass between 970 and 1400 GeV is excluded. The expected limits on the radion and bulk graviton for all resonant HH searches done at CMS with 2016 data can be seen in Figure 7.1. For resonance masses > 1100 GeV the limits from this analysis are the most stringent. Ongoing work is currently being done by the CMS Collaboration to improve the limits by combining all of these HH search channels, although the inclusion of the $\mathrm{b\bar{b}}\gamma\gamma$ channel will only neglibly improve the sensitivity at high resonance masses due to the strength of the $\mathrm{b\bar{b}b\bar{b}}$ channel.

By the end of 2018, the CMS detector will have collected $\sim$130 fb^{-1} of 13 TeV data and the sensitivity of the $\mathrm{HH} \rightarrow \mathrm{b\bar{b}b\bar{b}}$ search will be improved by utilizing this full dataset. A recent development within the CMS collaboration that could further improve the sensitivity of this search

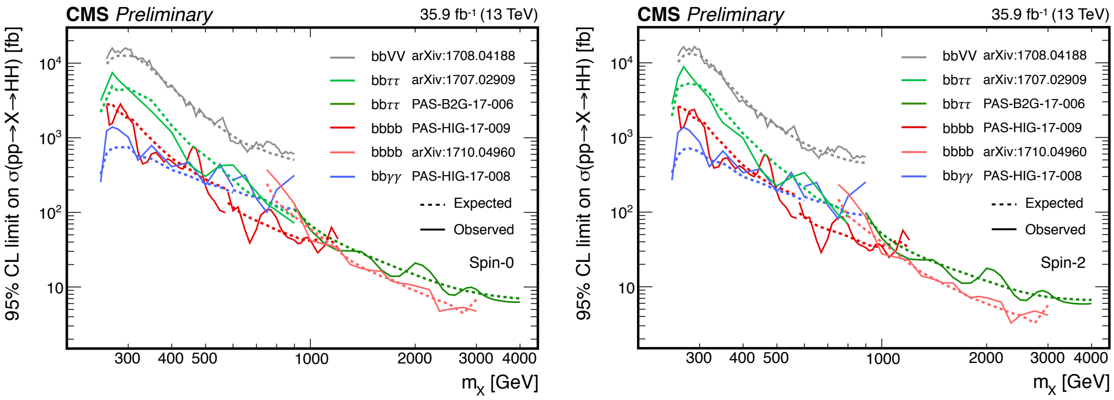

Figure 7.1: The limits for the spin-0 radion (left) and the spin-2 bulk graviton (right) from all resonant HH final states searched for with the CMS detector in the full 2016 dataset. The results present in this thesis are labeled as bbbb arXiv:1710.04960 [12].

is the development of a new double-b tagger. This double-b tagger is created from a deep neural network to improve on the signal discrimination from the double-b tagger used in this analysis. Initial studies have found that at the same QCD mistag rate the new double-b tagger doubles the tagging efficiency of $H \rightarrow b\bar{b}$ events. The increase in sensitivity of this analysis would be greatly improved by increasing the discrimination between QCD background and HH signal events.

Looking further into the future, the plan for the LHC is to shut down for over two years after the 2018 data taking period in preparation for a slight increase to the center-of-mass energy to 14 TeV and the CMS detector is expected to collect $\sim$300 fb^{-1} of data at this energy. Then another shut down will occur in preparation for the HL-LHC which will begin running in 2026 and is expected to collect $\sim$3000 fb^{-1}. In order for the CMS detector to be able to handle the large amount of pileup at the HL-LHC, where it will increase to at least 140 compared to the $45-60$ that was obtained during 2016, the pixel detector will have to be completely replaced. The radiation studies presented in this thesis indicate that 65 nm CMOS technology is a viable technology for the HL-LHC pixel detector and would allow the pixel detector to function throughout the lifetime of the HL-LHC.

With this increase in center-of-mass energy and the large amount of expected data, hopefully searches for resonant HH production will be able produce a discovery at the LHC. In the scenario that no discovery is made, resonant and non-resonant HH searches will be able to place precise constraints on SM HH production and possibly determine the Higgs self-coupling, λ_{HHH}. Projections have been done that predict the CMS detector will be able to measure λ_{HHH} with a significance of 0.9σ with 3000 fb^{-1} of data by combining the $bb\tau\tau$ and $bb\gamma\gamma$ search channels [97]. However, including other search channels, such as $\mathrm{b\bar{b}b\bar{b}}$ where the backgrounds have been much more manageable than expected due to double-b tagging, in the combination will increase the significance and furthermore, unforeseen improvements to analysis techniques could further push this significance to a discovery. Therefore, I am optimistic that a discovery of SM HH production is feasible within the current expected lifetime of the LHC.

Bibliography

[1] LHC Higgs Cross Section Working Group. Handbook of LHC Higgs Cross Sections: 4. Deciphering the Nature of the Higgs Sector, volume CERN-2017-002-M. 2017.

[2] Science Node. A standard infographic of the SM. `https://sciencenode.org/img/Standard_model_infographic.png/`, April 2014.

[3] CMS Collaboration. Observation of a new boson at a mass of 125 GeV with the CMS experiment at the LHC. Phys. Lett. B, 716(30), 2012.

[4] ATLAS and CMS Collaborations. Measurements of the Higgs boson production and decay rates and constraints on its couplings from a combined ATLAS and CMS analysis of the LHC pp collision data a $sqrts = 7$ and 8 TeV. JHEP, 08(045), 2016.

[5] J. Baglio et. al. The measurement of the Higgs self-coupling at the LHC: theoretical status. JHEP, 04(151), 2013.

[6] CMS Collaboration. Identification of b-quark jets with the CMS experiment in the LHC Run 2. (CMS-PAS-BTV-15-001), 2016.

[7] CMS Collaboration. Identification of double-b quark jets in boosted event topologies. CMS Physics Analysis Summary CMS-PAS-BTV-15-002, CERN, 2016.

[8] Phys Org. Breaking the performance barrier of 22-nm CMOS technology. `https://phys.org/news/2008-02-barrier-nm-cmos-technology.html`, 2008.

[9] Federico Faccio and Giovanni Cervelli. Radiation-Induced Edge Effects in Deep Submicron CMOS Transistors. IEEE Transactions on Nuclear Science, 52(6):2413–2420, 2005.

[10] CMS Collaboration. Identification techniques for highly boosted W bosons that decay into hadrons. JHEP, 1412(017), 2014.

[11] CMS Collaboration. Pileup Removal Algorithms. CMS Physics Analysis Summary CMS-PAS-JME-14-001, CERN, 2014.

[12] Roberto Salerno. Summary of run-II $\sigma(gg \to X) \times B(X \to HH)$95% CL upper limits assuming spin-0 and spin-2 hypothesis. Technical report, 2018.

[13] F. Englert and R. Brout. Broken Symmetry and the Mass of Gauge Vector Mesons. Phys. Rev. Lett., 13:321–323, 1964.

[14] P. W. Higgs. Broken Symmetries and the Mass of Gauge Besons. Phys. Rev. Lett., 13:508–509, 1964.

[15] J. Goldstone. Field theories with ¡¡ Superconductor ¿¿ solutions. Il Nuovo Cimento, 19(154), 1961.

[16] ATLAS Collaboration. Observation of a new particle in the search for the Standard Model Higgs boson with the ATLAS detector at the LHC. Phys. Lett. B, 716(1), 2012.

[17] ATLAS and CMS Collaboration. Combined Measurement of the Higgs Boson Mass in pp Collisions at $\sqrt{s} = 7$ and 8 TeV with the ATLAS and CMS Experiments. Phys. Rev. Lett., 114(191803), 2015.

[18] ATLAS Collaboration. Measurements of the Higgs boson production and decay rates and coupling strengths using pp data at $\sqrt{s} = 7$ and 8 TeV in the ATLAS Experiment. Eur. Phys. J., C 76(6), 2016.

[19] CMS Collaboration. Precise determination of the mass of the Higgs boson and tests of compatibility of its couplings with the standard model predicitons using proton collisions at 7 and 8 TeV. Eur. Phys. J., C 75(212), 2015.

[20] L. Randall and R. Sundrum. A large mass hierarchy from a small extra dimension. Phys. Rev. Lett., 83(3370), 1999.

[21] W. D. Goldberger and M. B. Wise. Modulus stabilization with bulk fields. Phys. Rev. Lett., 83(4922), 1999.

[22] C. Csaki, M. Graesser, L. Randall, and J. Terning. Cosmology of brane models with radion stabilization. Phys. Rev. D, 62(045015), 2000.

[23] C. Csaki, M. Graesser, and G. D Kribs. Radion dynamics and electroweak physics. Phys. Rev. D, 63(065002), 2001.

[24] H. Davoudiasl, J. L. Hewett, and T. G. Rizzo. Phenomenology of the Randall-Sundrum Gauge Hierarchy Model. Phys. Rev. Lett., 84(2080), 2000.

[25] O. DeWolfe, D. Z. Freedman, S. S. Gubser, and A. Karch. Modeling the fifth dimension with scalars and gravity. Phys. Rev. D, 62(046008), 2000.

[26] K. Agashe, H. Davoudiasl, G. Perez, and A. Soni. Warped gravitoins at the LHC and beyond. Phys. Rev. D, 76(036006), 2007.

[27] G. F. Giudice, R. Rattazzi, and J. D. Wells. Graviscalars from higher dimensional metrics and curvature Higgs mixing. Nucl. Rev. B, 595(250), 2001.

[28] D. Dominici, B. Grzadkowski, J. F. Gunion, and M. Toharia. The scalar sector of the Randall-Sundrum model. Nucl. Rev. B, 671(243), 2003.

[29] A. Oliveira and R. Rosenfeld. Hidden sector effects on double higgs production near threshold at the LHC. Phys. Lett. B, 702(201), 2011.

[30] V. Barger and M. Ishida. Randall-Sundrum Reality at the LHC. Phys. Lett. B, 709(185), 2012.

[31] R. Schabinger and J. D. Wells. A Minimal Spontaneously Broken Hidden Sector and its Impact on Higgs Boson Physics at the Large Hadron Collider. Phys. Rev. D, 72(093007), 2005.

[32] T. Robens and T. Stefaniak. Status of the Higgs Singlet Extension of the Standard Model after LHC Run 1. Eur. Phys. J. C, 75(105), 2015.

[33] H. Georgi and M. Machacek. Doubly charged Higgs bosons. Nucl. Phys. B, 262(463), 1985.

[34] J. Chang C. Chen and C. Chiang. Higgs boson pair productions in the Georgi-Machacek model at the LHC. JHEP, 03(137), 2017.

[35] Lyndon Evans and Philip Bryant. LHC Machine. JINST, 3(S08001), 2008.

[36] Julie Haffner. The CERN accelerator complex, 2013.

[37] CMS Collaboration. The CMS experiment at the CERN LHC. JINST, 3(S08004), 2008.

[38] Viktor Veszpremi. CMS Pixel Detector 2015 Offline Performance Results - For LHC Commitee Meeting. Technical report, 2015.

[39] CMS Collaboration. CMS Technical Design Report for the Pixel Detector Upgrade. (CERN-LHCC-2012-016), 2012.

[40] CMS Collaboration. The electromagnetic Calorimeter Technical Design Report. (CERN-LHCC-97-033, CMS-TDR-4), 1997.

[41] A. M. Sirunyan et al. Particle-flow reconstruction and global event description with the cms detector. JINST, 12:P10003, 2017.

[42] CMS Collaboration. Particle-Flow Event Reconstruction in CMS and Performance for Jets, Taus, and E_T^{miss}. CMS-PAS-PFT-09-001, 2009.

[43] CMS Collaboration. Description and performance of track and primary-vertex reconstruction with the CMS tracker. JINST, 9, 2014.

[44] Rudolf Fruhwirth. Application of Kalman filtering to track and vertex fitting. Nucl. Instrum. Meth., A262:444–450, 1987.

[45] W. Adam, R. Fruhwirth, A. Strandlie, and T. Todorov. Reconstruction of electrons with the Gaussian-sum filter in the CMS tracker at the LHC. Journal of Physics G: Nuclear and Particle Physics, 31(9), 2005.

[46] S. Bonancini, P. Valerio, R. Avramidou, R. Ballabriga, F. Faccio, K. Kloukinas, and A. Marchioro. Characterization of a commercial 65 nm CMOS technology for SLHC applications. JINST, 7(P01015), 2012.

[47] Timothy R. Oldham. Basic Mechanisms of TID and DDD Response in MOS and Bipolar Microelectronics. GSFC Radiation Effects and Analysis Group, 2011.

[48] F. Faccio, S. Michelis, D. Cornale, A. Paccagnella, and S. Gerardin. Radiation-Induced Short Channel (RISCE) and Narrow Channel (RINCE) Effects in 65 and 130 nm MOSFETs. IEEE Transactions on Nuclear Science, 62(6):2933–2940, 2015.

[49] Dieter K. Schroeder. Semiconductor Material and Device Characterization. Wiley-IEEE Press, New York, 1998.

[50] CMS Collaboration. Search for a massive resonance decaying to a pair of Higgs bosons in the four b quark final state in proton-proton collisions at $\sqrt{s} = 13$ TeV. Phys. Lett. B, 781(10), 2018.

[51] ATLAS Collaboration. Search for Higgs boson pair production in the $\gamma\gamma b\bar{b}$ final state using pp collision data at $\sqrt{s} = 8$ TeV from the ATLAS detector. Phys. Rev. Lett., 114(081802), 2015.

[52] ATLAS Collaboration. Search for Higgs boson pair production in the $b\bar{b}b\bar{b}$ final state using pp collisions at $\sqrt{s} = 8$ TeV with the ATLAS detector. Eur. Phys. J. C, 75(412), 2015.

[53] ATLAS Collaboration. Search for Higgs boson pair production in the $hh \to b\bar{b}\tau\tau$, $\gamma\gamma WW^*$, $\gamma\gamma bb$, $bbbb$ channels with the ATLAS detector. Phys. Rev. D, 92(092004), 2015.

[54] CMS Collaboration. Search for resonant pair production of Higgs bosons decaying to two bottom quark-antiquark pairs in proton-proton collisions at 8 TeV. Phys. Lett. B, 749(560), 2015.

[55] CMS Collaboration. Search for a heavy scalar boson H decaying to a pair of Higgs bosons hh or for a heavy pseudoscalar boson A decaying to Zh, in the final states with $h \to \tau\tau$. Phys. Lett. B, 755(217), 2016.

[56] CMS Collaboration. Search for two Higgs bosons in final states containing two photons and two bottom quarks in proton-proton collisions at 8 TeV. Phys. Rev. D, 94(052012), 2016.

[57] CMS Collaboration. Search for heavy resonances decaying to two Higgs bosons in final states containing four b quarks. Eur. Phys. J. C, 76(371), 2016.

[58] M. Dasgupta, A. Fregoso, S. Marzani, and G. P. Salam. Towards an understanding of jet substructure. JHEP, 09(029), 2013.

[59] A. J. Larkoski, S. Marzani, G. Soyez, and J. Thaler. Soft drop. JHEP, 05(146), 2014.

[60] J. Thaler and K. Van Tilburg. Identifying Boosted Objects with N-subjettiness. JHEP, 03(093), 2011.

[61] J. Thaler and K. Van Tilburg. Maximizing Boosted Top Identification by Minimizing N-subjettiness. JHEP, 03(093), 2012.

[62] J. Alwall et al. The automated computation of tree-level and next-to-leading order differential cross sections, and their matching to parton shower simulations. JHEP, 07(079), 2014.

[63] NNPDF Collaboration. Parton distributions for the LHC Run II. JHEP, 04(040), 2015.

[64] L. A. Harland-Lang, A. D. Martin, P. Motylinski, and R. S. Thorne. Parton distributions in the LHC era: MMHT 2014 PDFs. Eur. Phys. J. C, 75(204), 2015.

[65] A. Buckley et al. LHAPDF6: parton density access in the LHC precision era. Eur. Phys. J. C, 75(132), 2015.

[66] S. Carrazza, J. I. Latorre, J. Rojo, and G. Watt. A compression algorithm for the combination of PDF sets. Eur. Phys. J. C, 75(474), 2015.

[67] J. Butterworth et al. PDF4LHC recommendations for LHC Run II. J. Phys. G, 43(023001), 2016.

[68] T. Sjöstrand et al. An Introduction to PYTHIA 8.2. Comput. Phys. Commun, 191(159), 2015.

[69] CMS Collaboration. Event generator tunes obtained from underlying event and multiparton scattering measurements. Eur. Phys. J. C, 76(115), 2016.

[70] S. Gieseke, C. Rohr, and A. Siodmok. Colour reconnections in Herwig++. Eur. Phys. J. C, 72(225), 2012.

[71] S. Frixione, G. Ridolfi, and P. Nason. A postive-weight next-to-leading-order monte carlo for heavy flavour hadroproduction. JHEP, 09(126), 2007.

[72] S. Frixione, P. Nason, and C. Oleari. Matching NLO QCD computations with Parton Shower simulations: the POWHEG method. JHEP, 11(070), 2007.

[73] S. Alioli, P. Nason, C. Oleari, and E. Re. A general framework for implementing NLO calculations in shower Monte Carlo programs: the POWHEG BOX. JHEP, 06(043), 2010.

[74] GEANT4 Collaboration. GEANT4–a simulation toolkit. Nucl. Instrum. Meth. A, 506(250), 2003.

[75] J. Allison et al. Geant4 developments and applications. IEEE Trans. Nucl. Sci., 53(270), 2006.

[76] M. Cacciari, G. P. Salam, and G. Soyez. The anti-k_t jet clustering algorithm. JHEP, 04(063), 2008.

[77] M. Cacciari, G. P. Salam, and G. Soyez. FastJet user manual. Eur. Phys. J. C, 72(1896), 2012.

[78] D. Bertolini, P. Harris, M. Low, and N. Tran. Pileup per particle identification. JHEP, 10(059), 2014.

[79] CMS Collaboration. Jet enery scale and resolution in the CMS experiment in pp collisions at 8 TeV. JINST, 12(P02014), 2017.

[80] CMS Collaboration. Jet enery scale and resolution performance with 13 TeV data. CMS Detector Performance Summary CMS-DP-2016-020, CERN, 2016.

[81] G. P. Salam. Towards jetography. Eur. Phys. J. C, 67(637), 2010.

[82] M. Dasgupta, A. Fregoso, S. Marzani, and G. P. Salam. Towards an understanding of jet substructure. JHEP, 09(029), 2013.

[83] CMS Collaboration. Jet algorithms performance in 13 TeV data. CMS Physics Analysis Summary CMS-PAS-JME-16-003, CERN, 2017.

[84] S. Catani, Y. L. Dokshitzer, M. H. Seymour, and B. R. Webber. Longitudinally invariant K_t clustering algorithms for hadron hadron collisions. Nucl. Phys. B, 406(187), 1993.

[85] S. D. Ellis and D. E. Soper. Successive combination jet algorithm for hadron collisions. Phys. Rev. D, 48(3160), 1993.

[86] CMS Collaboration. Search for heavy resonances decaying to a pair of Higgs bosons in four b quark final state in proton-proton collisions at *sqrts* = 13 TeV. CMS Physics Analysis Summary CMS-PAS-B2G-16-008, CERN, 2016.

[87] R. G. Lomax and D. L. Hahs-Vaighn. Statistical concepts: a second course. Taylor and Francis, Hoboken, NJ, 2012.

[88] CMS Collaboration. CMS Luminosity Measurement for the 2016 Data Taking Period. CMS Physics Analysis Summary CMS-PAS-LUM-17-001, CERN, 2017.

[89] J. Butterworth et al. PDF4LHC recommendations for LHC Run II. J. Phys. G, 43(023001), 2016.

[90] S. Dulat et al. Parton distribution functions from a global analysis of quantum chromodynamics. Phys. Rev. D, 93(033006), 2016.

[91] L. A. Harland-Lang, A. D. Martin, P. Motylinski, and R. S. Thorne. Parton distributions in the LHC era: MMHT 2014 PDFs. Eur. Phys. J, C75(204), 2015.

[92] NNPDF Collaboration. Parton distributions in the LHC Run II. JHEP, 04(040), 2015.

[93] R. Barlow and C. Beeston. Fitting using finite Monte Carlo samples. Comput. Phys. Commun., 77(219), 1993.

[94] A. L. Read. Presentation of search results: The CL_s technique. J. Phys. G, 28(2693), 2002.

[95] T. Junk. Confidence level computation for combining searches with small statistics. Nucl. Instrum. Meth. A, 434(435), 1999.

[96] G. Cowan, K. Cranmer, E. Gross, and O. Vitells. Asymptotic formulae for likelihood-based tests of new physics. Eur. Phys. J. C, 71(1554), 2011.

[97] CMS Collaboration. Technical Proposal for the Phase-II Upgrade of the CMS Detector. Technical Report CERN-LHCC-2015-010, CERN, 2015.

[98] Florian Beaudette. The CMS Particle Flow Algorithm. Proceedings of the International Conference on Calorimetery for the High Energy Frontier, pages 295–304, 2013.

[99] M. Krohn, B. Bentele, D.C Christian, J.P. Cumalat, G. Deptuch, F. Fahim, J. Hoff, A. Shenai, and S.R. Wagner. Radiation tolerance of 65 nm CMOS transistors. JINST, 10(P12007), 2015.